

**The ‘lower dimer’ and its role in actin patterning:
Studying different forms of actin by electron microscopy,
biochemistry and tailor-made antibodies**

Inauguraldissertation

zur

Erlangung der Würde eines Doktors der Philosophie
vorgelegt der
Philosophisch-Naturwissenschaftlichen Fakultät
der Universität Basel

von

Ulrich Johannes Hubertus Schröder
aus Würzburg, Deutschland

Basel, 2011

Genehmigt von der Philosophisch-Naturwissenschaftlichen Fakultät

auf Antrag von

Prof. Dr. Ueli Aebi, PD Dr. Cora-Ann Schoenenberger und Prof. Dr. Hans Georg Mannherz

Basel, den 9.12.2008

Prof. Dr. Eberhard Parlow
Dekan

for my beloved sons

Jacob and Julian

Table of Contents

Summary	1
----------------------	---

Chapter 1

The actin ‘lower dimer’ modulates the structure of actin filaments	5
1.1 Introduction.....	6
1.2 Aims of project.....	15
1.3 Material and methods.....	15
1.4 Results.....	20
1.5 Discussion.....	34
1.6 Conclusions and outlook.....	41

Chapter 2

Peptide Nanoparticles - a potent immunogen for the production of monospecific antibodies	42
2.1 Introduction.....	43
2.2 Aims of project.....	45
2.3 Material and methods.....	46
2.4 Results 1.....	47
2.5 Results 2.....	54
2.6 Results 3.....	79
2.7 Conclusions and outlook.....	82

Chapter 3

Raver1 - an integral component of muscle contractile elements and a potential ligand for actin.....	83
3.1 Introduction.....	84
3.2 Material and methods.....	86
3.3 Results 1.....	88
3.4 Results 2.....	104
3.5 Conclusions and outlook.....	113
References.....	115
Acknowledgments.....	134
Curriculum vitae.....	135

Summary

The ‘lower dimer’ and its role in actin patterning:

**Studying different forms of actin by
electron microscopy, biochemistry
and tailor-made antibodies**

At the onset of actin polymerization, a transient species termed ‘lower dimer’ (LD) is incorporated into growing filaments, but disintegrates during filament maturation. Because two actin subunits assume an antiparallel orientation in the LD, it is inherently polymerization-incompetent and its subunit contacts do not occur in F-actin filaments at steady state. However, by copolymerizing G-actin and previously cross-linked LD in the presence of phalloidin, we were able to produce a novel type of actin hybrid filaments, which contained the LD at steady state. The presence of LD in hybrid filaments was verified by high-speed sedimentation and subsequent SDS-PAGE analyses as well as by conventional and scanning transmission electron microscopy (CTEM and STEM). Copolymerization of mixtures containing G-actin and increasing amounts of LD depicted that the LD was incorporated into hybrid filaments at corresponding ratios. One subunit of the LD contributed to the hybrid filament backbone whereas the other jutted out from the filament surface, thereby causing numerous lateral protrusions. Occasionally, these protrusions initiated the branching of lateral emanating daughter filaments. Hybrid filaments revealed also a high degree of structural variation. Frequent local unraveling of the two hybrid filament strands and perturbation of crossover spacings indicated that the presence of incorporated LD also strongly interfered with interstrand subunit contacts. It seems that particularly in highly disordered filament sections, the intersubunit contacts needed for phalloidin binding were not established. As a consequence subunits were released and/or exchanged at steady state.

Contrary to the biochemical evidence and CTEM analysis which clearly demonstrate the co-polymerization of LD and actin into hybrid filaments, STEM data did not reveal any difference between mass-per-length (MPL) and full-width half-maximum (FWHM) in hybrid versus conventional F-actin filaments.

Our findings corroborate that actin has the intrinsic ability for branching in vitro, and that the LD substantially contributes in the formation of branching sites.

In the second part of this study we tested the immunogenic potential of a novel type of self-assembled peptide nanoparticles. According to the design principles, 60 copies of a computationally designed and recombinantly expressed coiled coil polypeptide self-assemble to form highly organized regular dodecahedrons of defined size.

In order to elucidate whether the nanoparticles (NP) can be functionalized to potent immunogens, we genetically engineered a 13mer corresponding to the amino acid residues 239 - 251 of human β -cytoplasmic actin onto the C-terminus of the NP.

The resulting nanoparticles were termed NP-Gly. Corresponding nanoparticles containing the same actin sequence but with a single point mutation from Gly to Asp at the original position 245 were termed NP-Asp. A 13mer peptide containing this mutation has previously

been used to produce a monospecific polyclonal antiserum in rabbits. CTEM analysis revealed that neither epitope interfered with the formation of homogenous populations of nanoparticles. Moreover, immunochemical analyses with the antisera against wild type and G245D mutant actin demonstrated the accessibility of the corresponding epitopes on NP-Gly and NP-Asp. Subsequent immunization of rabbits with NP-Gly and NP-Asp yielded individual polyclonal antisera that were shown to react with wild type and mutant actin, respectively.

In order to examine the immunogenic potential of a distinct structural element that is exposed on the nanoparticles surface, we grafted 12mers corresponding to the so-called ‘hydrophobic loop’ of human β -cytoplasmic actin onto the C-terminus of NPs. Since the ‘hydrophobic loop’ is buried within the F-actin filaments, but is exposed to the surface of monomeric actin, we assumed that immunization with nanoparticles containing the ‘hydrophobic loop’ epitope would yield antibodies that detected only non-filamentous actin.

In a first construct, an additional Cys residue was introduced downstream of the nanoparticle core polypeptide in order to stabilize the propensity of the grafted actin epitope to assume a loop structure by a disulphide bond with the Cys residue contained in the epitope sequence. The resulting nanoparticles were termed NP-L/C and extensively aggregated as displayed by electron micrographs. In a second construct termed NP-L/S, both cysteines were replaced by Ser residues in order to eliminate the random formation of disulphide bonds between polypeptides. CTEM analyses confirmed that NP-L/S assembled into a disperse population of spherical particles rather than forming aggregates.

Following immunization of mice with NP-L/C, six individual hybridoma clones were selected, all of which produced IgGs of the subclass 2b. Immunoblot experiments under native and denaturing conditions revealed that the monoclonal antibodies (mAbs) specifically reacted with NP-L/C and NP-L/S. In addition, the mAbs reacted with purified skeletal muscle actin and detected actin in a number of total cell extracts. Fluorescence cross-correlation spectroscopy further demonstrated the binding specificity of selected antibodies with NP-L/S.

The *in situ* reactivity of the mAbs was further characterized by immunofluorescence on Rat2 fibroblasts and immunogold labeling on ultrathin sections of different cell lines and tissues. These experiments showed that the mAbs which were raised against loop nanoparticles, also recognized the ‘hydrophobic loop’ of actin in its native context throughout the cytoplasm and in the nucleus. The presence of the antigenic determinant in the nucleus and the absence of a filamentous staining pattern in the cytoplasm indicated that the epitope was readily detected in non-filamentous actin, but hidden in F-actin filaments. Consistently, the mAbs did not cosediment with F-actin filaments from purified skeletal muscle actin in high-speed cosedimentation assays.

In conclusion, the data show that self-assembling peptide nanoparticles are a suitable platform for the immunogenic surface display of actin-related epitopes, which because of their high conservation are poor antigens. Presenting the refractory antigenic determinants in an ordered, repetitive array significantly increased the immune response of the host animal, resulting in specific poly- and monoclonal antibodies.

The third part of this study addresses the interaction of actin with Raver1. This ubiquitously expressed hnRNP protein resides primarily in the nucleus, where it colocalizes with the polypyrimidine-tract binding protein PTB. During skeletal muscle differentiation, raver1 translocates to the I-Z-I-band of sarcomers, where it colocalizes with its ligands metavinculin, vinculin and α -actinin. In order to obtain a more detailed view on the potential role of raver1 in muscle, we investigated its distribution and localization in murine striated and smooth muscle using three monoclonal antibodies that recognize distinct epitopes at the N- and C-terminus of raver1. Immunofluorescence and immunoelectron microscopy showed that cytoplasmic raver1 is an integral part of the sarcomers of skeletal muscle, heart and smooth muscle, and is not restricted to costamers like its ligands vinculin and metavinculin. A closer look at isolated myofibrils and ultrathin sections of skeletal muscle revealed that raver1 mainly concentrated at sarcomeric I-Z-I band. Moreover, a minor fraction of raver1 was present in the nucleus of the three muscle types tested.

Pre-embedding immunolabeling of isolated *Xenopus* nuclei with all three antibodies revealed that raver1 at the nucleoplasmic periphery is preferentially located at the distal ring of the nuclear pore complex, where actin has also been described.

Cosedimentation assays and electron microscopy with recombinant full-length raver1 protein and a C-terminal deletion fragment revealed that both proteins induce bundling of F-actin filaments in vitro. In addition, preliminary data suggest that raver1 might also interact with monomeric actin.

Our data indicate that during muscle differentiation raver1 might link gene expression with structural functions of the contractile machinery of muscle. Moreover, due to the common localization of raver1 and actin in the cytoplasm and in the nucleus, one can assume that both proteins might translocate as complexes to the cytoplasm, possibly accompanied by proteinous cargo.

Chapter 1

The

actin ‘lower dimer’

modulates the structure of actin filaments

1.1 Introduction

1.1.1 Actin *in vivo*

Actin, a protein of 375 amino acids, is one of the most abundant proteins in nature. It is encoded by an evolutionary highly conserved gene family (Gallwitz and Sures 1980) and ubiquitously expressed in nearly all eukaryotic cells. Actin is known to be involved in a fast growing number of essential protein-protein interactions and actin represents also a key player of the highly dynamic eukaryotic cytoskeleton.

The intrinsic ability of actin monomers (G-actin) to reversibly assemble into filamentous polymers is the driving force for a multitude of motile cellular functions which are spatially and temporarily precisely orchestrated by a myriad of regulatory actin binding and actin related proteins (reviewed by (Pollard and Borisy 2003)). Despite the vast number of accessory proteins, the basis of actin-based motility remains the interaction of actin with itself.

Depending on its actual task, cytoplasmic actin occurs in different forms, such as G-actin, individual filaments, filament bundles and supramolecular filament assemblies. This polymorphism provides the basis for the diversity of actin functions including muscle contraction, maintenance of the cell shape, cell migration, cytokinesis, phagocytosis, intracellular transport, subcellular organization and definition of embryonal polarity (reviewed by (Pollard 2003; Rafelski and Theriot 2004; Disanza et al. 2005; Dormann and Weijer 2006; Kaksonen et al. 2006)).

Other than the established cytoplasmic conformations, actin can assume unconventional forms, which are sometimes transient. For instance, the transiently formed 'lower dimer' described below (see Chapter 1.1.3), is assumed to trigger the formation of distinct actin assemblies (Schoenenberger et al. 1999; Pope et al. 2000; Pelham and Chang 2001; Schoenenberger et al. 2002; Ono 2003; Pollard and Borisy 2003; Schmid et al. 2004; Disanza et al. 2005).

Over the past decades, various studies have reported the presence of actin in the nucleus in addition to the cytoplasm. However, the existence of nuclear actin was a matter of dispute for many years because it was regarded as artifact. Although the discovery of nuclear functions associated with actin has settled the dispute, the form of nuclear actin remains an enigma. Only few authors report on distinct forms of nuclear actin (Gard 1999; Kiseleva et al. 2004; McDonald et al. 2006). But there is increasing evidence that distinct pools of unconventional forms of actin, which have so far been undervalued, might contribute to the functions carried out by nuclear actin (Pederson and Aebi 2005; Schoenenberger et al. 2005; Jockusch et al. 2006).

Only little is known of the role of actin in the nucleus. But there is increasing experimental evidence that nuclear actin might be involved in essential nuclear processes such as chromatin remodeling, initiation of RNA polymerase activity during transcription, RNA processing,

nucleo-cytoplasmic transport and assembly and maintenance of the nuclear envelope (reviewed by (Jockusch et al. 2006; Percipalle and Visa 2006; Chen and Shen 2007)).

1.1.2 Structural characteristics of actin

To achieve both a mechanistic understanding of the actin function and its interactions with other proteins, it is crucial to know the atomic structure of G-actin as well as the subunit contacts in F-actin filaments. Initially, crystallization of unbound or unmodified G-actin failed, because conditions favoring 3-D crystallization induce the formation of F-actin filaments. These, in turn, are essentially incompatible with the growth of 3-D crystals. To overcome these difficulties, 2-D crystals of skeletal muscle actin were grown in the presence of the trivalent lanthanide gadolinium (Dos Remedios and Dickens 1978). However, the 3-D structure from tilted views of negatively stained 2-D crystals were only resolved at low resolution (Aebi et al. 1980; Aebi et al. 1981; Smith et al. 1983; Steinmetz et al. 1998).

The first crystal structures of monomeric actin at atomic resolution were determined from a number of complexes with actin binding proteins that prevent polymerization, such as DNase I (Kabsch et al. 1990), profilin (Schutt et al. 1993; Chik et al. 1996), gelsolin fragments (Mannherz et al. 1992; McLaughlin et al. 1993; Irobi et al. 2003; Vorobiev et al. 2003) and vitamin D-binding protein (Otterbein et al. 2002). Based on crystal structures of a nonpolymerizable tetramethylrhodamine-labeled monomeric actin (TMR-actin) with ADP (Otterbein et al. 2001) or with the non-hydrolyzable ATP analog AMPPNP (Graceffa and Dominguez 2003) at the active site, structural differences between ADP and ATP actin have been revealed (see also (Rould et al. 2006)). More recently, the atomic structure of pure polymerization-competent G-actin was solved (Klenchin et al. 2006).

Today, the structure of the monomeric actin is understood in considerable detail. Most of the atomic structures of monomeric actin display striking similarities except for some very flexible regions, such as for instance the C-terminus and the DNase I binding loop in subdomain 2. In addition, depending on the crystallization conditions, the nucleotide-binding cleft has been found in an open or closed conformation (Otterbein et al. 2001; Sablin et al. 2002; Klenchin et al. 2006; Rould et al. 2006).

The asymmetric actin molecule consists of four subdomains that fit into a box measuring 5.5 x 5.5 x 3.5 nm. The polarity of actin, which is of great importance in actin dynamics, is determined by mass differences of the subdomains (Kabsch et al. 1990; Bremer and Aebi 1992). In the center of the molecule and embedded by all subdomains, there are both a single high affinity binding site for a nucleotide (ATP/ADP-P_i/ADP) and for a divalent cation (Mg²⁺/Ca²⁺). The cohesion of all subdomains is mainly supported by chemical interactions between the phosphate groups of the nucleotide and the divalent cation.

The first structural model of the F-actin filament was published by Holmes and colleagues (1990), who determined the approximate orientations and positions the atomic structure of

G-actin in the filament by using fiber-diffraction data from oriented gels of actin filaments (Holmes et al. 1990). A large number of studies using different analytical techniques confirmed the basic features of the 'Holmes' model and have led to its structural refinements (e.g. (Milligan et al. 1990; Bremer and Aebi 1992; Lorenz et al. 1993; Lorenz et al. 1995; Hoenger 1996; Kim et al. 2002; Holmes et al. 2003; Holaska et al. 2004)).

There is a general agreement that an F-actin filament consists of two intertwined right-handed long-pitch helical strands, which cross each other, dependent on the experimental conditions, approximately every 36 nm. A helical turn is assumed to contain 13 actin subunits with an axial subunit repeat of 5.5 nm, and the two helical strands are axially staggered by half the axial subunit spacing (described in more detail by (Steinmetz et al. 1997).

However, due to averaging, the highly ordered assembly of subunits in these models disregards the flexibility of subunit interactions and subunits-subunit interfaces that occur in F-actin filament (Egelman et al. 1982; Sablin et al. 2002). For instance, as seen for the conformational transitions of nucleotide binding cleft during ATP hydrolysis and P_i -release, structural changes of subunits in actin filaments are essential characteristics for the regulation of their polarity and dynamics (Sablin et al. 2002).

Structural plasticity of F-actin filaments was also described in the 'lateral slipping' model by Bremer and colleagues (1991), which revealed that both long-pitch helical filament strands are capable to independently move along each other (Bremer et al. 1991). This depicted that the subunit contacts along the two long-pitch helical strands are continuous and much stronger than those between them (reviewed by (Holmes and Kabsch 1991; Bremer and Aebi 1992)). The two filament strands were also found to be locally unraveled at random sites (Aebi et al. 1986; Bremer and Aebi 1992; Steinmetz et al. 1997), which in turn changed the screw angle of the filaments.

Although many different studies revealed an astonishingly similar structure of G-actin at atomic resolution and to a large extent, there is an agreement concerning the model for the F-actin filament, the orientation and position of the subunits in the filament is so far only resolved to 8 - 10 Å resolution at best (Holmes et al. 1990; Schmid et al. 2004). Thus, many questions concerning the arrangement of actin subunits in polymeric actin assemblies are still open.

1.1.3 Actin polymerization and the actin 'lower dimer' (LD)

G-actin has the intrinsic ability to polymerize into F-actin filaments in the presence of salts. For a long period of time, the basic principle of actin polymerization was described as reversible, single pathway reaction that includes the three major steps i) fast monomer activation, ii) rate-limiting formation of trimeric nuclei and, iii) fast and linear elongation of the filament until a steady state without net filament growth is reached (reviewed by (Schoenenberger et al. 2002).

When G-actin polymerization is monitored by time-resolved conventional transmission electron microscopy (CTEM), it was shown that actin growing filaments undergo remarkable morphological changes. Shortly after the onset of polymerization, actin filaments appear ragged and branched, whereas at steady state they emerge smooth and linear, without lateral protrusions (Steinmetz et al. 1997; Schoenenberger et al. 2002). The formation of lateral protrusions at early stages of polymerization, even if transient, does not fit with the simple three-step model of polymerization described above.

A new understanding of the actin polymerization pathways and the molecular architecture of the actin filament was established by chemical cross-linking experiments using the bifunctional sulfhydryl reagent N,N'-1,4-phenylenebismaleimide (1,4-PBM) (Knight and Offer 1978). The addition of 1,4-PBM immediately after the salt-induced onset of polymerization yields an initial dimeric actin species with an apparent molecular mass of 86 kDa (Millonig et al. 1988). The production of this so-called 'lower dimer' (LD) is transient and in its place an 'upper dimer' (UD) with an apparent molecular mass of about 120 kDa by SDS-PAGE, is subsequently formed. Isolated cross-linked LD is not able to form F-actin filaments or nucleate filament formation, whereas UD will assemble into filaments indistinguishable from those polymerized from unmodified G-actin (Elzinga and Phelan 1984; Millonig et al. 1988; Steinmetz et al. 1997).

Given the appropriate experimental conditions, the transient production of the LD at early stages of polymerization can be sustained, leading to the presence of cross-linked LD at steady state (Steinmetz et al. 1997). The resulting filaments exhibit a ragged phenotype similar to that seen shortly after the initiation of polymerization without cross-linker and display an increased incidence of lateral protrusions and branches at steady state (Figure 1).

Thus, a correlation seems to exist between the detection of LD by chemical cross-linking experiments and the ragged morphology observed during maturation of F-actin filaments.

Of particular interest is the antiparallel orientation of the subunits in the LD. Crystallography revealed comparable atomic structures of actin dimers with subunits in antiparallel orientation (Bubb et al. 2002; Reutzler et al. 2004; Klenchin et al. 2006; Lassing et al. 2007).

Figure 2 exemplarily exhibits the structure of a polylysine-actin-latrunculin A dimer at 3.5 Å resolution, which is likely to be consistent with the antiparallel LD described above (Bubb et al. 2002).

At the interface of the actin monomers within the ribbon-and-strand representation there is a disulfide bond between the C-terminal Cys-374 residues of the individual subunits (Figure 2). It is conceivable that these Cys-374 are covalently cross-linked (Elzinga and Phelan 1984) by the 1,4-PBM linker which measures 11.1 ± 0.5 Å in length (Green et al. 2001). In addition, each subunit contributes two parallel helices to the specific interface that stabilize the corresponding helices of the adjacent monomer by intersubunit salt bridges between residues Glu-361 and Arg-372 in the model.

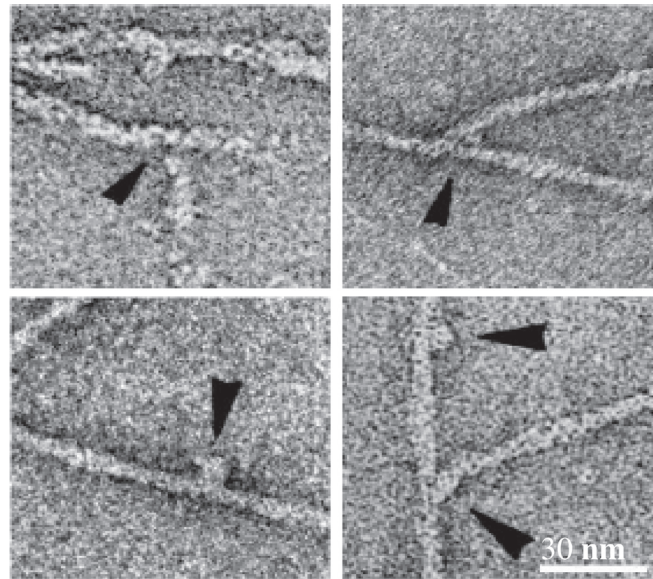


Figure 1. LD-containing ragged actin filaments. Arrowheads indicate lateral protrusions and branching sites that are most likely mediated by incorporated LD in actin filaments at steady state. Scale bar, 30 nm. Adapted from Schoenenberger et al. (2002).

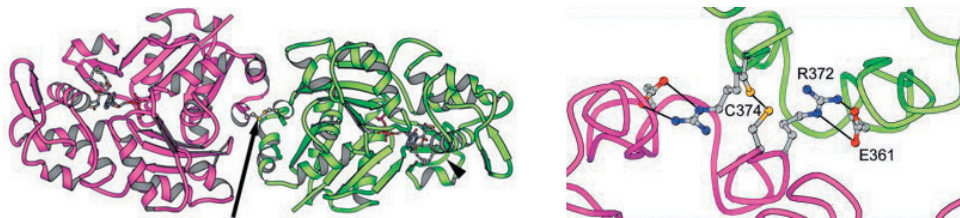




Figure 2. Ribbon-and-strand representation of an antiparallel actin dimer. The individual actin subunits are colored purple and green. On the left, the disulfide bond connecting the subdomains 1 are depicted as ball-and-stick and indicated with an arrow. The arrowhead indicates the DNase I binding loop (subdomain 2). On the right, a close-up view of the dimer interface at the barbed ends of both subunits reveals the disulfide bond between the residues Cys-374 and the four salt bridges between residues Glu-361 and Arg-372 that stabilize the helices of the adjacent subunits. Adapted from Bubb et al. (2002).

Further biochemical characteristics of LD and UD are summarized in Table 1 (Millonig et al. 1988; Hesterkamp et al. 1993; Steinmetz et al. 1997).

Table 1. Biochemical und structural characteristics of the actin LD and UD

	LD	UD
Electrophoretic mobility on SDS-PAGE [kDa]	~ 86	~ 120
Appearance after onset of actin polymerization	early stages	later stages
Life span	transient	persisting
Compatibility with F-actin filament geometry	no	yes
Orientation of subunits	antiparallel	parallel
Cross-linked residues		
Self-assembly into F-actin filaments	no	yes

In conclusion, time-resolved CTEM analysis and chemical cross-linking of polymerizing actin with 1,4-PBM revealed that actin is not only capable to assemble into linear filaments, but also has the intrinsic ability for branching *in vitro*. The experimental data suggest that the transiently formed LD represents a so far undervalued player in the dynamic assembly and turnover of actin networks. Hence, branching and networking of actin in motile cells may not be entirely mediated by actin-associated proteins such as the Arp2/3 complex (Mullins et al. 1998; Pollard et al. 2000; Pantaloni et al. 2001) but might involve transient actin intermediates. It is possible that transiently incorporated LD constitute a platform for the binding of Arp2/3 to commence the formation of daughter filaments *in vivo* (Lassing et al. 2007). Therefore, the principle function of actin-binding proteins could be to act as catalyst or stabilizer for the assembly of suprastructures (Schoenenberger et al. 2002).

1.1.4 Actin polymerization follows a dual pathway

The correlation of LD formation and ragged filament morphology at early stages of polymerization has prompted a refined model for the polymerization of actin (Steinmetz et al. 1997; Schoenenberger et al. 2002). As shown in Figure 3, this model postulates a dual pathway that G-actin can undergo during polymerization into mature F-actin filaments.

The conventional pathway, also termed the 'UD pathway', includes a slow nucleation step during which three activated G-actin moieties assemble to form a nucleus (colored dark grey) that encompasses all the actin-actin contacts present in mature F-actin filaments (Barden et al. 1987).

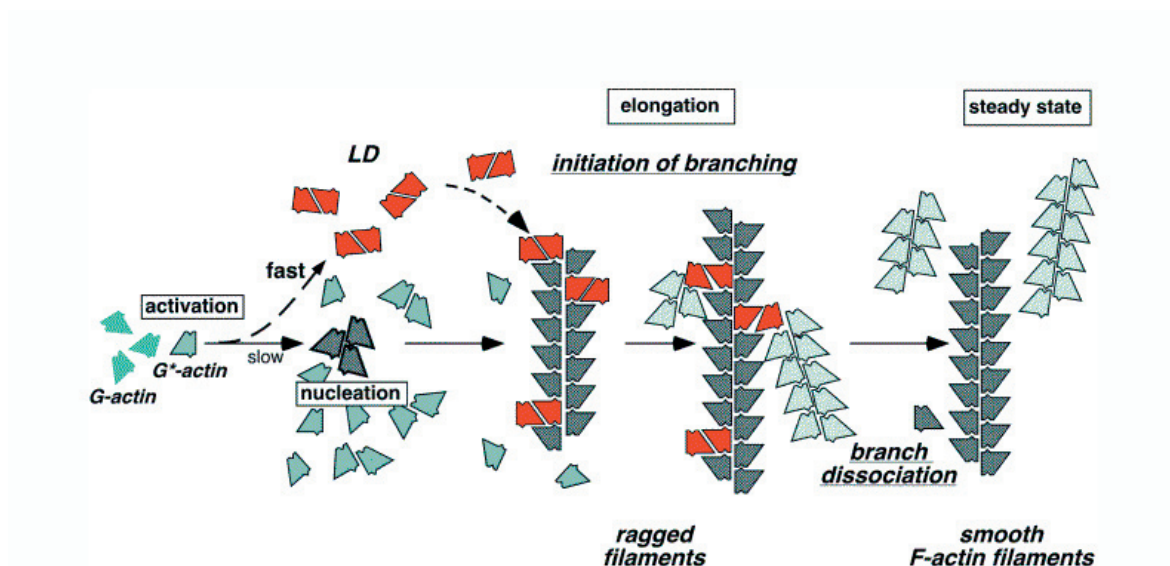


Figure 3. Dual pathway for actin polymerization. The bulk of activated G-actin assembles in a slow reaction to form a nucleus onto which monomeric actin, UD and LD are added. The latter is formed along the fast pathway. At the site of LD incorporation, the growth of a daughter filament might be initiated. However, the integrated LD is not stable and will rapidly dissociate. Finally, both pathways converge and the disperse actin filaments at steady state exhibit an unbranched and smooth morphology. Adapted from Schoenenberger et al. (2002).

Subsequently, the filaments elongate relatively fast through the addition of monomers, small oligomers or UD until elongation of unbranched and smooth filaments ends at steady state.

Following the unconventional pathway, termed the 'LD pathway', which is restricted to a short period of time immediately after the onset of polymerization, G-actin dimerizes in a fast reaction to LD (colored red). When transiently incorporated into growing filaments, the LD subunits which are not involved in filament formation, jut out from the filaments, thereby causing their ragged appearance (Millonig et al. 1988; Steinmetz et al. 1997).

Consistent with this notion, Reutzel and colleagues (2004) suggested that one of the LD subunits is integrated into the growing actin filament, causing a rotational movement between the two monomers of the LD. Moreover, these subunits could serve as origin for the formation of branching daughter filaments (colored light grey). In the absence of accessory proteins, LD are labile and dissociate possibly as a result of a conformational change with ongoing polymerization. In this process, protruding subunits and emerging filament branches would be released. Finally, both pathways converge and all F-actin filaments at steady state exhibit a smooth and unbranched morphology (reviewed by (Schoenenberger et al. 2002)).

1.1.5 LD-like contacts are established in unconventional actin arrays

Because of the transient nature of the LD and because of the lack of suitable tools, it has not been possible to detect this actin species in the complex environment of a cell. However, the existence and functional importance of LD *in vivo* have gained support from a number of studies which show that several actin binding proteins interact with an antiparallel LD-like actin dimer with high affinity (Hesterkamp et al. 1993; Bubb et al. 1994). Studying the nature of the LD in detail would be greatly facilitated by structures with a stable, native arrangement of subunits in LD conformation.

As illustrated in Figure 4, purified muscle actin can form a number of unconventional assemblies given the adequate experimental conditions. For example, two-dimensional crystalline 'sheets' (panel A) and 'tubes' (panel B) form in the presence of the trivalent lanthanide gadolinium (Dos Remedios 1978; Aebi et al. 1980). Moreover, polymerization in the presence of magnesium concentrations above 10 mM will result in tightly packed two-dimensional paracrystalline arrays of actin filaments (panel C; (Fowler and Aebi 1982; Millonig et al. 1988).

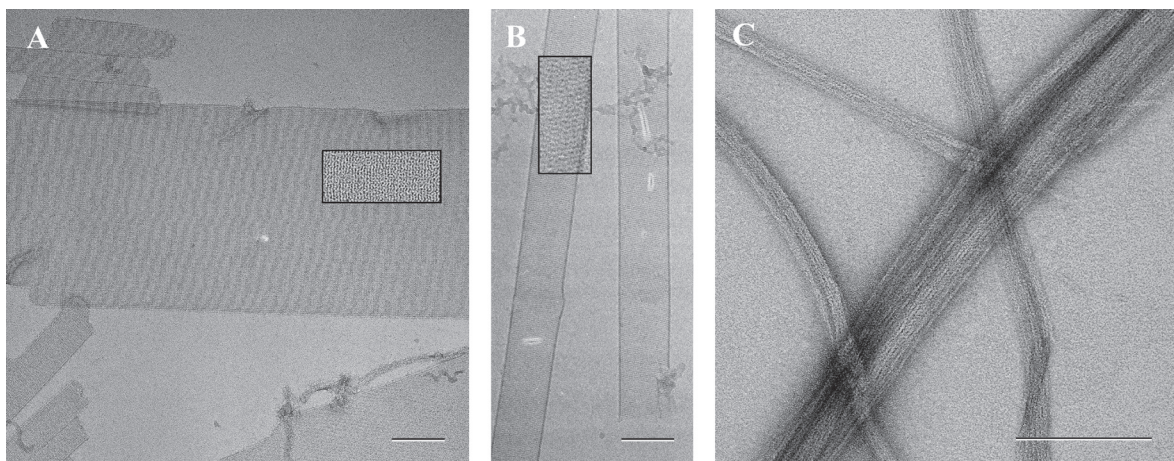


Figure 4. Unconventional actin arrays including LD-like contacts. The formation of actin 2-D crystals (A) 'sheets' and (B) 'tubes' from purified rabbit skeletal muscle actin was induced by gadolinium(III)chloride and KCl. (C) Actin paracrystalline arrays were formed by adding 50mM $MgCl_2$ to G-actin. Inserts display close-up views of the ultrastructural patterning of 2-D crystals. Bars, 200 nm.

Similarly, paracrystalline arrays of F-actin have been formed on positively charged lipid layers composed of phosphatidylcholine (PC) and quaternary ammonium surfactants (Taylor and Taylor 1992).

Interfilament contacts between actin subunits in antiparallel orientation, reminiscent of those occurring in LD, are made possible by the lateral alignment of F-actin filaments with

opposite polarity. Consistent with this notion, 1,4-PBM cross-linking of paracrystalline arrays yields a substantial amount of LD and polymerization in the presence of 50 mM magnesium reveals that cross-linked LD persists at steady state (Millonig et al. 1988).

Similar results were obtained when gadolinium-induced actin 2-D crystals were cross-linked (Millonig et al. 1988), suggesting that some of the contacts in sheets represent the LD conformation.

By fitting the atomic structure of the G-actin monomer (Kabsch et al. 1990) into an EM-based 3-D reconstruction obtained from negatively stained actin 'tubes', Steinmetz and colleagues (1998) confirmed that actin crystals include antiparallel packing of subunits into dimers which are reminiscent of the LD, and that the LD is compatible with the unit cell structure and symmetry of the crystals. Moreover, similar to LD, most of the intersubunit contacts within or between the dimers in a 2-D crystal are not compatible with the F-actin filament symmetry (Aebi et al. 1980; Aebi et al. 1981; Smith et al. 1983; Steinmetz et al. 1998; Schoenenberger et al. 1999).

Because these unconventional synthetic actin polymers represent stable arrays of LD-like subunit arrangement they lend themselves to further characterization of the structure and function of the LD.

1.2 Aims of project

The fundamental idea of this study was to gain insight into the role of the LD in actin patterning. Moreover, we aimed at overcoming the transient nature of LD and producing supramolecular actin structures with persisting LD subunit contacts. These structures should prove useful to test the specificity of antibodies raised against the LD conformation of actin.

1.3 Materials and methods

Preparation of monomeric actin (G-actin)

Rabbit skeletal muscle actin was extracted from acetone powder (Spudich and Watt 1971). The resulting F-actin filament pellet was resuspended in monomer buffer A (2.5 mM imidazole, 0.2 mM CaCl₂, 0.2 mM ATP disodium salt, 0.005% NaN₃, 0.2 mM DTT, pH 7.2 - 7.4) and dialyzed with vigorous stirring against buffer A at 4°C for 72 hrs with daily buffer changes. The G-actin was centrifuged at 100.000 g for 2 hrs to remove oligomeric actin and the upper 3/4 of the supernatant was separated by gel filtration chromatography on an equilibrated (buffer A) Superdex™ 200 prep grade HiLoad™ 26/60 column (Amersham Biosciences) at a flow rate of 1 ml/min in buffer A. Eluted fractions of 2.5 ml were collected and the peak fractions were analyzed by SDS-PAGE. The protein concentration of monomeric peak fractions was determined by measuring the absorbance at 280 nm. Monomeric G-actin was stored in buffer A at 4°C and used within 2 weeks.

Intermolecular cross-linking of G-actin with N,N'-1,4-phenylenebismaleimide

Intermolecular cross-linking of G-actin with sulfhydryl reagent N,N'-1,4-phenylenebismaleimide (1,4-PBM) was carried out essentially as described (Millonig et al. 1988; Steinmetz et al. 1997). All reagents were freshly prepared and kept at 4°C. Briefly, 1,4-PBM was dissolved in dimethylformamide (DMF) at 5 mM and diluted in 20 mM sodium borate, pH 9.5, containing 100 mM KCl and 0.2 mM CaCl₂, prior to use.

To optimize the yield of LD, polymerization of freshly isolated G-actin (1 - 1.5 mg/ml) was induced by the addition of CaCl₂ to a final concentration of 20 mM, and cross-linking was immediately initiated by the addition of an equal volume of 1,4-PBM diluted in 20 mM sodium borate, 20 mM of CaCl₂, pH 9.5, to achieve a final molar ratio of 0.5:1 1,4-PBM/actin. The reaction was quenched after 20 min at room temperature by the addition of 0.001 v/v β-mercaptoethanol. The efficiency of cross-linking was monitored by SDS-PAGE and subsequent Coomassie Brilliant blue staining (Figure 5).

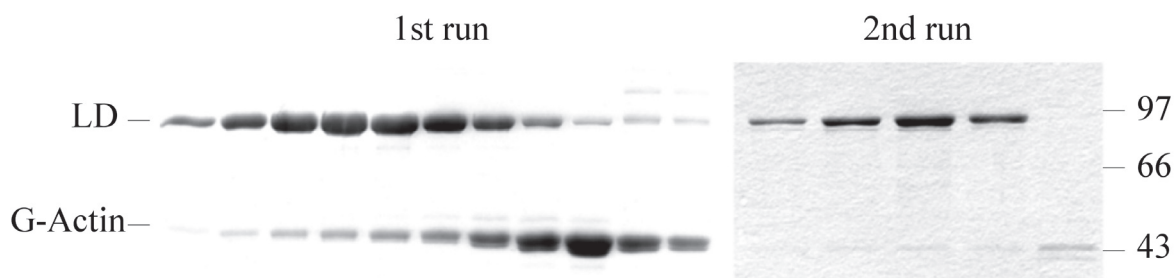


Figure 5. Purification of cross-linked LD by gel filtration chromatography. SDS-PAGE of consecutive fractions indicates that an efficient separation of the intermolecularly cross-linked LD from the intramolecularly cross-linked actin moiety requires repeated runs on a Superdex 200 column. After the first run, fractions containing mostly LD were combined, concentrated and re-chromatographed. After the 2nd run (right panel), peak fractions contained only small amounts of monomeric actin (> 1%). The molecular masses in kDa of standard proteins are indicated on the right.

Purification of the actin 'lower dimer' (LD)

The covalently cross-linked actin solution was dialyzed against buffer A at 4°C for at least 36 hrs with several buffer changes and then centrifuged at 100,000 g for 2 hrs in a swing-out rotor. To purify LD, the upper 3/4 of the solution was separated by gel filtration chromatography on a Superdex 200 (26/60) column equilibrated in buffer A at a flow rate of 1 ml/min. The eluent was collected in 2 ml fractions.

The peak fractions were analyzed by SDS-PAGE (Figure 5). Fractions containing > 80% LD were pooled and re-chromatographed to further reduce contaminating, intramolecularly cross-linked monomeric actin. Finally, fractions containing ~ 95% pure cross-linked LD were used for copolymerization assays with G-actin. The protein concentration of the LD was determined by measuring the absorbance at 280 nm.

Copolymerization of cross-linked LD and G-actin

Different ratios of purified cross-linked LD and monomeric G-actin were mixed and then polymerization was induced at room temperature by the addition of salt to a final concentration of either 100 mM KCl or 2 mM MgCl₂/50 mM KCl, and a twofold molar excess of phalloidin over actin where indicated. After 2 hrs, the polymerization reaction was analyzed by a standard pelleting assay as schematically illustrated in Figure 6. Briefly, the total polymerization reaction 'T' was centrifuged at 100,000 g at 4°C for 1 hr yielding a supernatant (S) that contains non-polymerized actin and small oligomers and a pellet fraction (P) with filamentous actin.

The supernatant was removed and the pellet was washed in the one volume of polymerization buffer F (buffer A containing either 100 mM KCl or 2 mM MgCl₂/50 mM KCl). After washing, the pellet was gently resuspended in one volume of buffer F and incubated for at least 1 hr at 4°C.

Corresponding aliquots of the total protein input 'T', the high-speed supernatant 'S' and the resuspended pellet 'P' were analyzed on 12% SDS-PAGE gels by Coomassie Brilliant blue staining. In addition, aliquots of 'P' were examined by CTEM and STEM (see below).

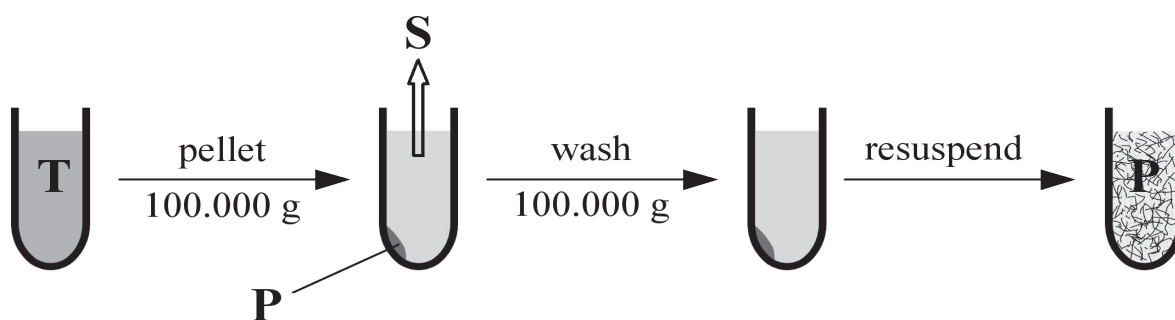


Figure 6. Schematic representation of the standard pelleting assay.

Preparation of actin 2-D crystals

The preparation of two-dimensional actin crystals has been previously described (Dos Remedios 1978; Aebi et al. 1981). Briefly, G-actin (1.0 - 1.5 mg/ml in buffer A) was dialyzed in a 0.25-inch diameter dialysis tubing with a molecular weight exclusion limit of 12,000 Da against 'prepolymerization buffer' (2.5 mM imidazole, 0.5 mM CaCl₂, 0.25 mM dithiothreitol, 0.005% NaN₃, pH 7.25) for 5 hrs at 4°C. The dialysis bag was then carefully transferred to two liters of 'crystallization buffer' (2.5 mM PIPES, 0.25 mM dithiothreitol, 0.005% NaN₃) containing 25 mM KCl and a 5:1 molar ratio GdCl₃ over actin ('sheet' conditions) or 75 mM KCl and a 9:1 molar ratio GdCl₃ over actin for ('tube' conditions) for at least 6 hrs at 4°C with minimal agitation. The 2-D crystals were processed within 24 hrs.

Conventional Transmission Electron Microscopy (CTEM)

For specimen preparation, carbon-coated 200 mesh/inch copper grids for CTEM were rendered hydrophilic by gentle glow discharge in air at low pressure. 5 μ l sample droplets were then adsorbed to the grids for 30 - 60 s, washed four times with double-distilled water to remove salts, and subsequently negatively stained with 2% uranyl acetate, pH 4.5, for 10 s according to standard protocols (Harris and Agutter 1970; Aebi et al. 1981). Analogue high resolution micrographs were taken at a nominal magnification of 50.000x on Hitachi H 7000 and H 8000 microscopes at acceleration voltages of 100/200 kV. Low-resolution images were taken on a fully digitalized FEI Philips Morgagni 268D at an acceleration voltage of 80 kV.

Scanning Transmission Electron Microscopy (STEM)

STEM analysis of negatively stained specimens was performed as described previously (Muller and Engel 1998; Muller and Engel 2001). Briefly, aliquots of the resuspended pellet fractions from copolymerization experiments were adsorbed for 1 min to freshly glow discharged thin carbon film that spanned a thick fenestrated carbon layer covering a gold-plated copper microscopy grid. The specimens were washed on four drops of quartz bi-distilled water, negatively stained with 0.75% uranyl formate, pH 4.25, and air dried. Images were recorded with the STEM (STEM HB5; Vacuum Generators, East Grinstead, England) operated at an accelerating voltage of 100 kV and a nominal magnification of 500.000x.

Mass determination by STEM

For mass-per-length measurements (MPL), 5 μ l aliquots of the sample were adsorbed for 1 min to glow discharged STEM microscopy films; thin carbon films that spanned a thick fenestrated carbon layer covering 200-mesh/inch, gold plated copper grids. The grids were then blotted and washed on four drops of quartz bi-distilled water to remove buffer salts, and freeze-dried at -80°C and $5 \cdot 10^{-8}$ Torr overnight in the microscope.

Tobacco mosaic virus (TMV) particles served as mass standard. These were similarly adsorbed to separate microscopy grids, washed on four droplets of 10 mM ammonium acetate, air-dried and placed in the microscope together with the sample.

Digital STEM dark-field images were recorded using a Vacuum Generator HB-5 STEM interfaced to a modular computer system (Tietz Video and Image Processing Systems GmbH, D-8035 Gauting) operated at an accelerating voltage of 80 kV and a nominal magnification of 200.000x. Mass loss induced by the electron beam was experimentally determined as described previously (Engel 1978; Muller et al. 1992).

The mass analysis was carried out using the IMPSYS program package as detailed in (Engel and Reichelt 1988; Muller et al. 1992). Accordingly, filament segments were manually selected in square boxes and tracked. The total scattering of each filament region was then calculated and the scattering of the supporting carbon film deducted. Division by the filament length gave the MPL. The resulting values were scaled according to the mass measured for TMV and corrected for beam-induced mass loss (Muller et al. 2001). The mass values were then displayed in histograms and described by Gauss curves.

Width measurement of actin filaments

The widths of actin filaments were measured manually from uncompressed digital STEM electron micrographs of negatively stained specimens (see above) using the image processing and analysis software ImageJ. Width measurements were carried out on both, conventional F-actin filaments that were polymerized from G-actin and hybrid actin filaments that were copolymerized from G-actin and LD. The filament widths were measured perpendicular to the filament axis at the sites of maximal width between two consecutive crossovers of the two long pitch helical strands. In the case of laterally protruding protein, the maximum widths of the filaments with and without the protrusion were measured.

1.4 Results

1.4.1 Copolymerization of G-actin and cross-linked actin 'lower dimer' (LD)

In the present study we copolymerized G-actin and covalently cross-linked LD in varying ratios in the presence of 100 mM KCl and a twofold molar excess of phalloidin. Phalloidin, a bicyclic heptapeptide toxin of the toadstool *Amanita phalloides* (Wieland and Faulstich 1977; Wieland and Faulstich 1978) blocks actin subunits in F-actin filaments and prevents monomer release from the filaments ends (Estes et al. 1981; Coluccio and Tilney 1984). The incorporation of LD into filamentous structures was biochemically analyzed by high-speed pelleting assays and subsequent SDS-PAGE and visualized by CTEM.

1.4.2 G-actin and cross-linked LD cosediment in high-speed pelleting assays

G-actin and cross-linked LD mixed at different ratios were copolymerized for one hour at room temperature and then centrifuged at 100.000 g in order to separate unpolymerized (supernatant) from polymerized or aggregated protein (pellet). Subsequently, aliquots of the total protein input (T) at the onset of polymerization and the supernatant (S) and the resuspended pellet fraction (P) at steady state were separated on a 12% SDS-PAGE gel and stained with Coomassie Brilliant Blue.

As documented in Figure 7, at steady state, the native actin pool was entirely pelleted in the absence, but also in the presence of LD. Copolymerization of native actin and LD at a molar ratio of 10.5:1.8 [μM] yielded pellets that contained LD in addition to the native actin with virtually no protein in the supernatant. Increasing the fraction of LD lead to a higher amount of LD in the pellet. At the same time, the amount of LD that remained in the supernatant slightly increased. In the absence of native actin (panel on the far right), addition of 100 mM KCl and phalloidin did not induce significant amounts of LD-structures that pelleted at high speed, and most of the LD stayed in the supernatant.

In conclusion, the high-speed pelleting experiments suggest that cross-linked LD is able to copolymerize with native actin into filamentous structures. Considering that the LD might interfere with the formation of actin filaments, we cannot rule out that the pellets represent unstructured aggregates rather than filaments, although the control experiment with purified LD alone indicates that LD does not form aggregates under the given salt conditions. Hence, in Chapter 1.4.3 the pellet factions containing cosedimented actin and LD were further examined by CTEM.

Corresponding pelleting experiments were carried out in the absence of phalloidin. In contrast to the experiments with phalloidin, SDS-PAGE analysis revealed that the initial G-actin fraction was not entirely polymerized and pelleted in the presence of the LD (data not shown).

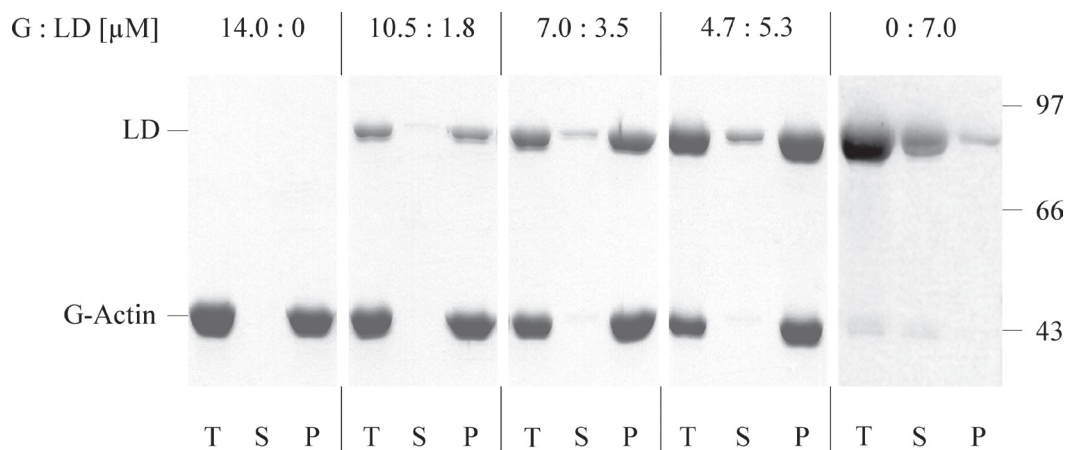


Figure 7. Cosedimentation of native actin and cross-linked LD. Different ratios of G-actin:LD (indicated in the top line) were copolymerized by the addition of salt to a final concentration of 100 mM KCl and a 2:1 molar excess of phalloidin over actin. After centrifugation at 100.000 g, samples were washed and resuspended in the initial volume with filament buffer. Aliquots of the total protein input (T), the supernatant after high-speed centrifugation (S) and the resuspended pellet fractions (P) were separated on a 12% SDS-PAGE gel and stained with Coomassie Brilliant Blue. In the presence of native actin, LD was predominantly found in the pellet fraction whereas without actin, LD remained mostly in the supernatant. The molecular masses in kDa of standard proteins are indicated on the right.

1.4.3 The incorporation of cross-linked LD alters the morphology of actin filaments

For CTEM analysis, aliquots of the resuspended pellet fractions from copolymerization of G-actin with different amounts of cross-linked LD were adsorbed to EM-grids and negatively stained with 2% uranyl acetate. Micrographs representing the cosedimented fraction from different actin:LD ratios are shown in Figure 8. As expected, high-speed centrifugation of G-actin polymerized without LD (Figure 8 A) yielded the highly ordered, smooth F-actin filaments that are described in the literature (Millonig et al. 1988; Milligan et al. 1990; Schoenenberger et al. 1999). Typically, crossovers are spaced regularly along the filaments and subunits appear well-aligned within the helices. Figure 8 B displays filaments from copolymerization of G-actin and LD at a molar ratio of 10.5:1.8. Consistent with the biochemical analysis that suggested a copolymerization of LD and actin (Figure 7), these filaments appear less straight and slightly irregular compared to bona fide F-actin filaments in panel A. In particular, regular crossover spacings are less evident. With increasing amounts of LD present at the onset of copolymerization, the subtle alterations of the filament architecture became more pronounced. At a molar ratio of 7.0:3.5 actin:LD (Figure 8 C), the overall contour of the filaments appeared to be more ragged.

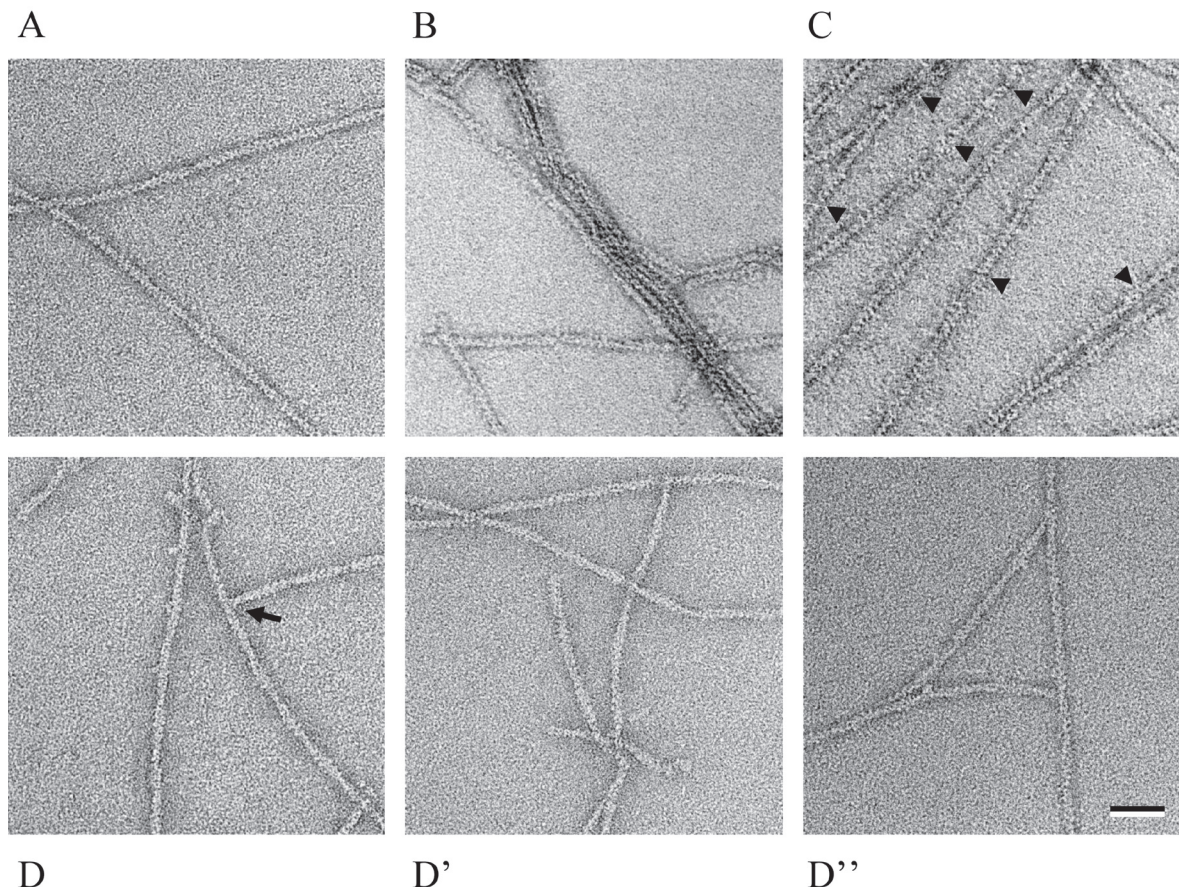


Figure 8. CTEM micrographs of copolymerized native actin and cross-linked LD. Varying ratios of G-actin: LD were copolymerized by adding 100mM KCl and a 2:1 molar ratio of phalloidin over actin. Negatively stained specimens of resuspended high-speed pellet fractions are shown. F-actin filaments (A), copolymerization of G-actin and LD at molar ratio of 10.5:1.8 (B), 7.0:3.5 (C) and 4.8:5.3 (D - D''). Arrowheads in (C) point to disruptions of the filament structure. Arrow in (D) marks a possible branching site. Bar, 50 nm.

Typically, small lateral protrusions were jutting out from the filaments and disruptions occurred along the filament axis. At a slight molar excess of LD over actin (5.3:4.8), lateral protrusions were more frequent (Figure 8 D - D'') and the regular substructure of F-actin filaments (Figure 8 A) was no longer detectable. Remarkably, several cases of junctions where two filaments are linked were observed. In most instances, one of the filaments terminated at the junction, which might indicate that this structure represents a branching site rather than two random filaments crossing each other.

Together, biochemical and electron microscopic studies showed that copolymerization of G-actin and cross-linked LD in the presence of phalloidin lead to the stable incorporation of LD into actin filaments. With increasing amounts of LD, the filament morphology was significantly altered. In particular, the substructure characteristic for F-actin filaments was perturbed and small lateral protrusions were prominent.

Moreover, at high levels of LD, the fraction of un-incorporated LD increased, indicating that LD-incorporation is only tolerated to a certain extent. Consistently, filamentous structures were no longer observed in mixtures with a large excess of LD over actin. This finding suggests that a minimal number of proper actin subunit interactions are needed to allow for filament formation in the presence of LD. Moreover, numerous cases of filaments ending at the side of other filaments suggest that LD incorporation is conducive to branching.

For a more detailed structural analysis of the effects of LD incorporation on F-actin filament architecture, we processed the hybrid filaments for scanning transmission electron microscopy (STEM) analysis.

1.4.4 Scanning transmission electron microscopy (STEM)

In STEM technology, a field emission gun produces an electron beam with a narrow energy distribution allowing the electrons to be focused to a sharp point. The rastering of the beam over the sample in combination with a high-angle detector capable of counting single electrons allows for mass measurements and the generation of mass maps. Moreover, the highly sensitive detector system and thin carbon support films used, result in a high signal to noise ratio allowing even unstained protein to be detected and quantitatively measured (Muller et al. 1996). Because STEM simultaneously provides images and quantitative data, it is invaluable for structure determination. Its most successful application is the mass determination and mass mapping of protein complexes and supramolecular structures.

We used STEM to compare the morphology of conventional F-actin filaments with that of hybrid filaments containing actin and LD subunits. The specific focus was to investigate the mass-per-length (MPL) of hybrid filaments and compare it to that of conventional F-actin filaments. Based on previous findings, we assumed that the incorporation of dimeric actin protomers in hybrid filaments should result in a higher MPL, and that the MPL difference between both filament types would provide more information of the actual incorporation rate of LD in hybrid filaments.

Moreover, by analyzing digital STEM images of negatively stained specimens we intended to obtain a more detailed picture of the morphological changes brought about by the LD incorporation.

1.4.4.1 Mass-per-length measurements of unstained F-actin and hybrid filaments

For mass-per-length measurements (MPL) of unstained specimens, a droplet of the resuspended pellet fractions from copolymerization of actin and cross-linked LD in the presence of phalloidin (see Chapter 1.3) was adsorbed to glow discharged STEM grids. After removal of buffer salts, the specimens were freeze-dried in the microscope.

To examine the effect of LD incorporation in actin filaments, we compared the MPL of unstained F-actin filaments and hybrid filaments, which were copolymerized from G-actin and LD. We mainly focused on hybrid filaments, which were copolymerized from G-actin and LD at a molar ratio of 4.8:5.3 μM , because they frequently exhibit lateral protrusions.

For analysis, square boxes (80 pixel²) containing filament segments were manually selected from digital STEM dark-field images and the MPL and the full-width half-maximum (FWHM) of the filament segments were calculated computationally. MPL-data describe the calculated entire signal curve of an object, whereas the FWHM-data depict the width of the signal curve at its half maximum value. For circular and tubular objects, the analysis of the FWHM is a valid alternative to the MPL, because by excluding the information at the periphery of the objects measured inaccurate data analysis at the blurred and noisy edges is avoided.

Table 2 displays the data obtained from STEM analysis for both conventional F-actin and hybrid filaments.

Table 2. MPL and FWHM of F-actin filaments and hybrid filaments determined by STEM

	F-actin filaments (n = 65)	Hybrid filaments (n = 69)
Average MPL [kDa/nm]	14.7	14.6
SD	1.4	1.3
Gaussian peak MPL [kDa/nm]	14.6	14.6
SD	1.3	1.3
FWHM [nm]	7.8	8.0
SD	0.7	0.8

n, number of measuring points; *MPL*, mass-per-length;

SD, standard deviation; *FWHM*, full-width half-maximum

The average MPLs of F-actin filaments (14.7 kDa/nm) and hybrid filaments (14.6 kDa/nm) were similar. Surprisingly, a slight MPL decrease was recognized for hybrid filaments. In related experiments using different conditions for F-actin filament and hybrid filament polymerization (data not shown), we observed a similar tendency for MPL values to decrease as a result of LD incorporation.

Figure 9 depicts that the MPL of both filament types distribute almost congruent within the Gaussian curve. Depending on the X-axis scale factor used, the Gaussian peak for hybrid filaments fits between 14.50 - 14.55 kDa/nm. For F-actin filaments, the Gaussian peak was always 14.60 kDa/nm. Moreover, the FWHM of hybrid filaments (8.0 nm) and F-actin filaments (7.8 nm) is almost identical.

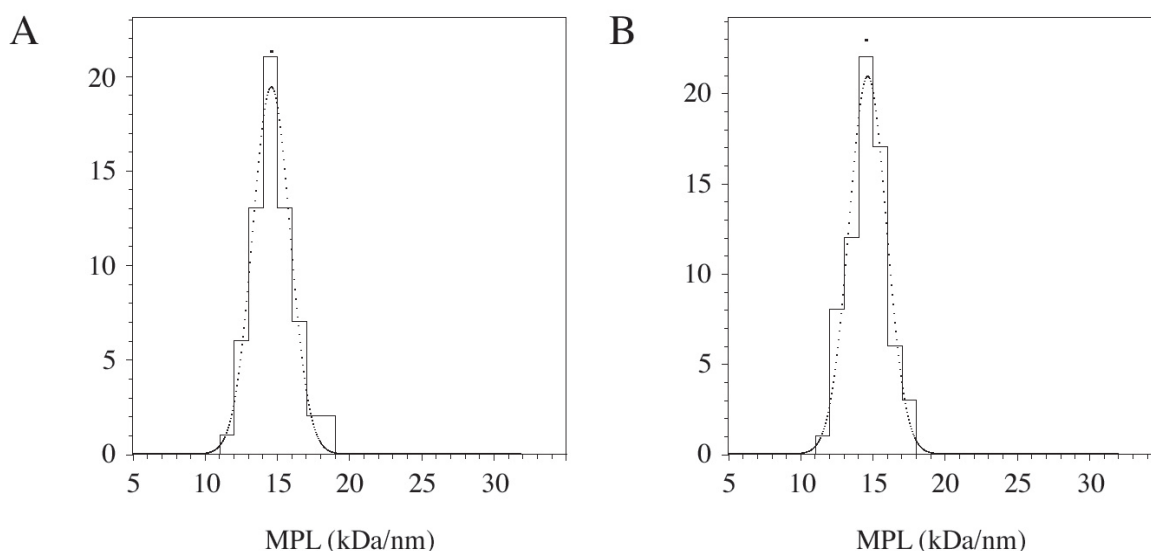


Figure 9. MPL analysis of F-actin filaments and hybrid filaments. MPLs of (A) native F-actin filaments and (B) hybrid filaments that were copolymerized from G-actin monomers and LD in a molar ratio of 4.7:5.3 μ M. The Gaussian fits (indicated by the dotted lines) reveal no MPL differences between the two types of filaments. The ordinate displays the number of boxes; MPL, mass-per-length.

Contrary to the biochemical evidence and CTEM analysis which clearly demonstrate the co-polymerization of LD and actin into hybrid filaments with an altered geometry, STEM data did not reveal any difference between MPL and FWHM in hybrid versus conventional F-actin filaments.

It appears that those two parameters are not suitable to characterize the consequences of LD incorporation on filament geometry.

1.4.4.2 Highly ordered F-actin filaments versus morphologically altered hybrid filaments visualized at high magnification

In order to evaluate the structural impact of LD in hybrid filaments in detail, we examined negatively stained specimens from resuspended pellet fractions of copolymerized actin and cross-linked LD and actin (see Chapter 1.3) at a nominal magnification of 500.000x by STEM. A gallery of highly magnified, inverted STEM micrographs is shown in Figure 10.

The highly ordered structure of conventional F-actin filaments assembled from native G-actin is presented in panel A. The smooth appearance and the constant diameter of the filaments, as well as the regular crossover repeats and homogenous staggering of subunits along the longitudinal filament axis, confirm the proper assembly of monomers into bona fide F-actin filaments.

In contrast, the hybrid filaments resulting from copolymerization of G-actin and LD at a molar ratio of 4.8 μM :5.3 μM , characteristically displayed some unique features, namely lateral protrusions (Figure 10 B) and branching (Figure 13). The hybrid filaments revealed irregular staggering of subunits and numerous prominent lateral protrusions that were irregularly spaced along the filament axis and resulted in a ragged appearance accompanied by an increase of the average filament diameter. Although some of the protrusions seemed to be associated with the filament rather loosely, the majority were actual constituents of the filament structure.

1.4.4.3 Width measurement of negatively stained F-actin and hybrid filaments on highly magnified STEM images

To determine the width at different sites of hybrid and conventional F-actin filaments, the image processing and analysis software ImageJ was used. In particular, the width at individual sites between two recognizable crossovers of the long-pitch helical strands was measured perpendicular to the filament axis. Only filament sections that lacked morphological disruptions such as breaks, were considered.

At the sites selected, filaments exhibited either a smooth morphology or a laterally protruding structure. In the latter case, a corresponding hypothetical filament width excluding the protrusion was also determined. Occasionally, the prevailing smooth morphology of the conventional F-actin filaments also appeared to be interrupted by a protrusion. Based on several earlier studies which demonstrate conventional F-actin filaments at steady state exhibiting a smooth morphology (Steinmetz et al. 1997), we concluded that the lateral protrusions in our F-actin filament preparation represent an artifact caused by free protein that randomly associated with the filaments. For this reason, the particular data points were not considered in the statistical calculations of the width of conventional F-actin filaments.

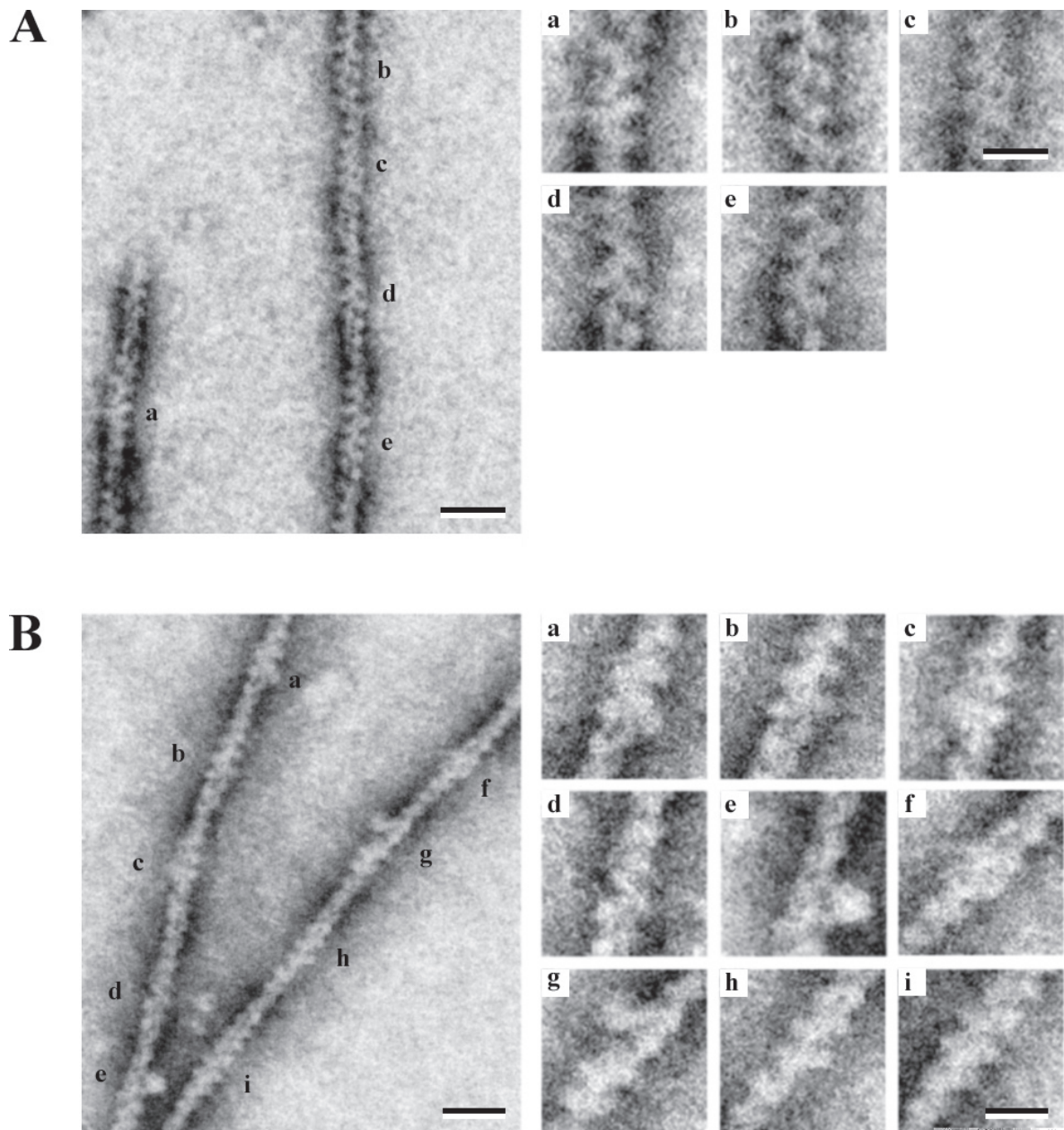


Figure 10. STEM analysis of negatively stained specimens from copolymerization of cross-linked LD with native actin. Copolymerization of cross-linked LD with native actin was induced by the addition of salt to a final concentration of 100 mM KCl in the presence of a 2:1 molar ratio of phalloidin over actin. The filaments were centrifuged at high speed (100,000 g), resuspended and then processed for STEM analysis. In (A), F-actin filaments from polymerization of pure G-actin exhibit a smooth morphology with a highly ordered substructure. (B) If native actin and LD were copolymerized at a molar ratio of 4.8:5.3, filaments display abundant lateral protrusions. Bars in A, B, 20 nm; in galleries, 10 nm. The individual sites of width measurements are marked with lower case letters and shown at higher magnification in the adjacent galleries. Note the lateral protrusions that emanate from hybrid filaments in (B)a, e and g.

As illustrated in Table 3, 152 individual measurements were collected for conventional F-actin filaments and 165 for hybrid filaments. The width of hybrid filaments ranged from 4.76 to 17.90 nm. As a result of LD incorporation, width variability of hybrid filaments is significantly larger compared to smooth F-actin filaments, which range from 7.98 to 16.23 nm in width.

Table 3. Width measurements of conventional F-actin filaments and hybrid actin filaments

	F-actin filaments (n = 152)	Hybrid filaments (n = 165)
Filament width [nm]	7.98 - 16.23	4.76 - 17.90
Average filament width [nm]	10.58	11.63
SD	1.25	1.86

n, number of measuring points; *SD*, standard deviation

Moreover, consistent with a high frequency of lateral protrusions, a 9.9% increase in the average width was detected in hybrid filaments (11.63 nm) compared to that of F-actin filaments (10.58 nm). Statistical analysis using the unpaired t-test revealed this increase to be statistically extremely significant ($p < 0.0001$).

Figure 11 displays the width distribution at 0.3 nm intervals for both types of filaments. Note that for hybrid filaments only the data from width maxima at sites containing lateral protrusions were included, not the hypothetical filament width lacking these protrusions.

The width distribution measured from F-actin filaments ranges predominantly from 8.71 - 12.90 nm, with a maximum frequency between 9.01 - 11.40 nm. In contrast, hybrid filaments exhibited a more even width distribution over the entire range with a slight clustering between 9.01 and 13.80 nm.

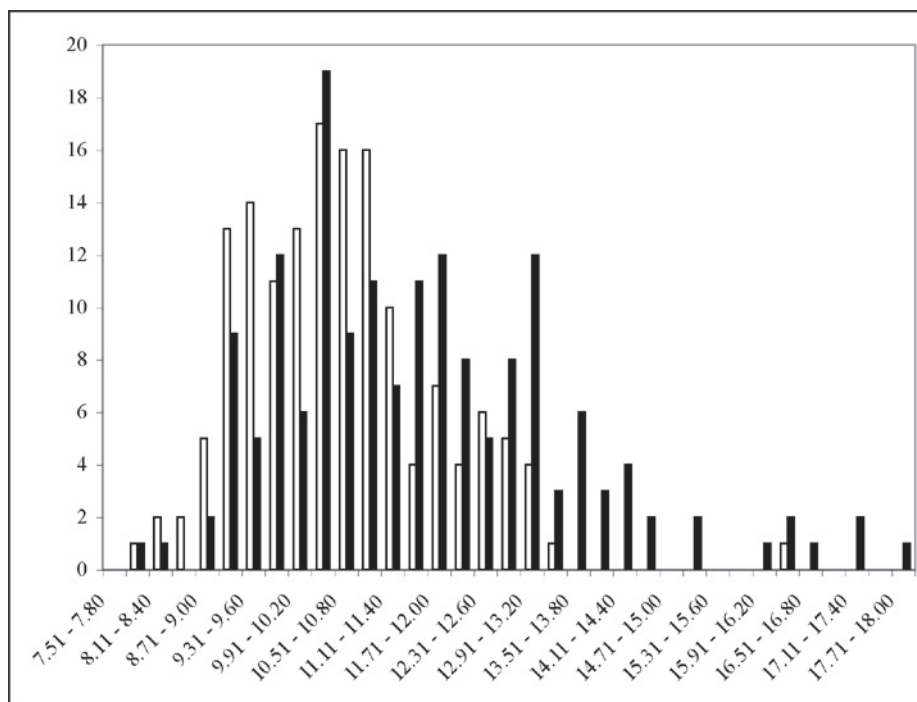


Figure 11. Width distribution of F-actin and hybrid filaments. Width frequencies were plotted at 0.3 nm intervals. White bars represent F-actin filaments; black bars, hybrid filaments.

In the following we evaluated the width of the lateral protrusions in hybrid filaments. 66 individual protrusions were analyzed (Table 4).

Table 4. Width measurements of lateral protrusions from hybrid filaments

	Lateral protrusions (n = 66)
Width [nm]	1.54 - 6.92
Average width [nm]	3.66
SD	1.35

n, number of measuring points; *SD*, standard deviation

The average width of the lateral protrusions measured 3.66 nm. Although the maximal distance from the filament surface was 6.92 nm, 90.9% of the protrusions did not extend more than half of the average diameter of hybrid filaments without protrusions (10.87 nm/2=5.44 nm). The dimension of the average protrusion corresponds well with the dimensions of an actin subunit. Thus, it is conceivable that the protrusion represents the free actin subunit of the incorporated LD that is jutting out from the filament.

A comparison of the width of F-actin filaments and hybrid filaments measured at sites without lateral protrusions (Table 5) revealed only a minor difference between the two diameters, which was not significant according to unpaired t-test ($p = 0.860$).

Table 5. Width measurements of conventional F-actin filaments and hybrid filaments without lateral protrusions

	F-actin filaments (n = 152)	Hybrid filaments (n = 99)
Width [nm]	7.98 - 16.23	8.37 - 17.25
Average filament width [nm]	10.58	10.87
SD	1.25	1.38

n, number of measuring points; *SD*, standard deviation

This finding supports the notion that the LD incorporation along hybrid filaments occurs at random: some filament segments frequently exhibit laterally protruding LD subunits whereas others have a smooth contour and highly ordered substructure comparable to that of F-actin filaments.

Another striking effect of LD incorporation was the perturbation of the crossover repeats of the long-pitch helical strands in hybrid filaments. An extreme example of a hybrid filament segment lacking any evidence of a crossover is shown in Figure 12. It is conceivable that the absence of helical structure in this filament segment prevented phalloidin from binding the hybrid filament. As a result, both monomeric (asterisks) and dimeric (arrowheads) protomers possibly dissociated, leading to a high background staining.

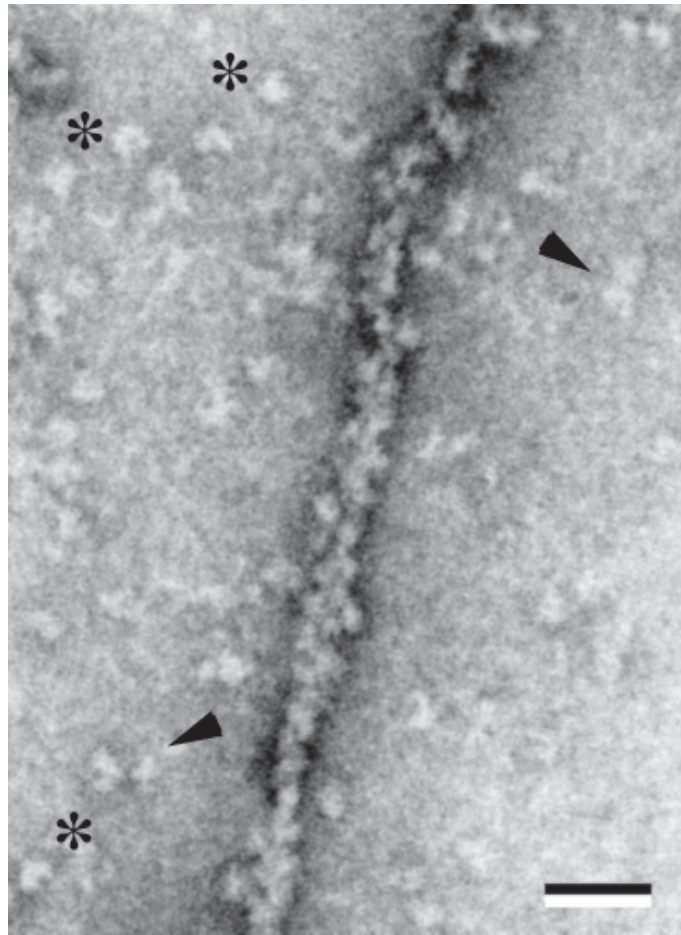


Figure 12. Perturbation of crossover repeats in hybrid filaments. Native actin and LD were copolymerized at a molar ratio of 4.8:5.3. The filament displays a perturbed morphology lacking axial repeats. Dissociated protein moieties cover the EM-grid. Potential actin monomers and antiparallel dimers are indicated by asterisk and arrowheads, respectively. Bar, 10 nm.

Because the axial repeats in hybrid filaments often could not be localized, a general comparison with the regular repeats in F-actin filaments is not possible. However, segments of hybrid filaments that are devoid of lateral protrusions, exhibited axial repeats comparable to those of F-actin filaments.

Another noteworthy feature of hybrid filaments is the occurrence of 'daughter' filaments that appear to emanate from the 'mother' filament at different angles. An example of such a filament that seems to be branching off another filament at an angle of approximately 90° is shown in Figure 13. At the interface of the two filaments, a prominent horseshoe-like subunit, which is reminiscent of the shape of an actin monomer, encompassed a lateral protuberance of the adjacent filament. Although the exact origin of the protomers at the contact site is unclear, they evidently establish contacts between two filaments, which is consistent with the notion of branching. We cannot rule out that mechanical forces during sample preparation have destroyed many of these delicate structures, rendering a detailed examination of the branching rate unfeasible.

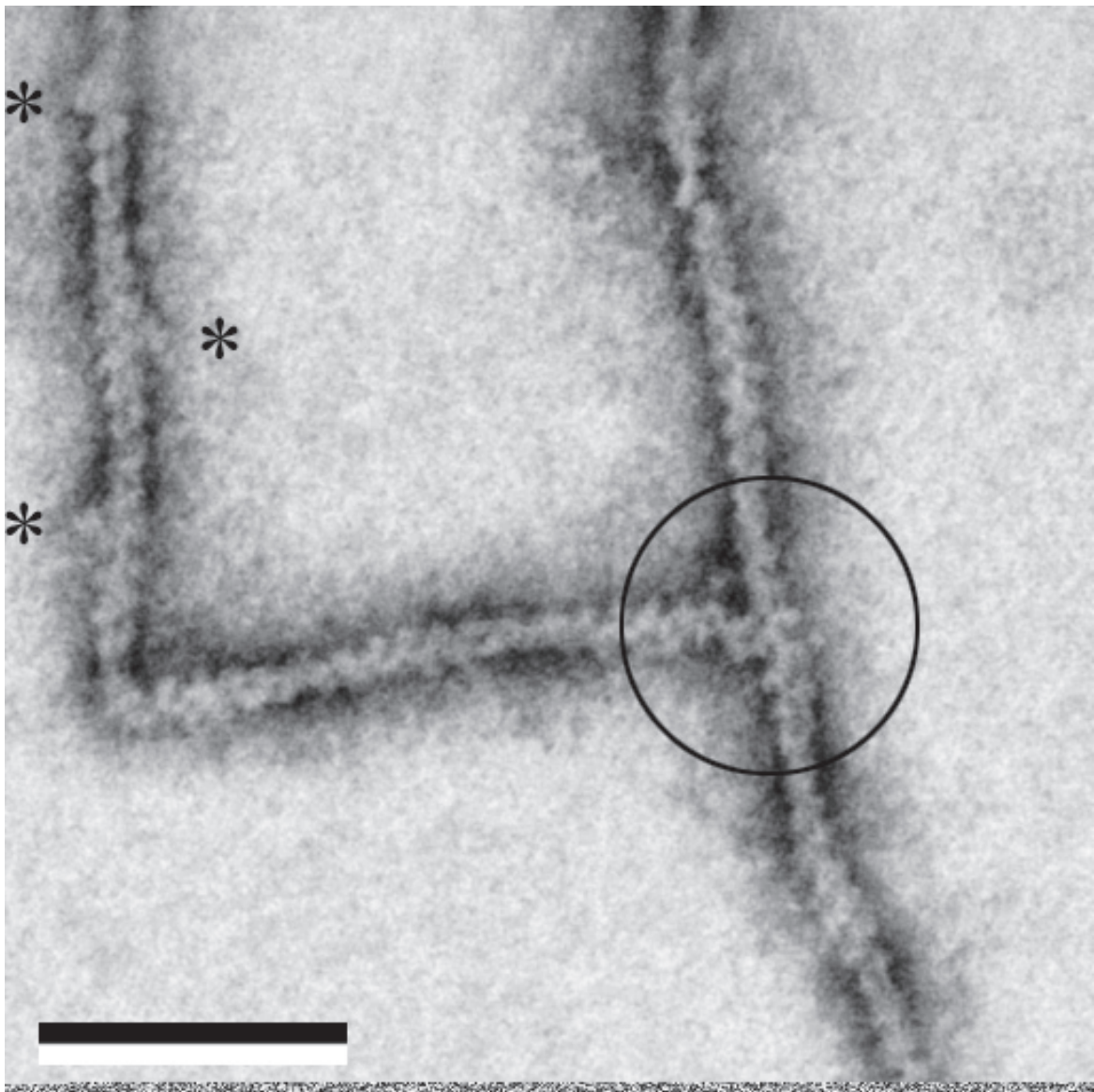


Figure 13. Branching of hybrid filaments. At the interface of the two filaments (circle), a prominent horseshoe-like subunit, which is reminiscent of the shape of an actin monomer, encompasses a lateral protuberance of the adjacent filament. Prominent lateral protrusions (asterisks) approximately extend to half of the filament diameter. Bar, 20 nm.

In summary, ultrastructural analysis by electron microscopy showed that the copolymerization of cross-linked LD with actin produced filamentous structures with randomly incorporated LD. STEM data revealed that incorporated LD on one hand perturbed the spatial packing of the actin subunits in the filaments, and on the other hand, their laterally protruding free subunits led to a ragged appearance of the hybrid filaments. Consistent with the notion that the protruding LD subunit might trigger a branching event, we observed an increased incidence of hybrid filaments that were linked at different angles. In addition,

hybrid filaments displayed an overall increase of the average filament width compared to conventional F-actin filaments. However, the extent of LD incorporation is limited and a minimum amount of monomeric actin subunits that establish the corresponding filament contacts are required to form hybrid filaments. The presence of LD in the filaments also affected the crossover spacing of the two long-pitch helical strands: crossovers varied considerably, provided crossovers were detected at all.

The finding that the LD incorporation did not increase the mass-per-length in hybrid filaments was somewhat unexpected. A likely explanation for the absence of the mass increase can be found in the large structural heterogeneity of hybrid filaments. Clearly, more extensive data sets are required to establish the relation of incorporated LD and actin filament geometry.

1.5 Discussion

LD incorporation alters the appearance of actin filaments

Time resolved CTEM analysis of polymerizing actin has shown that filaments at early stages of polymerization appear ragged on account of numerous protrusions that jut out from the filament surface, and mature into smooth F-actin filaments over time (Millonig et al. 1988; Steinmetz et al. 1997). Following the polymerization reaction by chemical cross-linking with 1,4-PBM revealed the kinetics of LD formation to concur with the ragged filament appearance, suggesting that transient incorporation of a native LD via one of its subunits into growing F-actin filaments might be the origin of the ragged morphology. Consistent with this notion, polymerization in the presence of 1,4-PBM cross-linker and phalloidin yielded ragged filaments even at steady state and the presence of cross-linked LD in these filaments was biochemically confirmed (Steinmetz et al. 1997)(reviewed by (Schoenenberger et al. 2002)). However, the amount of incorporated LD and the effects on the filament geometry were not elucidated.

The experiments described above were designed to test whether cross-linked LD could be stably incorporated into F-actin filaments and how the incorporation affected standard filament geometry. In contrast to an earlier study, where polymerization was initiated in the presence of 1,4-PBM and phalloidin was added immediately to prevent dissociation of cross-linked moieties (Millonig et al. 1988; Steinmetz et al. 1997), we chose a slightly different approach. We copolymerized monomeric G-actin and previously cross-linked LD at defined ratios and removed unpolymerized moieties by high-speed centrifugation. This approach offers the advantage that the incorporation of the LD can be quantitatively assessed by SDS-PAGE analysis of pellet and supernatant fractions after high-speed centrifugation. Accordingly, biochemical analysis showed that the amount of LD incorporation correlated with the amount of LD present at the onset of polymerization over a certain range. This data is consistent with the notion that preformed LD can be incorporated into growing actin filaments. At the same time, the amounts of unincorporated LD in the supernatant also increased while the monomeric G-actin fraction had entirely polymerized (see Figure 7). This finding indicates that the ratio between LD and monomeric subunits in structures found in the pellet is limited and that subunit-subunit contacts as they occur in F-actin filaments are required for the overall integrity of the filament structure.

The morphological effects of LD incorporation were similarly influenced by the amounts of LD. Ultrastructural analysis by CTEM and STEM revealed that the protrusions that jut out from the filament axis in hybrid filaments become more frequent at higher LD concentrations (see Figures 8 and 10). Overall, hybrid filaments displayed a ragged morphology similar to the appearance of F-actin filaments during early stages of polymerization (Steinmetz et al. 1997; Schoenenberger et al. 2002). Our data support the earlier notion by Steinmetz and

colleagues that the transient incorporation of LD via one of its subunits is part of the early polymerization process and gives rise to a ragged morphology in growing filaments.

Interestingly, hybrid filaments resulting from copolymerization of equal amounts of G-actin and LD, exhibit segments with a ragged morphology, but also segments that show the smooth, well-ordered appearance of native F-actin filaments (see Figure 10). It is conceivable that the conventional subunit interactions of monomeric actin in these segments are essential to maintain a filamentous structure in the presence of persisting LD. Consistently, when LD is present at a large excess over G-actin in the polymerization reaction, the number of hybrid filaments is reduced. High-speed cosedimentation assays (see above) provide further support for the limited tolerance of LD incorporation. Moreover, although the irregular morphology of hybrid filaments suggests a random incorporation of LD, the constant ratios of LD and monomeric actin observed in independent high-speed cosedimentation assays suggest that the LD incorporation must be somehow regulated.

Furthermore, the orientation of the incorporated LD within the hybrid filament is not yet resolved. The incorporation via one of its subunits, leaving the second subunit freely projecting from the filament surface, represents only one possible orientation. One could also imagine alternative orientations, for example along the filament axis, which are even less compatible with the conventional filament geometry and thus significantly perturb the molecular filament architecture. Consistent with this notion, hybrid filaments were found to display local disruptions along the filament axis, irregular axial subunit arrangement, as well as deviations from the mean actin filament crossover spacing (see Figures 8, 10, 12 and 13).

LD as an initiator of filament branching

It has previously been speculated that actin has the intrinsic ability to initiate the branching of filaments even in the absence of the Arp2/3 complex (reviewed by (Schoenenberger et al. 2002), which is generally believed to mediate the formation of actin branches (for a recent review see Pollard 2007). The working hypothesis for role of the LD in the polymerization pathway suggests that during the transient incorporation of an LD, the protruding subunit that is not involved in filament contacts, might act as an initiator of filament branching. Under experimental conditions that overcome the transient nature of the LD incorporation during F-actin polymerization, the probability for branching was 25-fold higher than in normal F-actin filament preparations (Steinmetz et al. 1997). A similar observation was made for LD containing hybrid filaments. Although the incidence of branching appeared significantly higher in hybrid filaments compared to F-actin filaments, we did not quantify the number of branches mainly for two reasons: *(i)* many filament branches may have detached from their 'mother' filaments during the processing for electron microscopy, and *(ii)* the resolution of CTEM images of negatively stained hybrid filaments, even at high magnification, does not

allow for an unambiguous distinction between structurally connected, true branching sites and independent filaments that incidentally join to form a branch. In some cases, the latter difficulty could be overcome by recording STEM images at a nominal magnification of 500,000-fold, yielding a closer view of the protein interface at the branching site (Figure 13). However, the monitored area is extremely small and thus this approach is not feasible to examine the frequency of branching events.

LD incorporation leads to an increase in filament width

Image processing was used to quantitatively assess the effects of LD incorporation on the geometry of hybrid filaments. A statistically highly significant increase of the average width of approximately 10% in hybrid filaments compared to F-actin filaments corroborates the incorporation of LD into the filaments. Moreover, the width distribution showed a more pronounced variation, which reflects the irregular contour of the hybrid filaments. Because LD incorporation occasionally led to local disruptions in hybrid filaments, diameters smaller than known for F-actin filaments were also found. If only hybrid filament segments that lacked lateral protrusions were considered, the average diameter as well as the width distribution did not significantly differ from F-actin filaments. This finding supports the notion that the corresponding smooth segments in hybrid filaments are composed exclusively of monomeric actin subunits and that the increase in average width can be attributed to the incorporation of LD moieties.

To further characterize the nature of the protruding structure, we measured the maximal width, the width without the protrusion at the same site, and the width of the respective protrusion and compared the values to the average width of F-actin filaments. The diameter of the hybrid filament backbone was similar to that of smooth F-actin filaments. In addition, the vast majority of the lateral protrusions (~ 90%) had dimensions corresponding to those of actin subunits (Kabsch et al. 1985) (Fowler and Aebi 1983). Therefore, these measurements substantiated our predictions of a transient incorporation of LD via one of its subunits during early stages of actin polymerization (Table 4). Based on the dimensions alone, we cannot rule out that the LD incorporates into the filament in other orientations, for example, along the long pitch helical strand. However, LD incorporation in an orientation that conflicts the inherent polarity and symmetry of the F-actin filament would cause an even more severe impairment of the filament geometry and is therefore rather unlikely.

LD incorporation interferes with crossover spacing

Electron microscopic analysis of hybrid filaments revealed that the incorporation of cross-linked LD interferes with the global helical parameters of the F-actin filament. As a consequence, regular crossovers of the two strands were often missing or spaced further

apart in hybrid filament segments displaying lateral protrusions (Figures 10, 12 and 13). This finding provides further evidence that spontaneously formed LD can only be transiently incorporated into filaments.

Furthermore, because of the irregular spacing of manifest crossovers, which resulted from the random incorporation of cross-linked LD, meaningful mass-per-length measurements (see below) were not feasible. In contrast, filament segments without apparent LD incorporation displayed distinct crossovers and the crossover spacing was comparable to that of F-actin filaments.

The role of phalloidin in hybrid filaments

In order to prevent subunit exchange during the copolymerization of actin and cross-linked LD protomers, all polymerization reactions were carried out in the presence of phalloidin. In the absence of phalloidin, hybrid filaments were not detected in the pellet fraction of cosedimentation assays, either because they were not formed or did not abide high-speed sedimentation (data not shown). It is possible that if protomer exchange is allowed to take place, incorporated LD readily dissociates and remains present in the polymerization reaction at a concentration that is sufficiently high to prevent efficient polymerization. Alternatively, phalloidin stabilization of the monomeric protomers is required to provide a basic filamentous framework that will tolerate the presence of LD despite its interference with the filament geometry.

Although phalloidin stabilization is crucial for the integrity of hybrid filaments, it is doubtful whether phalloidin is bound in hybrid filament segments where the morphology indicates LD incorporation. A number of studies have addressed the localization of phalloidin binding sites in filamentous actin (Vandekerckhove et al. 1985; Barden et al. 1987; Miki et al. 1987; Drubin et al. 1993; Faulstich et al. 1993; Lorenz et al. 1993; Heidecker et al. 1995; Steinmetz et al. 1998; Belmont et al. 1999; Blondin et al. 2001; Shvetsov et al. 2002; Orlova et al. 2004; Oda et al. 2005), but nothing is known about the interactions of phalloidin with LD or LD-containing segments of hybrid filaments. It is generally agreed that for the formation of a tight complex with actin, phalloidin requires an actin nucleus containing at least three hydrolyzed ADP-P_i/ADP-actin subunits in a conformation that is distinct from G-actin (Barden et al. 1987; Orlova et al. 1995; Oda et al. 2005). In addition, studies by Faulstich and colleagues suggested that the phalloidin-binding site in the F-actin filament involves regions near the actin C-terminus (Faulstich et al. 1993). In the LD, this region is involved in forming the antiparallel interface between the two subunits. Therefore, and because the contacts to neighboring subunits are also distinct from those in F-actin filaments, it seems unlikely that phalloidin can bind at sites of LD incorporation. Consistent with this notion, actin filament morphology was altered by the copolymerization of actin that was derivatized at the C-terminal Cys374 with tetramethylrhodamine and unmodified G-actin

(Kudryashov et al. 2004). Employing an undecagold-tagged phalloidin, which has been shown to stoichiometrically decorate F-actin filaments and can be visualized by STEM (Steinmetz et al. 1998), in an experimental setup where incorporated native LD is preserved by 1,4-PBM cross-linking throughout polymerization, would provide further insight whether LD-incorporation is compatible with phalloidin binding in hybrid filaments.

Hybrid filaments do not lend themselves to mass-per-length analysis

Analytical dark-field scanning transmission microscope (STEM) has become a versatile tool for measuring the masses of large biological macromolecules independent of their shape (reviewed in Engel and Colliex 1993). Because in many cases it has been instrumental in determining the subunit stoichiometry of oligomeric protein complexes such as e.g. the aquaporins maltoporin (Lepault et al. 1988) and aerolysin (Wilmsen et al., 1992), we reasoned that STEM measurements should provide quantitative information on the amount of LD that can be copolymerized with actin into hybrid filaments. Our initial assumption that the incorporation of dimeric LD protomers would lead to an increase of the mass-per-length (MPL) was not confirmed (see Table 2). Rather, the average MPLs and Gaussian peaks for hybrid filaments did not significantly differ from those of conventional F-actin filaments (Figure 9), which were in good agreement with previously reported values (Steinmetz et al. 1998). Several factors, or maybe a combination thereof, should be considered that might explain the absence of a significant MPL increase. First, the maximal number of LD protomers which are tolerated in the hybrid filament might not be sufficient to yield a detectable difference, as the increase in mass with respect to the MPL measured in F-actin filaments needs to be at least ~ 3 kDa/nm (S. Müller, personal communication). Furthermore, the low-contrast dark-field STEM images did not allow reliable boxing of hybrid filament segments with a high frequency of lateral protrusions (Figure 14). As a consequence, hybrid filament segments without apparent LD incorporation were included in the MPL measurements. Because the incidence of LD incorporation was also highly irregular (see above), the proportion of measurements representing LD-containing filament segments is probably rather low.

In addition, as discussed above, LD incorporation interferes with formation of regular crossover repeats and most likely with the filament twist. Thus, it is conceivable that the number of actin subunits per crossover, which is 13 for F-actin filaments (Steinmetz et al. 1997), is altered and results in a reduced MPL value. Overall, the randomized LD incorporation and its structural consequences are incompatible with significant MPL measurements.

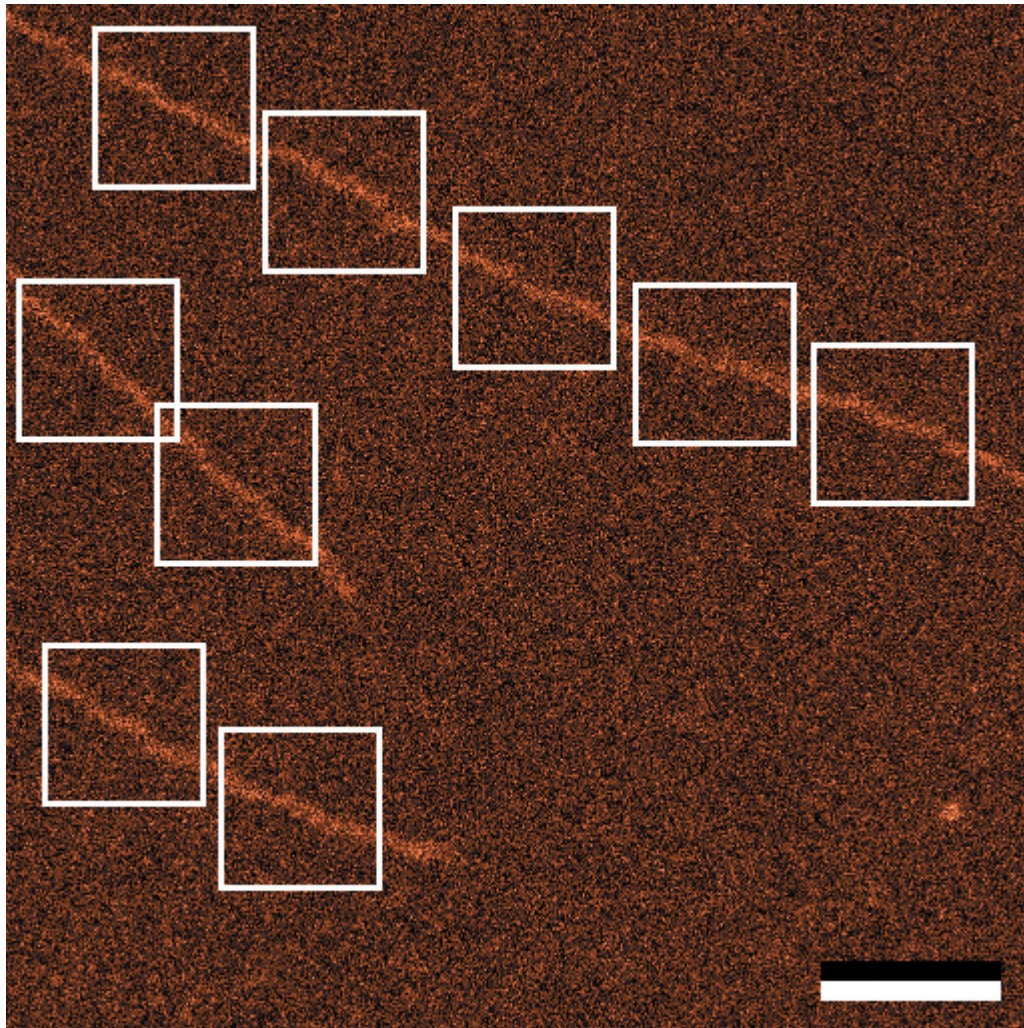


Figure 14. STEM dark-field image for MPL analysis. Lateral protrusions cannot be discerned in unstained hybrid filaments. Boxed areas measuring 80 x 80 pixel were used for MPL analysis. Bar, 100 nm.

The role of antiparallel dimers in actin patterning

Since the first atomic structure of monomeric actin complexed to DNase I has been reported in 1990 (Kabsch et al. 1990), a number of crystal structures have been obtained that represent mostly complexed or chemically modified actin (e.g. (Hesterkamp et al. 1993; Bubb et al. 1995; Reutzel et al. 2004; Klenchin et al. 2006; Lassing et al. 2007). The similarity of the complexed actin structures demonstrates that the overall structure of monomeric actin is not significantly affected by a multitude of actin-binding proteins and toxins. The first crystals induced from pure actin by gadolinium were described in the 1980s (Aebi et al. 1980; Aebi et al. 1981; Smith et al. 1983).

Besides other actin contacts, these 2-D actin crystals called 'sheets' and 'tubes' include a unit cell structure and symmetry similar to that of the LD (Millonig et al. 1988), which renders them suitable structures to examine structural aspects of the LD.

Possibly because of its transient nature and its geometry, which seems to be incompatible with that of the helical F-actin filament, the structural information available on antiparallel actin dimers is very limited and thus, the significance of LD-mediated processes is poorly understood. The crystallographic structure of a dimeric polylysine-actin-latrunculin A complex at 3.5-Å resolution with characteristics similar to the LD has been reported a few years ago (Bubb et al. 2002). An antiparallel actin dimer was also observed in the asymmetric unit of ECP-actin crystals (Klenchin 2006). The increasing number of crystal structures with actin contacts other than those that exist in mature F-actin filaments support the notion that unconventional forms of actin play a role in actin patterning (Klenchin et al. 2006; Lassing et al. 2007). Considering the structural plasticity inherent to different forms of actin, one could imagine that different intermediates dynamically transform from one form to another with ongoing polymerization and are eventually funneled into a pathway that yields mature F-actin filaments *in vitro* (Galkin et al. 2002; Orlova et al. 2004). This dynamic behavior provides a plausible explanation for the seemingly paradox contribution of an antiparallel dimer in the F-actin filament symmetry (Bubb et al. 2002; Pederson and Aebi 2002; Reutzler et al. 2004) and reconciles different structural intermediates with the Holmes model of the actin filament (Holmes et al. 1990; Lorenz et al. 1993).

In cells, it has been speculated that the flexibility of incorporated antiparallel dimers facilitates the binding of the Arp2/3 complex (Lassing et al. 2007), which leads to branched actin structures at angles ranging from 35° to 90° as seen by cryoelectron tomography studies (Medalia et al. 2002). As the indications for a role of the LD in actin patterning are accumulating, the need for tools that are suitable to specifically study this form of actin both *in vitro* and *in vivo* becomes evident. Therefore, we are aiming at raising antibodies that recognize distinct forms of actin by using peptide nanoparticles as a platform for immunization (Raman et al. 2006; Raman 2007)(Schroeder et al., JMB, manuscript accepted). An antibody that recognizes the LD and not other forms of actin would undoubtedly be of great value in dissecting its role in actin assembly and supramolecular patterning.

1.6 Conclusions and outlook

The LD, an antiparallel dimeric actin species that transiently occurs at the onset of actin polymerization, is by itself polymerization incompetent and incompatible with the helical geometry of mature F-actin filaments. However, copolymerization of 1,4-PBM cross-linked LD with monomeric Ca-ATP-G-actin at defined ratios produced hybrid filaments with stably incorporated LD. Ultrastructural analysis by electron microscopy revealed that LD incorporation significantly interferes with the morphology of synthetic F-actin filaments. Although there is an upper limit for the incorporation of LD, the degree of structural disorder in hybrid filaments correlates with the amount of LD present.

At closer inspection, filament segments comparable to F-actin filaments and segments with morphological and geometrical disorders could be discerned. Lateral protrusions in the latter led to an increase in width on the scale of an actin subunit. This is consistent with the notion that the protrusions represent free LD subunits that are jutting out from the filaments, as it has been predicted for the unconventional 'LD-pathway' in the course of actin polymerization. Moreover, lateral protrusions and the increased occurrence of branches in negatively stained hybrid filament specimens provides further evidence for an essential role of the LD in filament branching. Because the branches in hybrid filament preparations occur in the absence of the Arp2/3 complex or any other ligand, one might argue that the Arp2/3 complex acts through stabilizing a branch-inducing actin arrangement rather than initiating the actin branching.

Prominent local disorders of the filament geometry confirm that actin filaments represent a highly flexible structure including variable subunit contacts. The question whether phalloidin binds at sites of LD incorporation is still open, although one might assume that the subunit interactions required for phalloidin binding are not established and thus, dissociation of disordered filament segments is likely to occur. Labeling of hybrid filaments with undecagold-tagged phalloidin and subsequent dark field STEM analysis might shed some light on this issue. Alternatively, dissociation of hybrid filaments could be minimized by stabilizing hybrid filaments with a mild fixative, provided it does not affect their morphology.

Last but not least, hybrid filaments represent supramolecular actin assemblies that comprise the otherwise transient LD. Thus, they can be used to test the specificity of antibodies raised against distinct forms of actin, such as the LD. Other supramolecular actin structures that similarly display actin subunits in an antiparallel orientation, for example gadolinium-induced 2-D crystalline actin sheets and paracrystalline actin bundles, are less suitable, either because they are considerably more sensitive to mechanical stress and readily fall apart or the antiparallel subunit arrangement is less accessible.

In summary, the hybrid filaments hold large potential not only for studying the role of the LD in actin patterning, but also for analysis of LD-specific antibody reagents.

Chapter 2

Peptide Nanoparticles

**A potent immunogen for the production
of monospecific antibodies**

2.1 Introduction

2.1.1 Bionanoparticles

During the last years, the research on nanosized particles (size $\leq 100\text{nm}$) has intensified considerably, mainly because numerous promising applications have emerged.

Of particular interest are biology-inspired, protein-based nanoparticles which hold potential for biological, pharmaceutical and medical applications such as gene delivery, drug targeting, antigen display and vaccination (Allen and Cullis 2004; Kiser et al. 1998; Langer 1998; Savic et al. 2003). In this context, globular nanoparticles are frequently used as carriers of active ingredients that, in the ideal case, can be directly piloted to a specific location or even to a distinct cellular domain. Another advantage of globular nanoparticles over larger or differently shaped carriers is their comparatively high surface to volume ratio, which facilitates the transportation of high concentrations of ingredients.

Several bionanoparticles are based on self-organizing building blocks that are known from nature. For instance, multiple ferritin molecules (Ensign et al. 2004; Kramer et al. 2004) or heat shock protein subunits (Flenniken et al. 2005; Flenniken et al. 2006) can build up well-defined protein cages. Moreover, specific polypeptide chains are capable to self-assemble into precisely defined symmetric virus capsids or virus-like particles (VLP) (Georgens et al. 2005; May et al. 2002). Virus capsids and VLP hold the particular advantages that they are uniform in size, applicable in a robust, well-defined manner (Crick and Watson 1956; Johnson and Chiu 2000; Liljas 1999) and highly amenable to genetic and chemical modifications (Lee and Wang 2006).

Some decades ago it was already suggested that VLP could serve as a suitable platform to repetitively display copies of a specific antigen, which might improve the effectiveness of vaccines (Aebi et al. 1977; Buhle and Aebi 1984; Kistler et al. 1978). Consistent with this notion, immunization experiments with VLP yielded a strong immune response and high titers of specific antibodies (Bachmann and Zinkernagel 1996; Baschong et al. 2003; Zinkernagel 1996).

In the following Chapter 2.1.2, a novel class of self-assembling peptide nanoparticles, which were originally designed by Burkhard and colleagues in the late 1990s (Raman et al. 2006), will be described in more detail. In particular, we tested the suitability of specific nanoparticles to provide a platform for repetitive antigen display. For this purpose, the nanoparticles were genetically modified to express actin epitopes on their surface. Most animals with 'loaded' nanoparticles developed a significant immune response against otherwise poor antigens and both, polyclonal and monoclonal antibody reagents could be established.

2.1.2 Self-assembling peptide nanoparticles

The basic, unmodified peptide nanoparticle has been computationally designed to self-assemble from 60 single polypeptide chains into highly organized spherical particles of a size with regular polyhedral symmetry (Raman et al. 2006). The basic assembly steps of the core polypeptide and a model of the resulting nanoparticle are presented in Figure 15.

The core polypeptide chain is composed of two very stable coiled coil oligomerization domains (Burkhard et al. 2002; Guo et al. 2000) with different oligomerization states, which are joined by a short linker segment (Figure 15 A). The N-terminal oligomerization domain (green) corresponds to a slightly modified pentameric coiled coil domain of the cartilage oligomeric matrix protein (COMP) (Malashkevich et al. 1996) and the C-terminal domain (blue) comprises a *de novo* designed minimal trimeric coiled coil sequence (Burkhard et al. 2002; Burkhard et al. 2000a; Burkhard et al. 2000b). A rigid α -helical linker made up of two glycine residues connects the two oligomerization domains (Figure 15 B).

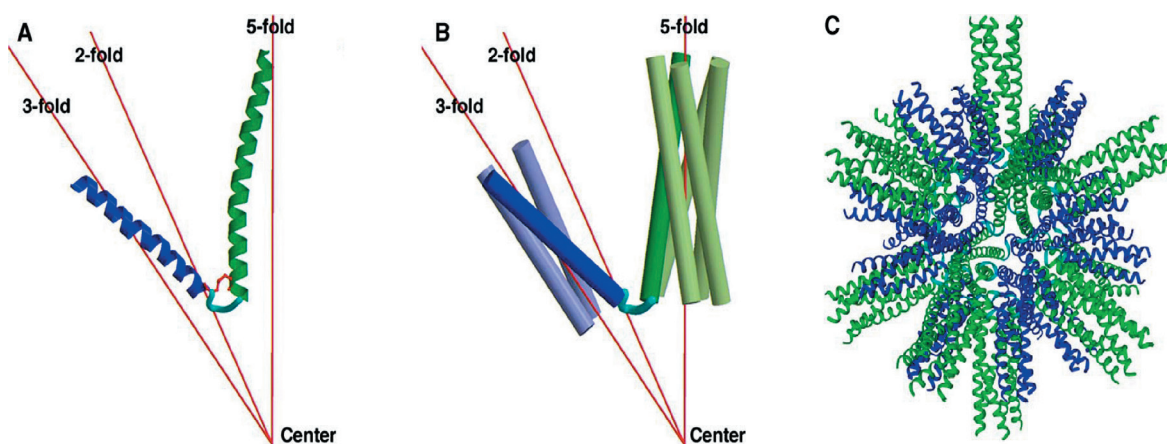


Figure 15. General architecture of peptide nanoparticles. In (A), the peptide building block, which is composed of a pentameric coiled coil domain of COMP with five-fold symmetry (green), a linker segment (cyan) and a *de novo* designed coiled coil domain with three-fold symmetry (blue), is displayed such that the internal symmetry elements of the two domains are superimposed onto the symmetry axes of the nanoparticle. The intrahelical disulfide bridge between the helices is displayed in red. In (B), the complete coiled coil domains are displayed as cylinders. Additional symmetry objects generated by the five-fold and the three-fold rotational symmetry elements are displayed in lighter shades of green and blue, whereas the original molecule is displayed in dark green and blue. The rotational symmetry axes are displayed as red lines in (A) and (B). (C) Computer model of the assembled peptide nanoparticle. This figure has been adapted from Raman et al. 2006.

Moreover, inter- and intrahelical salt bridges and hydrophobic interactions stabilize the coiled coils. At the 3' end of the pentameric and 5' end of the trimeric oligomerization domain, two cysteine residues were introduced to allow intramolecular disulphide bonding.

Hence, under oxidizing conditions the spatial orientation of the two helical oligomers within a polypeptide chain is assured without disorganizing their geometry (Raman 2007). To facilitate the downstream purification process, a His-tag was inserted at the N-terminus of the polypeptide chain.

To examine the immunogenic potential of self-assembling peptide nanoparticles, we grafted different actin-related antigenic determinants onto the C-terminus of the core polypeptide by genetic engineering. Therefore, nanoparticles can be considered a repetitive antigen display system conducive to raising a strong immune response.

2.2 Aims of project

The specific aims of the study presented below are i) to characterize recombinant NPs that carry an actin epitope, and ii) to demonstrate their immunogenic potential by establishing antibodies that react with different forms of actin.

2.3 Material and methods

Most of the methods applied are presented in the publication in Chapter 2.4.3.

Direct immunoelectron microscopy on peptide nanoparticles

Before use, aggregates were removed from nanoparticle preparations by centrifugation at 16.000 g for 15 min. Nanoparticles were applied to gently glow-discharged copper grids and excess liquid was blotted with filter paper. Then the grids were placed upside-down onto a droplet of 5 nm gold-coupled actin loop antibody 5B4 (5B4-Au) or a 5 nm gold-coupled unrelated antibody, washed with aqua bidest. and subsequently negatively stained with uranyl acetate. Serial dilutions were tested for each antibody.

After careful washing, the specimens were processed for electron microscopy as described in Chapter 1.3.

2.4 Results 1

2.4.1 Production of recombinant nanoparticles

The *de novo* designed polypeptides, which serve as building blocks for peptide nanoparticles (see Chapter 2.1.2), were recombinantly expressed in *E. coli* and then purified under denaturing conditions via metal affinity chromatography. Refolding was carried out by a stepwise dilution of urea under reducing conditions to prevent the formation of intermolecular disulfide bridges and thus promote the self-assembly of spherical nanoparticles. In a final dialysis step, oxidizing conditions allowed the formation of the disulfide bridges.

Consistent with the computer model shown in Figure 15 C, CTEM of negatively stained specimens revealed that the refolded core polypeptides self-assemble into spherical particles (Figure 16). The predominant species of particles exhibits a diameter of ~ 30 nm, warranting the term ‘nanoparticle’.

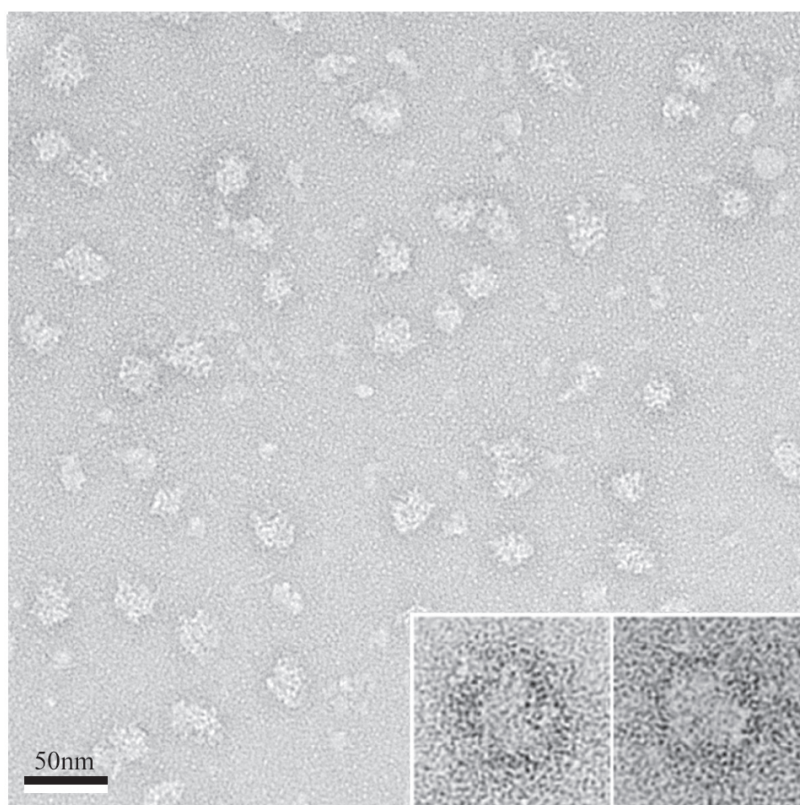


Figure 16. CTEM micrograph of negatively stained, ‘bare’ peptide nanoparticles. Core polypeptides self-assemble into spheric nanoparticles with a diameter of ~ 30 nm. Bar, 50 nm; frame size of inset: 68 nm.

Because the nanoparticles presented in Figure 16 have been assembled from unmodified core polypeptides, they are considered 'bare' (NP). Core polypeptides that were genetically functionalized with actin-related epitopes, were expressed, purified and refolded accordingly (see below).

2.4.2 Peptide nanoparticles are potent immunogens

2.4.2.1 Characterization of the actin point mutation G245D

In order to elucidate whether functionalization renders nanoparticles into potent immunogens, we genetically engineered an epitope which corresponds to amino acid residues 239 - 251 of human β -cytoplasmic actin with an additional mutation of Gly245 to Asp245, onto the core polypeptide.

A highly tumorigenic cell strain that expresses this single point mutated β -actin was established by neoplastic transformation of diploid KD fibroblasts *in vitro* (Leavitt and Kakunaga 1980). It has been shown that the expression of G245D variant β -actin in fibroblast cell lines caused their tumorigenic transformation (Vandekerckhove et al. 1980). For example, stable transfection of Rat-2 fibroblasts produced a tumorigenic strain termed Rat-2 sm9 (Leavitt unpublished).

The SDS-PAGE of total cell extracts in Figure 17 A revealed that Rat-2 sm9 expresses a ~ 42 kDa protein with a slightly reduced electrophoretic mobility compared to endogenous β -actin.

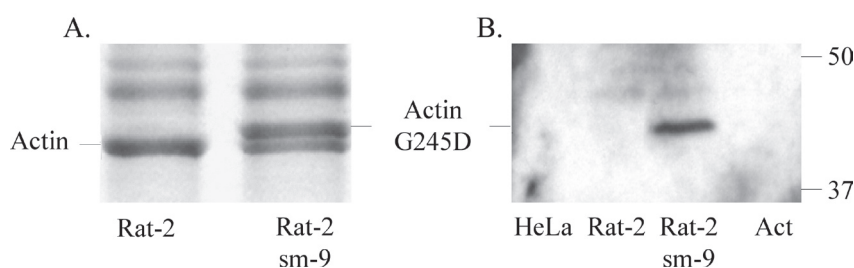


Figure 17. G245D mutant β -cytoplasmic actin. (A) Whole cell extracts prepared from Rat-2 fibroblasts and Rat-2 sm9 cells were subjected to SDS-PAGE and stained with Coomassie brilliant blue. In Rat-2, the band corresponding to wild type endogenous actin is more pronounced than in Rat-2 sm9 where an additional band with a slightly reduced mobility is seen. (B) Immunoblotting with a polyclonal antibody that specifically binds to the G245D variant actin. The mutant actin is only present in the transfected cells and not in untransfected Rat-2 or HeLa cells. The serum is specific for G245D actin variant and does not react with purified rabbit skeletal muscle actin (Act). The molecular masses in kDa of two standard proteins are indicated on the right.

The staining intensity of the mutant actin was comparable to that of the endogenous actin. Compared to the levels of β -actin in untransfected Rat-2, endogenous actin appeared to be slightly reduced in Rat-2 sm9. This finding suggests that expression of the variant actin led to a down regulation of the endogenous actin.

To confirm that this band represents the G245D variant of actin, we performed immunoblotting assays with whole cell extracts from both transfected and untransfected cell lines using a polyclonal antiserum that specifically recognizes only the G245D mutant (Leavitt et al. 1987). As documented in Figure 17 B, immunoblot analysis revealed that the G245D-specific serum detects a single band in Rat-2 sm9 cells that is absent in untransfected Rat-2 and HeLa cells. Similarly, the antibody did not react with purified skeletal muscle actin. Reprobing the membrane with an antibody that reacts to all actin isoforms confirmed that similar amounts of actin were present in Rat-2 and HeLa cell extracts and that the endogenous actin migrates slightly faster than the G245D variant (data not shown).

2.4.2.2 Polypeptides containing actin-related sequences self-assemble into nanoparticles

Because the synthetic 13-mer peptide containing the G245D mutation had proven to be highly immunogenic in standard immunization procedures and had produced a highly specific antiserum, we reasoned that this epitope would be suitable to test the immunogenic potential of 'loaded' nanoparticles. For this purpose, we genetically grafted the sequence corresponding to the amino acid residues 239 - 251 of human β -cytoplasmic actin with either a glycine or an aspartate residue at position 245 onto the C-terminus of the nanoparticle core peptide. Recombinant expression, purification and refolding were carried out as described in Chapter 2.3.

To confirm that the epitopes did not interfere with particle assembly, we examined the preparations after refolding by CTEM. Electron micrographs in Figure 18 illustrate that both, polypeptides expressing either wild type or the mutant actin epitope at the C-terminus, were able to self-assemble into nanoparticles. The 'loaded' nanoparticles displayed a similar morphology, measuring ~ 30 nm in diameter. Nanoparticles containing the β -cytoplasmic actin wild type epitope were termed NP-Gly (Figure 18 A), according to the glycine residue in position 245, whereas nanoparticles containing the mutated actin epitope were termed NP-Asp (Figure 18 B), indicating the exchange to an aspartic acid residue.

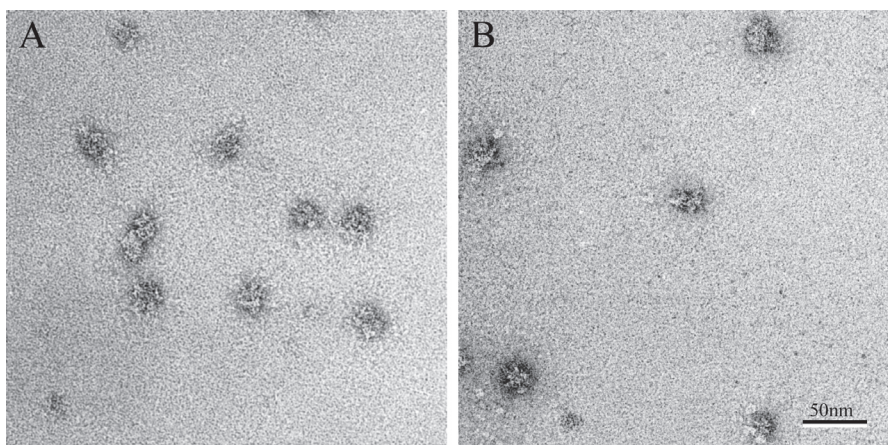


Figure 18. Peptide nanoparticles expressing actin-related epitopes. Epitopes corresponding to amino acids 239 - 251 residues of human β -cytoplasmic actin were engineered to the C-terminus of the core polypeptide chains that serve as building blocks for peptide nanoparticles. Following self-assembly, samples were applied to gently glow-discharged cooper grids and negatively stained with 2% uranyl acetate. (A), NP-Gly expressing a C-terminal sequence corresponding to human wild type β -cytoplasmic actin (SYELPDG₂₄₅QVITUG). (B), NP-Asp expressing the corresponding actin sequence but with a G245D mutation (SYELPDD₂₄₅QVITUG) in actin.

2.4.2.3 Demonstration of actin-related peptides on peptide nanoparticles

Even at closer inspection, CTEM did not reveal morphological differences between core nanoparticles lacking an epitope (NP), NP-Gly and NP-Asp (see Chapter 2.4.2.2). Hence, it remained unclear if multiple copies of the actin-related epitopes were exposed on the surface of NP-Gly and NP-Asp, as was predicted by modeling. To address this question, we performed biochemical experiments using the previously established G245D-specific polyclonal antiserum termed HuT-14.

Because the N-terminus of the core polypeptide contains a histidine tag, NP-Gly, NP-Asp and NP were separated by SDS-PAGE, blotted and probed with a monoclonal His antibody. As expected, the immunoblot in Figure 19 A shows that under denaturing conditions the His antibody detected the polypeptide chains in 'bare' (NP) and 'loaded' (NP-Gly, NP-Asp) nanoparticles tested. Consistent with the presence of an extra epitope, the monomeric species from NP-Gly and NP-Asp moved comparatively slower on SDS-PAGE than the monomeric NP core polypeptide.

Subsequently, we tested if the specific HuT-14 polyclonal antibody could recognize the epitopes under native conditions. For immunoprecipitation (IP), the polyclonal antiserum HuT-14 (characterized in Chapter 2.4.2.3) was covalently bound to Protein A Sepharose beads (PA) and then the PA-HuT-14 slurry was incubated with assembled NP-Gly, NP-Asp

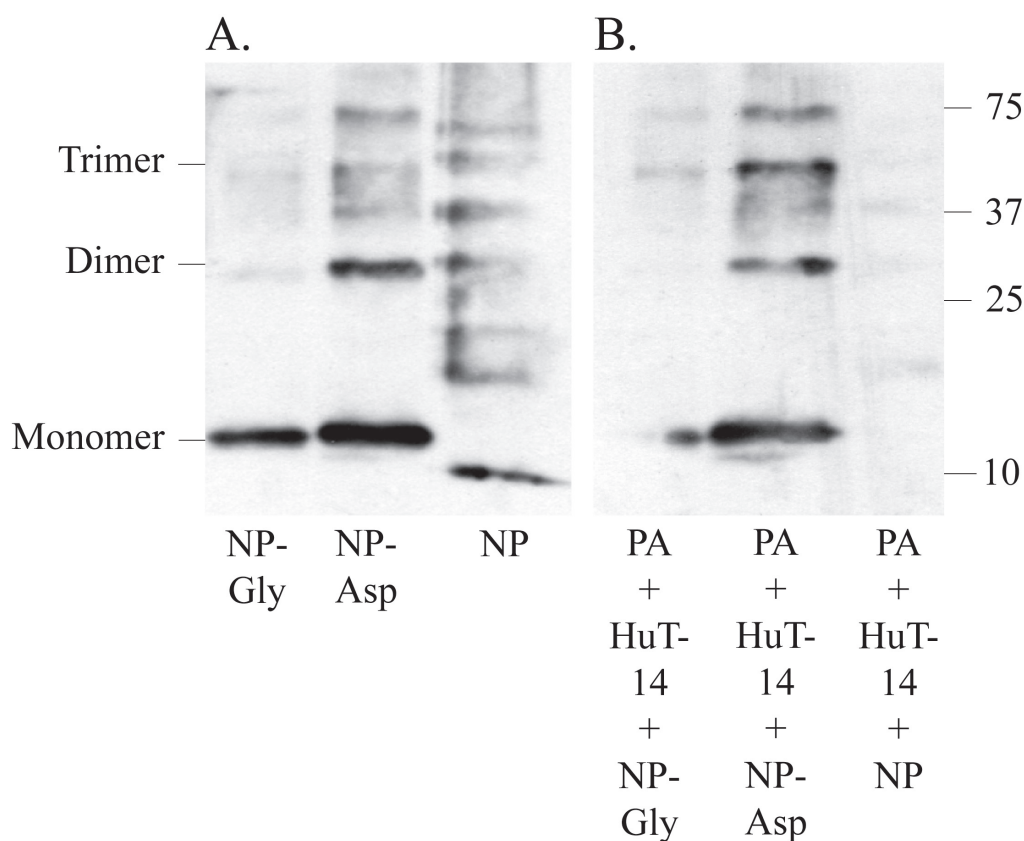


Figure 19. Actin-related epitopes on exposed peptidic nanoparticles. (A), Immunoblot analysis of NP-Gly, NP-Asp and NP with an His-tag antibody. The additional actin-related sequence in NP-Gly and NP-Asp lead to a reduced electrophoretic mobility of the corresponding polypeptide under denaturing conditions. (B), Immunoblot analysis of immunoprecipitated nanoparticles. HuT-14-antiserum was covalently bound to Protein A Sepharose (PA) and then the slurry was incubated with NP, NP-Gly and NP-Asp. Immunoprecipitated complexes were separated on SDS-PAGE and blotted. Probing with an His antibody showed that only NP-Asp were immunoprecipitated by HuT-14. NP-Gly, nanoparticles expressing an epitope derived from human β -cytoplasmic actin; NP-Asp, nanoparticles expressing a G245D mutant actin epitope; NP, core nanoparticles without epitope. The molecular masses of standard proteins in kDa are indicated on the right.

and NP. Subsequently, the immunoprecipitated complexes were collected by centrifugation and carefully washed. After releasing complexes from the beads by heat denaturing in SDS sample buffer, the IP samples were analyzed by SDS-PAGE and immunoblotted with a His antibody (see Chapter 2.3).

As documented in Figure 19 B, HuT-14 precipitated exclusively NP-Asp, which contains the mutated actin epitope. Bands that represent the monomeric, dimeric and higher oligomeric forms of the NP-Asp polypeptide were detected by the His monoclonal antibody. However, both NP-Gly as well as NP were not effectively immunoprecipitated by the G245D-specific HuT-14 and appeared to be largely absent.

In addition, we carried out immunoprecipitation experiments with a polyclonal antiserum that was raised against the human wild type β -cytoplasmic actin ('Gly') peptide. This antiserum immunoprecipitated predominantly NP-Gly and to a significant lesser extent NP-Asp. However, NPs lacking an actin-epitope were not detected (data not shown).

In summary, the data presented show that recombinant polypeptide chains expressing specific actin-related epitopes at the C-terminus self-assemble into homogenous populations of peptide nanoparticles. Although the monomeric polypeptides exhibited a slightly different electrophoretic mobility depending on the epitope sequence, the assembled particles could not be distinguished by CTEM. Immunoprecipitation studies with an antibody that specifically recognizes the G245D point mutation suggested that the antibody has access to the mutated actin epitope in assembled NP-Asp under native conditions, and thus, the epitopes are likely to be exposed on the nanoparticle surface.

2.4.2.4 Immunization with 'loaded' nanoparticles yields specific polyclonal antiserum

The apparent surface-exposure of the grafted actin-epitope and their repetitive, ordered arrangement implied from the polypeptide design, suggested that nanoparticles might be a suitable repetitive antigen display system that is able to induce a strong immune response in a host organism. To test this hypothesis, NP-Asp and NP-Gly were used to immunize rabbits for the production of polyclonal, monospecific antibodies. The antisera that were purified from different bleedings were tested for reactivity by immunoblot experiments. The highly specific Hut-14, which had been raised previously against a synthetic peptide containing the G245D mutation, served as positive control to confirm that signals correspond to mutant actin (data not shown).

As illustrated in Figure 20, crude serum from the final bleed after a standard immunization with NP-Asp reacted at a 1:10.000 dilution very strongly with a single band in Rat-2 sm9 whole cell extracts. The 'Asp'-antiserum did not react with endogenous β -cytoplasmic actin in whole cell extracts of Rat-2, Rat-2 sm9 or with purified α -skeletal muscle actin.

Immunization of rabbits with NP-Gly produced a 'Gly'-antiserum, which reacted with wild type and with mutant actin, albeit with a significantly reduced affinity (data not shown).

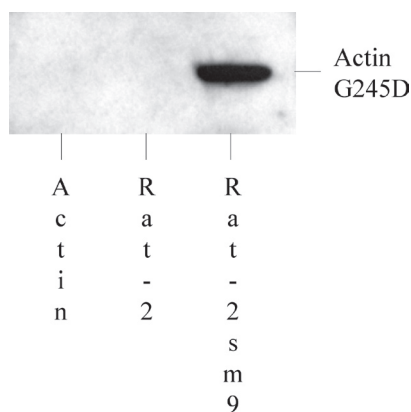


Figure 20. Specificity of the polyclonal antiserum raised against NP-Asp. Purified skeletal muscle actin and whole cell extracts of Rat-2 and Rat-2 sm9 cells were analyzed by immunoblotting with a 1:10,000 dilution of the antiserum produced in rabbits immunized with NP-Asp. The antiserum specifically detects the G245D actin variant expressed in Rat-2 sm9 and showed no reactivity with β -cytoplasmic actin in Rat-2 cells, or with skeletal muscle actin.

In conclusion, the data indicate that epitope-presenting nanoparticles are potent immunogens that elicit a strong immune response. In the following we grafted a sequence corresponding to a structural feature that is conserved in all actins, onto the C-terminus of nanoparticles and used them for the production of monoclonal antibodies.

Chapter 2.5

Peptide nanoparticles serve as a powerful platform for the immunogenic display of poorly antigenic actin determinants

Ulrich Schroeder¹, Alexandra Graff¹, Sabine Buchmeier², Per Rigler³, Unai Silvan¹, David Tropel¹, Brigitte M. Jockusch², Ueli Aebi¹, Peter Burkhard⁴ and Cora-Ann Schoenenberger¹

¹M.E. Müller Institute for Structural Biology, Biozentrum, University of Basel, Switzerland,

²Cell Biology, Zoological Institute, Technical University of Braunschweig, Germany

³Department of Chemistry, University of Basel, Switzerland

⁴The Institute of Materials Science, University of Connecticut, USA

Running title: Repetitive display of actin epitopes

Key words: actin conformations, actin antibodies, nanoparticles, antigenic display, fluorescence correlation spectroscopy, hydrophobic loop

Corresponding author:

Cora-Ann Schoenenberger
M.E. Müller Institute for Structural Biology
Biozentrum, University of Basel
Klingelbergstrasse 70
CH-4056 Basel/Switzerland

T: 0041 61 2672096

F: 0041 61 2672109

Cora-ann.schoenenberger@unibas.ch

Summary

The role of actin in transcription and RNA processing is now widely accepted but the form of nuclear actin remains enigmatic. Monomeric, oligomeric or polymeric forms of actin seem to be involved in nuclear functions. Moreover, uncommon forms of actin like the ‘lower dimer’ have been observed *in vitro*. Antibodies have been pivotal in revealing the presence and distribution of different forms of actin in different cellular locations. Because of its high degree of conservation, actin is a poor immunogen and only few specific actin antibodies are available. To unravel the mystery of less common forms of actin, in particular those in the nucleus, we chose to tailor monoclonal antibodies (mAb) to recognize distinct forms of actin. To increase the immune response, we used a new approach based on peptide nanoparticles, which are designed to mimic an icosahedral virus capsid and allow the repetitive, ordered display of a specific epitope on their surface. Actin sequences representing the highly conserved ‘hydrophobic loop’, which is buried in the F-actin filament, were grafted onto the surface of nanoparticles by genetic engineering. After immunization with ‘loop nanoparticles’, a number of mAbs were established that bind to the hydrophobic loop both *in vitro* and *in situ*. Immunofluorescence studies on cells revealed that F-actin filaments were only labeled once the epitope had been exposed. Our studies indicate that self-assembling peptide nanoparticles represent a versatile platform that can easily be customized to present antigenic determinants in repetitive, ordered arrays and elicit an immune response against poor antigens.

Introduction

Remodeling of the actin cytoskeleton plays an important role in many physio-pathological processes including embryonic development, tissue repair and carcinogenesis. The dynamics of the temporally and spatially tightly controlled actin network depends on the interplay of monomeric actin associated with distinct actin binding proteins (ABPs) and filamentous actin (F-actin) organized into higher order structures. Conventional F-actin filaments have not yet been identified in living, untreated nuclei, indicating that for its nuclear functions, actin might assume distinct oligo- or polymeric forms (Jockusch et al. 2006). Support for such “unconventional” actin assemblies has been gained from studies with antibodies that recognize distinct states of actin. For example, Gonsior and colleagues describe a monoclonal antibody, 2G2, which was raised against an actin-profilin complex, that recognizes a distinct form of actin in the nucleus (Gonsior et al. 1999). Another monoclonal antibody that reveals distinct actin structures in the nucleus and the cytoplasm, was established by immunizing mice with a chemically cross-linked, antiparallel actin dimer (Schoenenberger et al. 2005). Compared to phalloidin, which only binds to actin subunits in an F-actin conformation, antibodies are clearly more versatile tools in that they recognize different states and suprastructures of actin.

As actin is a highly conserved protein throughout all eukaryotic phyla, it is rather difficult to obtain specific anti-actins with affinities sufficient for use in immunoprecipitation, immunoblotting or immunocytochemical analyses. Early studies used actin purified from vertebrate skeletal or smooth muscle to immunize rabbits for the production of antisera. Although the immunogen differed only in a few amino acids from the endogenous actins of the vaccinated animal, specific antibodies were obtained in some cases (Lazarides and Weber 1974; Jockusch et al. 1978). These antibodies proved very useful in demonstrating the presence and localization of actin filaments in cultivated mammalian cells as they crossreacted with muscle as well as with nonmuscle actins from different species. In addition, they stimulated a plethora of studies on cellular architecture and mobility (Lazarides and Weber 1974). Subsequently, peptides corresponding to the N-terminal region, which has a slightly higher variability than the rest of the molecule (Vandekerckhove and Weber 1979), were successfully used to generate selected, isoform-specific monoclonal antibodies (Skalli et al. 1986; Gimona et al. 1994). However, even when technical developments designed to improve the immune response, such as specific immunization protocols, macrophage-activating carriers and adjuvants or specific myeloma strains for the production of monoclonal antibodies, are implemented, the production of a reliable anti-actin with high specificity for different forms of actin remains a challenging enterprise.

Modern immunization strategies involve live attenuated, whole inactivated, recombinant subunit protein, live vector DNA, and combinatorial vaccines (for reviews see (Cho 2003; Zinkernagel 2003)). Compared to attenuated or whole inactivated vaccines, which are not devoid of risk factors, subunit vaccines based on recombinant proteins can be considered safe. They may suffer from poor immunogenicity owing to incorrect folding of the target protein or its poor presentation to the immune system. One class of subunit vaccines that are readily recognized by the immune system are Virus-like particles (VLPs), highly organized spheres that self-assemble from structural envelope proteins of virus particles (for reviews see (Ludwig and Wagner 2007; Roy and Noad 2008)). When derived from the original pathogen, the repetitively arranged epitopes of the VLPs mimic viral antigens in a highly authentic conformation. In addition, VLPs have been used as carrier and presentation system for the repetitive display of B-cell epitopes from foreign pathogens.

The concept of improving antigenicity through presenting an antigen in an ordered, repetitive array (Baschong et al. 2003) is being increasingly employed to obtain high titers of specific antibodies. A case for this concept was made more than 25 years ago, when trying to produce high-titer/high-affinity monospecific antibodies against the different capsid proteins of bacteriophage T4 (Aebi et al. 1977). Subsequently, targeted expression of antigenic determinants on the surface of virus capsids or bacterial envelopes was achieved by recombinant DNA technology (Sanchez and Holmgren 1989; Greenwood et al. 1991; Lomonosoff and Johnson 1996; Porta et al. 1996; Lee et al. 2003). Alternatively, antigens were grafted onto *in vitro* assembled repetitive arrays of proteins (Domingo et al. 2001) or

stoichiometrically bound to the surface of a virus capsid in the form of antigen-carrying proteins (Ren et al. 1996). Engineering antigens as repetitive supramolecular arrays is now leading the way to novel strategies for therapeutic vaccines for chronic diseases (Bachmann and Dyer 2004).

So far, viral capsid structures have mostly been used as repetitive antigen display systems. Here we report the application of nanoparticles (Raman et al. 2006), which are formed through self-assembly of a single designed polypeptide, as a novel platform for the repetitive display of poorly immunogenic actin epitopes. The design principle of the peptide nanoparticles suggests immunization properties similar to those of VLPs. However, compared to VLPs the nanoparticle polypeptide can be easily customized at the N- and C- terminus by genetic engineering and recombinantly expressed in *E. coli*. To achieve a repetitive antigen display on the nanoparticle surface, a peptide sequence that corresponds to the hydrophobic loop of actin was added at the C-terminus of the backbone polypeptide. The resulting nanoparticles were used as immunogen to produce monoclonal antibodies that specifically react with the actin epitope on the nanoparticle carrier as well as with the hydrophobic loop in cellular actin networks. Our studies show that the repetitive antigen display offered by the peptide nanoparticle carrier increases the immunogenic potential of otherwise poor antigens.

Materials and Methods

Reagents

Alexa Fluor 568-phalloidin, Alexa Fluor 488- and Alexa Fluor 633 carboxylic acid, succinimidyl ester were purchased from invitrogen Molecular Probes. DRAQ5 cell permeant DNA probe was obtained from Alexis Biochemicals.

Cells

HeLa and Rat2 fibroblasts (Leavitt et al. 1985) were grown in Dulbecco's minimal essential medium supplemented with 2 mM L-glutamine, 100 IU/ml penicillin, 100 μ g/ml streptomycin, and 10% FCS (DFCS) at 37°C, in a humidified atmosphere containing 5% CO₂. Cells were subcultured weekly up to 10 passages.

Construction of NP and NP-loop expression plasmids

The sequence encoding the nanoparticle peptide (NP; Figure 1A) was ligated into the *BamHI/EcoRI* restriction sites of mpPEP-T expression vector which corresponds to pPEP-T (Brandenberger et al. 1996) lacking the oligomerization domain. Oligonucleotides encompassing residues 263 to 274 of human β -cytoplasmic actin with additional modifications (Figure 1B) were cloned into the *XmaI/EcoRI* restriction sites of the NP expression construct. The resulting constructs are termed NP-L/C and NP-L/S.

Expression and purification of NP peptides

A culture of transformed *E. coli* BL21 DE3 pLys was grown in LB (containing 20 $\mu\text{g/ml}$ ampicillin and 30 $\mu\text{g/ml}$ chloramphenicol) at 37°C at 190 rpm until OD_{600} 0.5 - 0.6 was reached. Expression of the peptide was induced by 1 mM IPTG for 3-4 hrs. After pelleting, the cells were resuspended in lysis buffer (8 M urea, 100 mM NaH_2PO_4 , 10 mM Tris, 5 mM β -Mercaptoethanol, pH 8.0) and sonicated. Non-solubilized cellular fragments were removed by centrifugation (40 min at 17,000 rpm) and the supernatant was incubated with nickel beads (Sigma-Aldrich) for 2 hrs at room temperature (RT) and then loaded onto a Ni-NTA column. Unspecifically bound proteins were removed by washing buffer (8 M urea, 100 mM NaH_2PO_4 , 10 mM Tris, 5 mM β -Mercaptoethanol) with decreasing pH, pH 6.3, 5.9, 5.0. Finally, the NP peptide was eluted from the resin using the elution buffer (8 M urea, 100 mM NaH_2PO_4 , 10 mM Tris, 5 mM β -Mercaptoethanol, pH 8.0 containing 1 M Imidazole). The fractions containing the purified peptide were combined and dialyzed overnight against 8 M urea, 20 mM Tris/HCl, 150 mM NaCl, 10% glycerol, 2 mM DTT, 1 mM EDTA, pH 7.5. Protein concentration was determined by Bradford assay (Bio-Rad) and purity analyzed by 17% SDS-polyacrylamide gels.

Self-assembly of nanoparticles

Protein concentration was adjusted to 0.1 mg/ml and dialyzed overnight at RT against assembly buffer (8 M urea, 20 mM Tris/HCl, 150 mM NaCl, 10% glycerol, 2 mM DTT, pH 7.5). Refolding and self-assembly was achieved by sequential dialysis in assembly buffer with reducing urea concentrations.

Production of monoclonal antibodies

Monoclonal antibodies (mAbs) were generated by i.p. injection of 7-week old BALB/c mice with 50 μg NP-L/C nanoparticles mixed with 50 μl Pam₃Cys-Ser-(Ly)₄ Hydrochloride (Calbiochem) on day 1, 21, and 42. 4, 3, and 2 days before fusion, i.p. booster injections of 50 μg NP-L/C without Pam₃Cys-Ser-(Ly)₄ Hydrochloride were administered. After fusion, cloning and selection, antibody-producing hybridomas were screened for their binding to NP-L/C peptide by immunoblotting. Eleven out of 41 strongly reactive clones from two independent fusion events were subcloned. Isotype analysis revealed all established hybridomas to produce mAbs of the IgG2b subtype. Supernatants were grown either according to standard protocols or in serum-free medium (ISF-1, Biochrom, Berlin). MAbs were used as culture supernatant or purified by immunoaffinity chromatography using anti-mouse IgG-agarose (Sigma).

Immunoprecipitation

Purified mAb 1F1 was coupled to protein A sepharose CL-4B (Amersham Biosciences) following the suppliers protocol. After several washes with coupling buffer (20 mM sodium phosphate, pH 7.0), antibody-protein A sepharose beads were incubated with NP-L/C and NP, respectively, on a rocker for 1 hr at 4°C. After multiple wash steps with coupling buffer, the supernatant was removed and the pellet was resuspended in 5x SDS sample buffer, boiled for 5 min at 95°C, vortexed and pelleted again. The supernatants were separated on 17% SDS-polyacrylamide gels and further processed for immunoblotting.

Indirect Immunofluorescence

For immunofluorescence, cells were grown on glass coverslips for 24 - 48 hrs to subconfluency. Coverslips were rinsed twice with PBS before fixation. Different fixation protocols were used as indicated. Cells were either fixed for 10 min with freshly prepared 3% formaldehyde in PBS, for 15 min with formalin solution (Sigma), or for 15 min with -20°C MeOH. In some cases, cells were extracted for 5 min with 2% octyl-POE (*n*-octylpolyoxyethylene, Alexis) in modified Hanks' buffer (MHB; (Small and Celis 1978)) containing 0.12% glutaraldehyde prior to fixation by 1% glutaraldehyde for 20 min (Baschong et al. 2001). After several washes in MHB, aldehyde groups were quenched by two times 10 min incubations with 0.5 mg/ml NaHB₄ in MHB on ice. Appropriate dilutions of the primary antibody were incubated for 1 hr at RT. After several washes in PBS, coverslips were placed on a drop of Alexa Fluor 488-conjugated anti-mouse IgG (H and L chain, Alexis; 1/800) secondary antibody solution and incubated for 1 hr at RT. In some cases, Alexa Fluor 568-phalloidin (1/250; Molecular Probes) and/or DRAQ5 (1/250; Alexis Biochemicals) were

incubated together with the secondary antibody.

Confocal images were obtained using a 63x or 100x oil objective on a Leica TCS SP laser scanning confocal microscope. Digitized confocal images were processed by Leica software, Imaris 4.1 (Bitplane AG) and Adobe Photoshop 7.0.

Immunoelectron microscopy

For immunogold labeling, ultrathin sections of LR White embedded HeLa cells were mounted on 200 mesh carbon/parlodion coated copper grids. After blocking unspecific binding sites by two 5 min incubations in 2% BSA/PBS, grids were incubated on droplets of 1F1 antibody solution in a humidified chamber for 2 hrs at RT. Then the grids were rinsed with PBS, blocked with 2% BSA/PBS for two times 5 min, and incubated with a 10 nm gold-conjugated goat anti mouse IgG secondary antibody (BBInternational) for 1 hr at RT. After washing in PBS and distilled water, grids were stained with 6% uranyl acetate for 1 hr, rinsed with distilled water and then counterstained with lead-citrate for 2 min. For control experiments, the primary antibody was omitted (data not shown). Stained specimens were examined in a Hitachi H7000 transmission electron microscope operated at 100 kV. Micrographs were recorded on Kodak® electron image film SO-163.

Fluorescent labeling of antibodies and nanoparticles

Antibody solutions in PBS were labeled for 3 hrs at RT with a 6-fold molar excess of Alexa Fluor 633 carboxylic acid, succinimidyl ester according to the manufacturer's protocol. The labeling reaction was stopped by adding 1 M hydroxylamine HCl. The free Alexa Fluor 633 was removed by gel filtration chromatography (Sephadex G50) and overnight dialysis in PBS. The labeling of NP and NP-L/S with Fluor 488 carboxylic acid, succinimidyl ester was carried out accordingly in 20 mM Hepes, 150 mM NaCl, 10% glycerol, pH 7.5. Uncoupled Alexa Fluor 488 was also removed by gel filtration (Sephadex G50), followed by overnight dialysis in 20 mM Hepes, 150 mM NaCl, 10% glycerol, pH 7.5.

Acquisition of fluorescence images

Fluorescence images were recorded using a fluorescence confocal laser scanning microscope (ZEISS LSM 510 META, ZEISS AG). Solutions (5 μ l) of fluorescently labeled peptidic nanoparticles were added to special chambered quartz glass holders (Lab-Tek, 8-well, NUNC A/S). Acquisition of images was performed with a water immersion objective (40x, 1.2 NA, C-Apochromat) focusing the laser onto the bulk of the aqueous solution.

The sample was excited simultaneously with a 433 and a 633 nm laser using a main and a secondary dichroic mirror to exclude any excitation light in the detection channel. For the emitted light, one channel was configured for detecting the Alexa 488 dye (LP 505), and the other channel was configured for detecting the Alexa 633 dye (LP 650). In order to obtain high quality images of double-labeled particles, images with a size of 512 x 512 pixels, using 8-bit color depth, and a scan speed of 0.96 s/pixel were collected. To increase intensity the pinhole diameter of Alexa 488 and the Alexa 633 channel was set to 146 μm and 185 μm , respectively.

Fluorescence cross-correlation spectroscopy

Fluorescence cross-correlation spectroscopy (FCCS) has been described in great detail elsewhere (Schwille et al. 1997; Rigler et al. 1998). The cross-correlation curve is obtained by correlating the individual intensities emitted in the green (488 nm laser), and the red (633 nm laser) channel. The corresponding cross-correlation function can be written as

$$G_{gr}'(\tau) = 1 + \frac{N_{gr}}{(N_g + N_{gr}) \cdot (N_r + N_{gr})} \left[\frac{1}{\left(1 + \frac{\tau}{\tau_{D,gr}}\right)} \cdot \frac{1}{\sqrt{1 + R^2 \frac{\tau}{\tau_{D,gr}}}} \right] \quad \text{Equation 1}$$

where N_g , N_r , N_{gr} , and $T_{D,gr}$ describes the number of molecules labeled with the green dye, the number of molecules labeled with the red dye, the number of molecules labeled with both red and green dye, and the diffusion time of the double labeled species, respectively. The number of double labeled species, which is given by equation 4 when $T = 0$, can be expressed as

$$G_{gr}'(0) = 1 + \frac{\langle \delta I_g(t) \delta I_r(0) \rangle}{\langle I_g \rangle \cdot \langle I_r \rangle} = 1 + \frac{1}{N} = 1 + \frac{N_{gr}}{(N_g + N_{gr}) \cdot (N_r + N_{gr})} \quad \text{Equation 2}$$

which can simply be rearranged to

$$(G_{gr}'(0) - 1) \cdot (N_g + N_{gr}) \cdot (N_r + N_{gr}) = N_{gr} \Leftrightarrow N_{gr} = \frac{N_{AC,g} \cdot N_{AC,r}}{N_{CC}} \quad \text{Equation 3}$$

with $N_{AC,g}$, $N_{AC,r}$, and N_{CC} being the total number of molecules detected in the green channel, the red channel, and the apparent number of molecules in the cross-correlation channel,

respectively. Equations 1 to 3 are only true if no cross-talk from one channel to the other occurs. Measurements were performed with a Confocor2 (ZEISS AG) by exciting the sample with both the 488 and the 633 nm laser line, and using a beam line using a bandpass (BP 505-550 nm) and a longpass (LP 650 nm) for the green and the red detector channel, respectively. A small quantity (5 μ l) of the sample was pipetted to special chambered quartz glass holders (Lab-Tek, 8-well, NUNC A/S) and acquisition of data from the sample was assured by focusing the laser beam 200 μ m above the glass surface. Repeated (15 times) measurements of 3 seconds duration were performed in order to remove data with too high intensities. Auto- and cross-correlation curves were fitted with a Marquardt-Levenberg algorithm using the supplied ZEISS software package. Diffusion times for the used dyes Alexa 488 (20 μ s) and Alexa 633 (45 μ s) were measured and used for all subsequent fitting of correlation curves. The diffusion times of Alexa 633-labeled mAbs was determined to 380 μ s. NP-L/S labeled with Alexa 488 correspond to a diffusion time of 1160 μ s.

For binding tests, mAbs and nanoparticles were incubated together for 1 hr with gentle shaking at RT prior to FCCS analysis.

Actin preparation

Rabbit skeletal muscle G-actin was purified from acetone powder (Spudich and Watt 1971) with an additional gel filtration step on a Superdex S200 column (Amersham Biosciences) equilibrated in buffer A (2.5 mM imidazole, 0.2 mM CaCl₂, 0.2 mM ATP, 0.005% NaN₃, pH 7.4). Fractions from gel filtration columns were analyzed by SDS-PAGE. The protein concentration of fractions containing the respective G-actin purified to homogeneity was determined spectrophotometrically by absorbance at 290 nm using a molar extinction coefficient of $2.66 \times 10^4 \text{ M}^{-1}\text{cm}^{-1}$.

Cosedimentation assay

Purified rabbit skeletal muscle G-actin was precleared by centrifugation at 250.000 g for 1 hr at 4°C. The G-actin solution was carefully removed and polymerization was induced by adding 100 mM KCl or phalloidin and 100 mM KCl at a molar ratio of 2:1 for 3 - 5 hrs at 4°C. After centrifugation for 1 hr at 100.000 g at 4°C, the supernatant was removed and the pellet was washed with buffer F (buffer A containing 100 mM KCl) by centrifugation at 100.000 g for 15 min at 4°C. The pellets were resuspended in the initial reaction volume of buffer F and incubated for at least 2 hrs at 4°C to obtain a homogenous suspension of F-actin filaments.

For incubation of prepolymerized F-actin filaments with mAb 5B4, aggregates were removed from the purified antibody solution by centrifugation at 100.000 g for 1 hr at 4°C immediately

before incubation with the resuspended F-actin pellet fraction. MAbs were added to $\sim 5 \mu\text{M}$ F-actin solution to a final concentration of $\sim 0.12 \mu\text{M}$. After 1 hr incubation on a roller at 4°C , the mixtures were centrifuged at $100,000 \text{ g}$ for 1 hr at 4°C . Aliquots of the input (T), the supernatant (S) and the resuspended pellet (P) were separated by 15% SDS-PAGE and analyzed by immunoblotting. Actin was detected with a commercially available actin polyclonal Ab (A2066, SIGMA) followed by an alkaline phosphatase-conjugated goat anti-rabbit IgG secondary antibody. The presence of 5B4 heavy and light chains was visualized with an alkaline phosphatase-conjugated goat anti-mouse IgG secondary antibody.

Results

Peptide nanoparticles as platform for the repetitive display of antigenic determinants

To improve the antigenicity of a distinct actin epitope we took advantage of the repetitive and ordered display of the corresponding actin sequence on the surface of a peptide nanoparticle platform. The basic building block of the nanoparticles is a polypeptide that was computationally designed to form a regular icosahedron (Burkhard et al. 2000; Burkhard et al. 2001). In contrast to the original nanoparticles (Raman et al. 2006) which were assembled from a synthetic peptide, we produced nanoparticles from recombinantly expressed polypeptides. As shown in Figure 21 A, the recombinant core peptide of a nanoparticle is composed of two linked oligomerization domains, each containing particular coiled-coil heptad repeat patterns: an N-terminal 36 amino acid segment largely corresponding to the assembly domain of cartilage oligomerization matrix protein (COMP; green), which oligomerizes into pentamers (Kajava 1996), linked by a two amino acid linker sequence (black) to a de novo designed trimerization domain (blue). Compared to the minimal trimeric coiled coil domain in the synthetic polypeptide, the recombinant nanoparticle core polypeptide was extended at the C-terminus by the addition of 21 coiled-coil forming residues in order to ensure the protrusion of the C-terminus on the surface of the nanoparticle (Figure 21 C).

Following expression in *E. coli*, the polypeptide was purified under denaturing conditions using metal affinity chromatography. Refolding and self-assembly into nanoparticles was induced by a stepwise dilution of urea. According to the design principles and assuming an icosahedral symmetry of the nanoparticles, each particle should be composed of 60 copies of the polypeptide, with the C-termini at the particle's periphery. Consequently, peptide-based epitopes, which are inserted at the C-terminus through genetic engineering, are likely to be exposed on the particle surface. The surface-exposure of multiple copies of antigenic determinants in combination with the regular icosahedral symmetry that the nanoparticles

are designed to adopt (Figure 21 C), suggest that ‘loaded’ nanoparticles might represent an ideal repetitive antigen display system for eliciting an immune response.

In order to examine the immunogenic potential of such loaded nanoparticles, we have introduced a peptide epitope, which corresponds to residues 263 to 274 of the highly conserved human β -cytoplasmic actin molecule (Figure 21 B, red), at the C-terminus of the core polypeptide. We chose an actin sequence because its high degree of homology throughout different phyla and the reluctance of the immune system to react to self-antigens render it a challenging antigen. Actin is an abundant, highly dynamic protein in eukaryotic cells that assumes different forms within the cell, most prominently monomeric and filamentous (F-actin). As shown in the model of the F-actin structure (Figure 21 B; (Holmes et al. 1990; Lorenz et al. 1993)), the sequence from amino acid 263 to 274 forms a distinct structure, the so-called ‘hydrophobic loop’, which inserts into a hydrophobic pocket formed by a subunit of the opposite filament strand, and thus plays an important role in filament stability as well as in polymerization. Grafting the sequence that corresponds to the hydrophobic loop onto the nanoparticles allows us to test whether this platform is feasible for generating antibodies

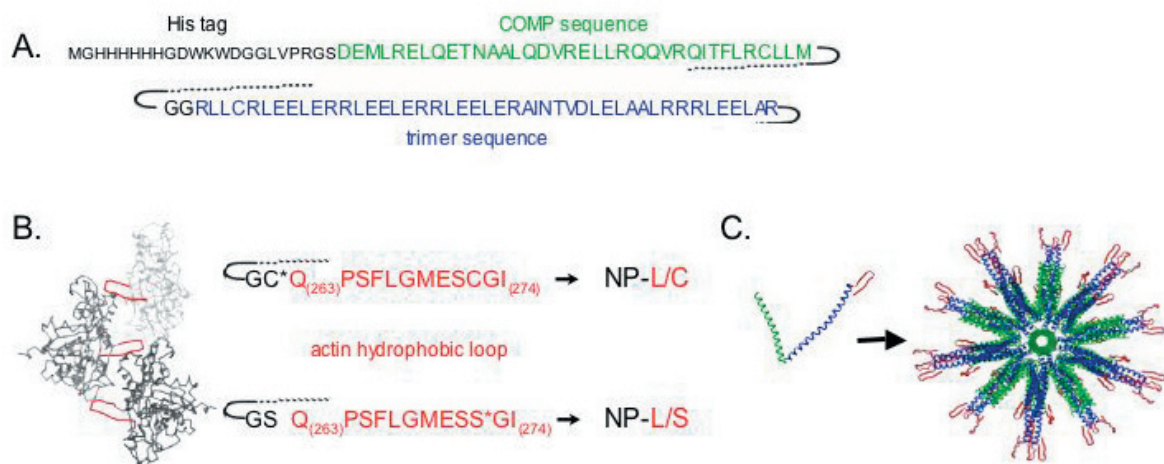


Figure 21. Design of peptide nanoparticles as a platform for repetitive actin epitope display. (A) Domain structure of the core polypeptide. The N-terminal histidine tag is followed by 36 amino acids that correspond to the slightly modified pentameric coiled coil domain of COMP (green). The second, C-terminal oligomerization domain consists of a de novo designed, 46 amino acid, trimeric coiled coil sequence (blue), which is linked to the pentameric domain by two glycine residues. (B) In the Holmes model of the F-actin filament structure (Holmes et al. 1990; Lorenz et al. 1993), the hydrophobic loop (red) corresponding to residues 262 to 274 in actin, inserts into a pocket formed at the interface between two adjacent subunits of the opposite strand. Amino acids 263 to 274 were grafted onto the C-terminus of the core polypeptide downstream of a glycine/cysteine linker (black). The resulting polypeptide termed NP-L/C contains two closely spaced cysteine residues, whereas the NP-L/S polypeptide contains serines at these positions. Exchanged amino acids are indicated by asterisks. (C) Computer model of the assembled NP-L/C nanoparticle with icosahedral symmetry.

that recognize a distinct structural element. In order to further stabilize the loop structure, we exchanged the glycine residue in the core polypeptide by a cysteine to allow for disulfide bonding with the cysteine residue of the epitope sequence near the C-terminus. The resulting construct was expressed, purified and refolded into NP-L/C particles, which were used for immunization of mice as described in *Materials and Methods*. In a second construct termed NP-L/S, the two cysteine residues near the C-terminus were replaced by serine.

Assembly of peptides containing actin loop epitopes into nanoparticles

Based on the *in silico* predictions shown in Figure 21 C and on previous data obtained with a synthesized core polypeptide (Raman et al. 2006), we would expect the recombinant polypeptides to assemble into a homogenous population of spherical particles. As illustrated by the electron micrograph in Figure 22, self-assembly of the core polypeptide produced mostly spherical nanoparticles. The nanoparticles exhibited a fairly uniform morphology with an outer diameter of approximately 30 nm for negatively stained samples. Based on the computer model, a diameter of 20.3 nm was predicted for native nanoparticles. Electron micrographs revealed a minor fraction of the core polypeptide to form smaller structures. We cannot distinguish whether they represent assembly intermediates or fragments of dissociated nanoparticles.

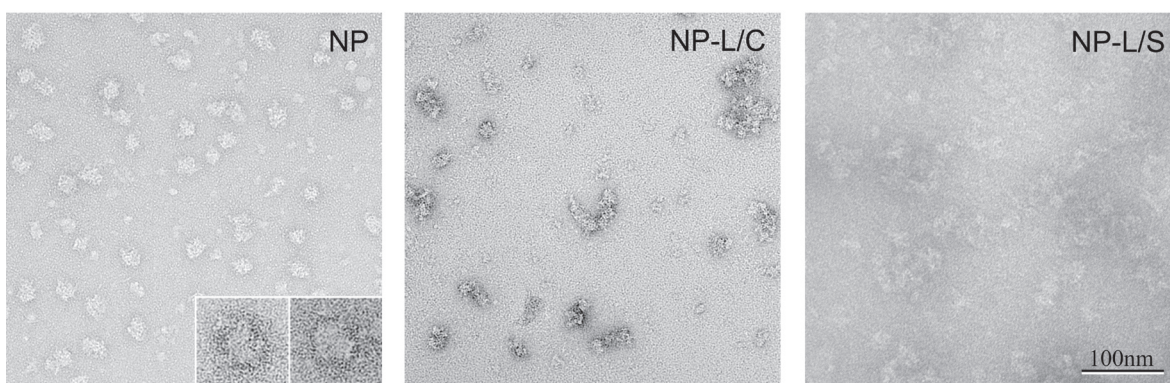


Figure 22. Transmission electron micrographs of peptide nanoparticles. After refolding of recombinantly expressed polypeptides, samples were adsorbed on carbon-coated grids and negatively stained with 2% uranyl formate. Core polypeptides assemble into single, spherical nanoparticles (NP). They are fairly homogenous in size with a diameter of ~ 30 nm. The frame size of the inset is 68 nm. NP-L/C particles display a tendency to aggregate under oxidizing conditions. Replacing the cysteine residue of the actin loop epitope by serine in the NP-L/S polypeptide yielded single homogenous nanoparticles with a diameter of ~ 25 nm.

Under oxidizing conditions, nanoparticles without an epitope were monodisperse with little tendency to aggregate. In contrast, electron micrographs revealed extensive aggregation of negatively stained NP-L/C (middle panel). Only a minor fraction of the polypeptides assembled into single spherical structures that appeared to be slightly smaller than nanoparticles. Because the NP-L/C polypeptide contains two cysteine residues near the protruding C-terminus, it is likely that at high protein concentrations, disulfide bonds are formed also between particles, causing their aggregation. To test this hypothesis, we produced NP-L/S particles where both cysteines at the C-terminus were replaced by serine residues, under oxidizing conditions. Electron micrographs of negatively stained NP-L/S (right panel) reveal individual spherical nanoparticles with outer diameters ranging from 20 to 25 nm. Based on the computer model, the diameter of particles that carry the actin epitope was calculated to be 23.3 nm. Similar to the ‘bare’ nanoparticles, smaller structures were also observed in negatively stained NP-L/S samples. Dynamic light scattering measurements of NP-L/S particles revealed a largely monodisperse size distribution of nanoparticles with a hydrodynamic diameter that is consistent with the EM data (data not shown).

Characterization of monoclonal antibodies raised against NP-L/C

For the production of monoclonal antibodies (mAb), mice were repeatedly immunized intraperitoneally with 50 μg purified NP-L/C particles per injection following the protocol described in *Materials and Methods*. Hybridoma supernatants were initially tested by an ELISA assay using purified rabbit skeletal muscle actin and a dot blot assay against NP-L/C polypeptide (data not shown). A number of reactive hybridoma clones from independent fusions were identified. Isotype determination revealed that all clones produced IgG2b antibodies. To characterize the epitope specificity under denaturing conditions, we carried out immunoblots with individual hybridoma supernatants. Figure 23 A shows a representative blot of refolded NP-L/S and NP-L/C, purified rabbit skeletal muscle actin and total cell extracts from HeLa cells probed with the randomly selected mAb 1F1. In NP-L/S and NP-L/C preparations, the antibody reacts with a band migrating at approximately 15 kDa. The electrophoretic mobility of this band correlates with the calculated molecular mass of the monomeric forms of the NP-L/C and NP-L/S polypeptide (approximately 14 kDa). The additional bands detected by 1F1 most likely correspond to dimeric and higher oligomeric species of the respective polypeptides. Probing a parallel blot with an antibody against the histidine tag present at the N-terminus revealed the same pattern, indicating that these bands represent full-length polypeptides (data not shown). To demonstrate that the 1F1 mAb is directed against the actin epitope sequence and not against the core polypeptide, we loaded purified skeletal muscle actin and a total cell extract of HeLa cells on the gel. 1F1 bound to the 42 kDa actin band and to a corresponding band in the cellular extract. Similar results were obtained with six different hybridoma lines (data not shown).

The immunoblotting experiments indicated that the mAbs obtained from immunization with NP-L/C recognize the denatured actin epitope sequence engineered onto the C-terminus of the core polypeptide in NP-L/C and NP-L/S, as well as in its native context. Under denaturing conditions, the cysteine residue corresponding to Cys272 in actin do not seem to be essential for antibody specificity.

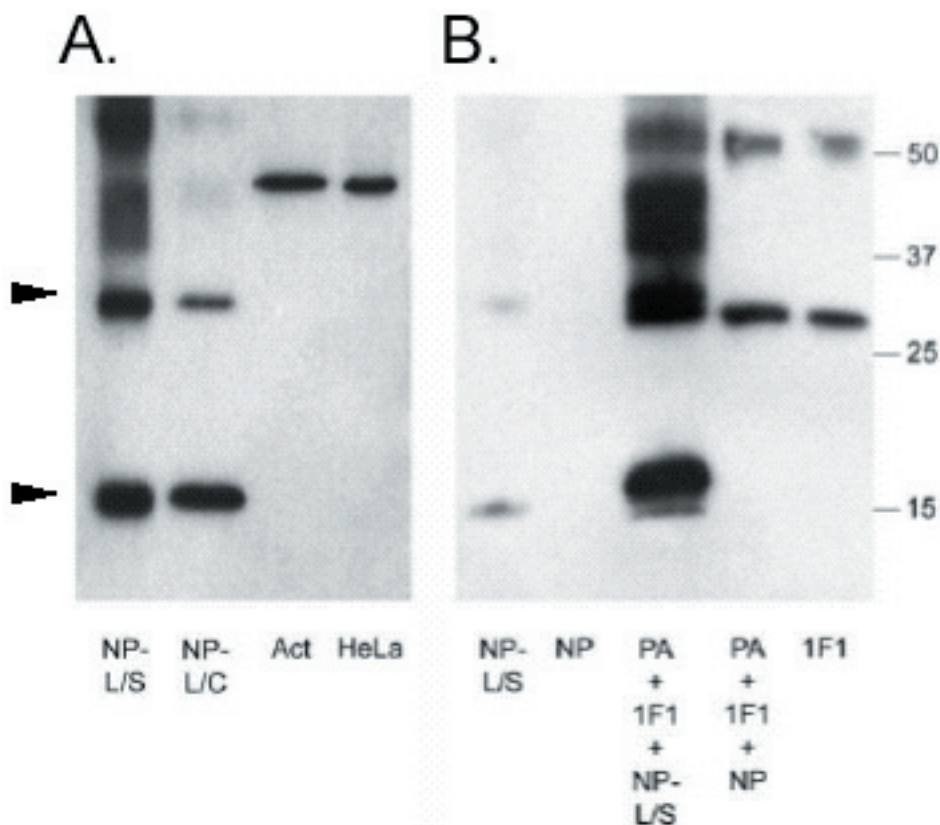


Figure 23. Immunoblotting characterization of mAb 1F1 specificity. (A) Purified NP-L/C and NP-L/S particles, purified skeletal muscle actin (Act), and total protein extracts from HeLa cell were separated on 15% SDS-polyacrylamide gels, blotted and probed with mAb 1F1. The antibody reacts with monomeric, dimeric (arrowheads) and oligomeric species of NP-L/S and NP-L/C polypeptides under denaturing conditions. 1F1 does not react with the core polypeptide NP (see panel B). The 1F1 epitope is also detected in purified actin. In HeLa cell extract, a single band with an electrophoretic mobility comparable to that of actin is recognized. (B) Immunoprecipitation of NP-L/S nanoparticles. Protein A sepharose beads (PA) were saturated with 1F1 and then incubated with NP or NP-L/S nanoparticles under native conditions. Immunoprecipitated complexes were separated on a 15% SDS-polyacrylamide gel. Purified NP, NP-L/S, and 1F1 mAb were loaded as controls. The blot was probed with 1F1 and immunoreactive bands were revealed by an alkaline phosphatase-conjugated secondary anti-mouse IgG. The secondary Ab does not cross-react with NP nanoparticles but reveals the heavy and light chains of the mAb, both in the immunoprecipitate and in the control lane with purified 1F1. The molecular masses (in kDa) of standard proteins are indicated on the right.

To examine the exposure of the epitope on the particle surface, we carried out immunoprecipitation experiments with assembled particles and subsequently blotted the immunoprecipitated complexes (Figure 23 B). Because the NP-L/C particles tended to aggregate, monodisperse NP-L/S particles were used for these experiments. Protein A sepharose beads were saturated with purified 1F1 mAb and then incubated with NP or NP-L/S under non-denaturing conditions. Precipitates, as well as directly applied NP and NP-L/S particles and purified 1F1, were separated on SDS-PAGE and subsequently blotted. As illustrated in Figure 23 B, immunoblotting showed that protein A-bound 1F1 only precipitated the particles carrying the actin epitope (NP-L/S) and not the 'empty' particles (NP). Directly loaded samples confirmed that 1F1-reactive bands were only seen in NP-L/S and not in NP.

In addition to the 1F1 mAb, we tested the specificity of four other hybridomas, 5B4, 4A7, 3E3 and 6E2, that were independently established after immunizing mice with NP-L/C particles, in biochemical assays. All mAbs specifically bound to nanoparticles carrying the actin epitope and detected actin in whole cell extracts under denaturing conditions (data not shown).

Binding of 1F1 mAb to NP-L/S visualized by fluorescence microscopy

The specificity of the binding between 1F1 and the NP-L/S in solution was determined by using both fluorescence microscopy and fluorescence cross-correlation spectroscopy (FCCS). For this purpose, purified antibodies and the peptide nanoparticles were labeled with the fluorescent dyes Alexa 633 and Alexa 488, respectively. An unrelated mAb of the same isotype as 1F1 was used as control. A fluorescent micrograph of a mixture of labeled mAbs and labeled NP-L/S is shown in Figure 24 A. The image reveals a fairly even distribution of NP-L/S particles (green dots in Figure 24 A) and antibodies (red dots in Figure 24 A). Fluorescence micrographs as well as FCCS data indicate that both antibodies and peptide nanoparticles aggregated slightly, despite pre-clearing by high-speed centrifugation or filtration (data not shown). A similar distribution was observed in images of a sample containing a mixture of a labeled control mAb and labeled NP-L/S (Figure 24 B). In contrast to the unspecific control antibody, which did not colocalize with the NP-L/S (merged image in Figure 24 B), there is a significant amount of dots that colocalized in the mixture containing 1F1 and NP-L/S (orange dots in the merged image of Figure 24 A). There is a number of dots that apparently do not colocalize in Figure 24 A, probably because not all labeled 1F1 and NP-L/S were exactly in the respective focal plane. Because the resolution of the light microscope is diffraction-limited to about 300 nm, colocalization only reveals that the differently labeled molecular species are close in space, whereas individual molecular interactions cannot be resolved. In addition, the confocal fluorescence micrographs are acquired with a photon multiplier tube detector that does not have single molecule sensitivity, i.e. individual nanoparticles are too small to be visualized. Hence, the conclusions drawn from the images in Figure 24 are based

on a qualitative assessment of the interaction between the specific antibody and the NP-L/S particles.

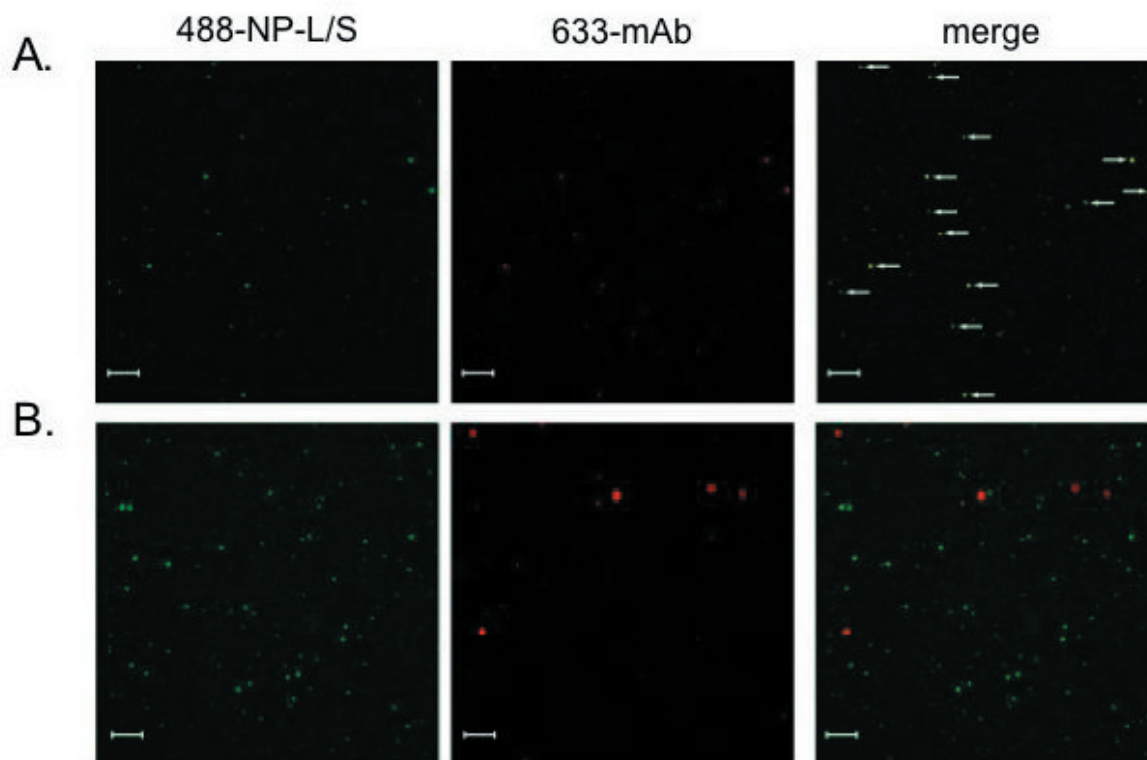


Figure 24. Specific binding of mAb 1F1 to NP-L/S nanoparticles visualized by fluorescence microscopy. Images were collected by focusing the laser beam in the bulk of small droplet (10 μ l) containing an aqueous solution of (A) labeled 1F1 and NP-L/S, and (B) an aqueous solution of labeled IgG2b control antibody and NP-L/S (negative control). Antibodies were labeled with Alexa 633, whereas the NP-L/S was labeled with Alexa 488. Fluorescence micrographs in the left and middle panel show images obtained in the green and red detection channel, respectively. The superposition of the green and red images is presented in the right panel. Colocalized, white/yellow particles (brightest particles are marked by white arrows) represent binding events of 1F1 mAb to NP-L/S. No colocalization was observed with the 633-control mAb (B, right panel).

Binding of 1F1 to NP-L/S is confirmed by fluorescence cross-correlation spectroscopy

In addition to the acquisition of fluorescence micrographs, binding of 1F1 mAb to NP-L/S was evaluated by FCCS. This single-molecule detection fluorescence spectroscopic technique is based upon the diffusion properties of fluorescently labeled species and is able to provide a yes or no answer if binding between two differently labeled partners, here an antibody and a nanoparticle, occurs. It allows for the determination of the concentration and dynamics of each individual, labeled protein as well as the double-labeled protein complexes, which in

our case correspond to the binding of Alexa 633-1F1 emitting in the red to Alexa 488-NP-L/S particles emitting in the green. An unspecific Alexa 633-mAb of the same isotype incubated with Alexa 488-NP-L/S particles served as negative control. Figure 25 A depicts the cross-correlation curves obtained from incubations of the specific 1F1 mAb with NP-L/S particles (black curves) and the control incubations with the unspecific mAb (blue curves). Mixing the specific 1F1 with NP-L/S leads to a significantly higher cross-correlation amplitude in comparison to the negative control. Binding becomes more overt in the normalized cross-correlation curves shown in Figure 25 B. The diffusion time derived for the 1F1-nanoparticle complex is 1962 μs (black curve) which correlates well with its approximate molecular weight (about 1000 kDa), whereas the corresponding diffusion time in the negative control experiment was 1046 μs . This difference, together with the significantly smaller amplitude obtained in measurements with the control mAb, indicate that 1F1 specifically binds to NP-L/S. Furthermore, a significant fraction of the auto-correlation curve recorded in the red detector channel corresponds to the diffusion time characteristic for the specific 1F1-NP-L/S complex formation (1950 μs). This fraction could not be detected with control mAb. The reason for the amplitude in the cross-correlation curve of the negative control experiment could be related to non-specific binding, but also to emission cross-talk which leads to an apparent increase in the cross-correlation amplitude.

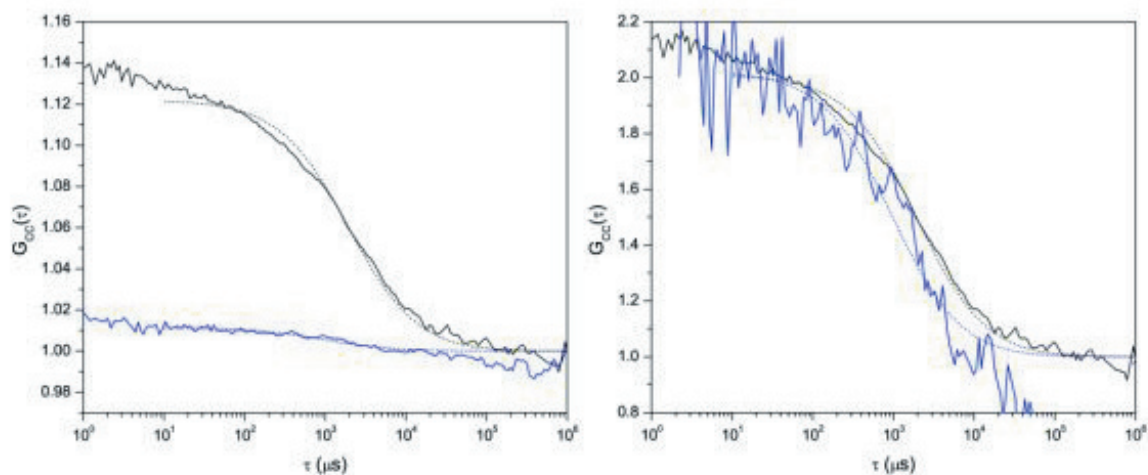


Figure 25. Binding of 1F1 mAb to NP-L/S examined by fluorescence cross-correlation spectroscopy. Left panel depicts the cross-correlation curves of a mixture of the Alexa 633-labeled 1F1 mAb and NP-L/S labeled with Alexa 488 (in black), and cross-correlation curves of a mixture of a control IgG2b mAb labeled with Alexa 633 and NP-L/S labeled with Alexa 488 (in blue). Corresponding normalized cross-correlation curves are presented in the right panel. Experimental data are shown as solid lines whereas the corresponding fit is depicted as a dotted line.

These results clearly indicate that specific binding between the 1F1 mAb and the NP-L/S particles occurs whereas binding of an unrelated antibody to NP-L/S particles is very low and can thus be considered non-specific. In support of this notion, control experiments performed with mixtures of labeled 1F1 mAb and ‘bare’ nanoparticles without an actin-derived epitope (NP) failed to show any antibody-antigen interactions (data not shown).

1F1 detects the hydrophobic loop epitope *in situ*

To determine whether the mAbs raised against nanoparticles displaying the hydrophobic actin loop sequence recognize the actin epitope in its native environment, we labeled Rat2 fibroblasts, which establish an extensive network of actin stressfibers, by indirect immunofluorescence and compared the staining pattern of 1F1 (Figure 26, upper panels) and

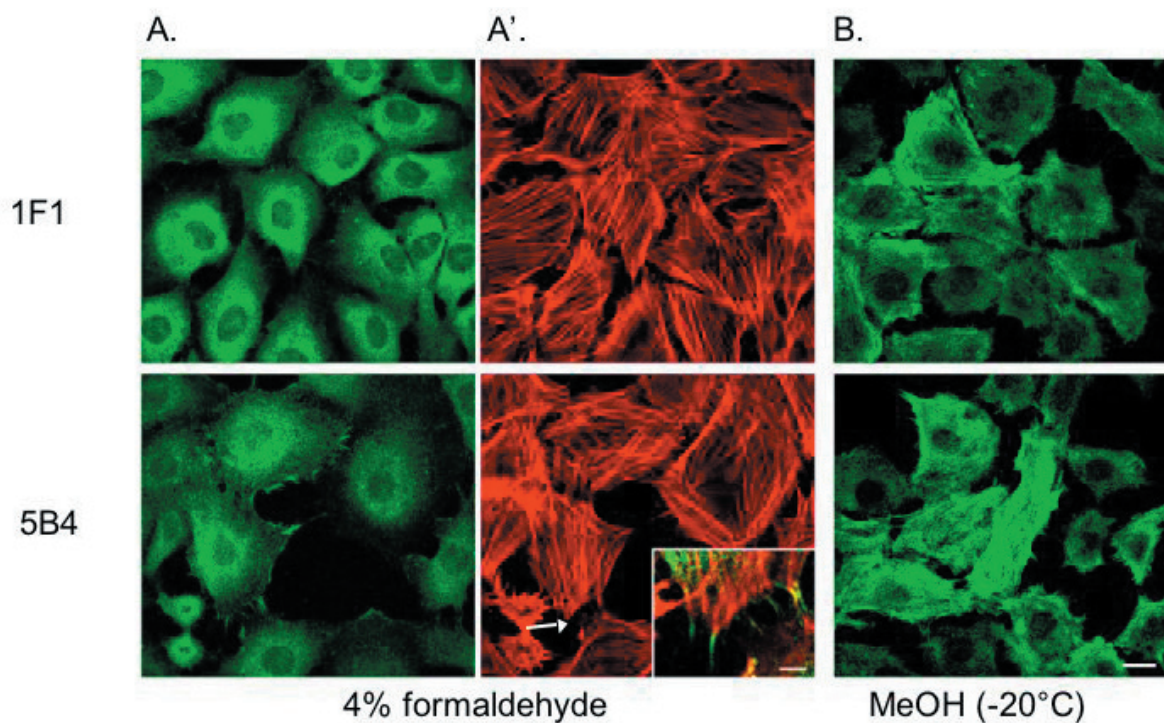


Figure 26. Cellular localization of the 1F1 and 5B4 epitope. (A) In Rat-2 fibroblasts that were fixed with 4% formaldehyde and permeabilized with 0.2% Triton X-100, 1F1 and 5B4 display a fine punctate staining pattern throughout the cytoplasm and the nucleus. Filopodial extensions at the cell periphery are prominently labeled. (A') Counterstaining of the cells with 568-phalloidin revealed the F-actin stress fibers and shows that both antibodies do not bind to filamentous actin under these conditions. The inset shows the merged image of the area indicated by the arrow at higher magnification. Actin at the tips of filopodial extensions is labeled by 5B4, but not by 568-phalloidin. Bar inset, 5 μm . (B) Fixation of rat2 fibroblasts with -20°C MeOH denatures stress fibers and permits binding of both mAbs to filamentous actin. Bar, 10 μm .

5B4 (lower panels) to that of phalloidin-positive filamentous actin. In Rat2 cells fixed with 4% paraformaldehyde and then permeabilized with 0.2% triton-X100 (Figure 26 A), 1F1 and 5B4 showed a fine disperse, slightly punctate staining throughout the cell. Consistent with the previously reported distribution of non-filamentous actin in the cytoplasm and the nucleus (Schoenenberger et al. 2005). 1F1 and 5B4-labeling was also found in both cellular compartments. Moreover, a pronounced staining of filopodial extensions at the cell periphery was observed in some cases. The staining pattern was clearly distinct from that of filamentous actin revealed by phalloidin (Figure 26 A'). However, when Rat2 cells were fixed with -20°C methanol (Figure 26 B), which results in partial denaturation and precipitation of cellular structures, the antibody labeling appeared to be more stressfiber-like. This finding suggests that MeOH had to some extent unmasked the binding site of 1F1 (and 5B4) in filamentous actin.

The accessibility of the 5B4-binding site in isolated F-actin filaments was studied by highspeed cosedimentation assays (Figure 27). As expected, pre-polymerized F-actin filaments were pelleted by centrifugation at 100.000 g (left panel), whereas purified 5B4 immunoglobulin remained in the supernatant. A similar distribution was observed when 5B4 was incubated together with F-actin filaments prior to centrifugation (right panel). The faint band representing small amounts of 5B4 light chain in the pellet fraction might represent antibody reacting with the free ends of filaments. The data from cosedimentation experiments support the notion that the epitope recognized by 1F1 and 5B4 is buried in filamentous actin.

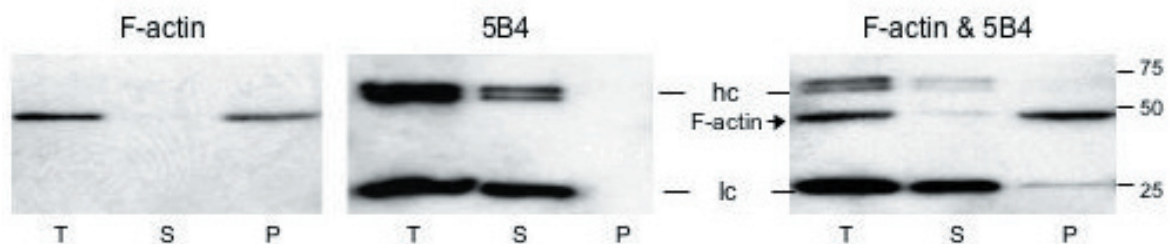


Figure 27. 5B4 does not bind to native F-actin filaments. The interaction of purified 5B4 with phalloidin-stabilized F-actin filaments was analyzed by high-speed cosedimentation assays. Blots of the total protein input (T), the supernatant (S) after centrifugation and the resulting pellet (P) were probed with a polyclonal actin antibody. Left panel, phalloidin-stabilized F-actin filaments were completely pelleted by the applied centrifugal forces. Middle panel, high-speed centrifugation does not pellet the purified antibody. Right panel, the majority of the antibody remained in the supernatant after cosedimentation with F-actin filaments. The molecular masses (in kDa) of standard proteins are indicated on the right. hc, heavy chain, lc, light chain.

Subcellular distribution of the 1F1 epitope

To further investigate the subcellular distribution of the hydrophobic loop antigen at the ultrastructural level, we carried out post-embedding indirect immunoelectron microscopy on ultrathin sections of HeLa cells and neonatal rat heart tissue (Figure 28). We chose HeLa cells because of their relatively large nucleus compared to the total cell volume and cardiac muscle tissue because of the abundance of actin filaments that are highly organized in sarcomeres. The sections were labeled with 1F1 and then incubated with a 10 nm colloidal gold-conjugated goat anti mouse IgG. Control incubations without the primary antibody showed that there was virtually no background labeling of HeLa cells or cardiac tissue under the experimental conditions chosen (data not shown). Consistent with the immunofluorescence labeling of Rat2 cells shown above, gold particles were detected throughout the cytoplasm (c) and the nucleus (n) in both cell types. The distribution of the gold particles appeared to be random, without an evident association with any distinct structure. In particular, there was no conspicuous labeling of thin filaments in the cardiac muscle tissue (Figure 28 B), supporting the notion that the antigen is concealed in the F-actin filament. Immunogold labeling of HeLa cells and cardiomyocytes confirmed that mAbs raised against NP-L/S particles detect the hydrophobic loop of actin primarily in non-filamentous actin where it is exposed.

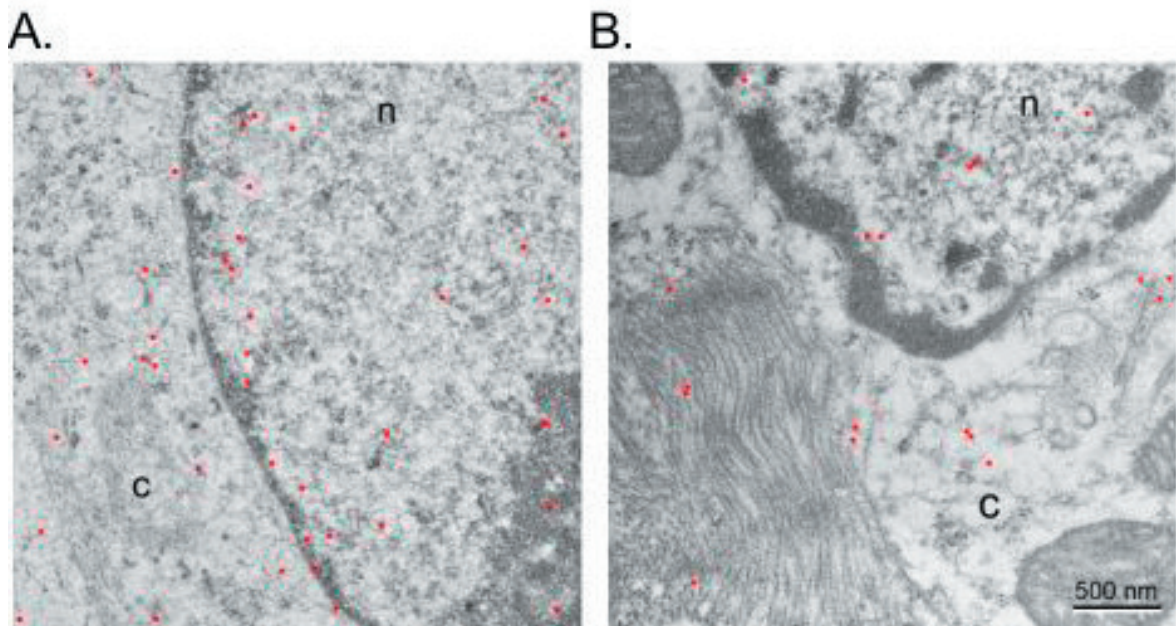


Figure 28. Cellular distribution of the 1F1 epitope at the ultrastructural level. Ultrathin sections of HeLa cells (A) and neonatal rat cardiomyocytes (B) were labeled post-embedding with 1F1 and a 10 nm gold-conjugated secondary antibody (enlarged, pseudocolored red). Immunogold labeling confirms that the actin conformation recognized by 1F1 is present in the cytoplasm (c) and the nucleus (n). A distinct labeling of thin filaments in the sarcomeres of cardiomyocytes is not evident.

Discussion**Repetitive surface display on peptide nanoparticles turns conserved actin sequences into potent immunogens**

Antibodies that recognize distinct structural elements are important tools to examine the distribution, assembly, and ultimately the function of supramolecular actin structures. Because actin is an extremely conserved molecule, peptides used for immunization are likely to be almost identical to the actin of the host and therefore, self-tolerance will prevent the induction of a strong immune response. Consequently, the production of specific actin antibodies has proven notoriously difficult. In those cases where the epitope has been mapped, antibodies raised against actin or peptides thereof predominantly recognize regions of the more variable aminoterminal (Skalli et al. 1986; Gimona et al. 1994). A small number of highly interesting antibodies have been obtained by using distinct forms of actin as immunogen rather than peptides corresponding to specific actin sequences. For example, immunization with actin complexed to profilin led to a mAb termed 2G2, which binds to a non-sequential actin epitope (Gonsior et al. 1999).

Besides several forms of denatured actin, 2G2 recognizes a specific conformation of native actin, which is present in the nucleus of certain cell types and specified by compaction of the antibody-reactive region into a coherent patch. Another antibody that reveals distinct forms of nuclear and cytoplasmic actin has been obtained by immunizing mice with a covalently cross-linked antiparallel actin dimer (Schoenenberger et al. 2005). Furthermore, autoantibodies that recognize predominantly filamentous actin have been found in patients with type 1 autoimmune hepatitis (Silvestrini and Benson 2001; Granito et al. 2006).

The ability of actin to polymerize into highly ordered, two-stranded helical filaments is an intrinsic property of all actins and thus sequences involved in the establishment of F-actin filaments are amongst the most conserved. Moreover, sequences that are involved in subunit contacts along and between the axial strands are in general not readily accessible for antibody binding. For example, amino acids 263 to 274 which form the 'hydrophobic loop', represent a highly conserved, distinct structural feature that lies buried in the filament. Because it presumably is a difficult antigen, we chose this particular sequence to test the immunogenic potential of peptide nanoparticles.

The display of peptides or proteins in an ordered, repetitive array is known to enhance their immunogenic potential. For example, pattern recognition by the immune system is efficiently stimulated by the highly ordered and repetitive structure of virus-like particles (VLPs). A number of VLPs, such as Tobacco mosaic virus (TMV; (Palmer et al. 2006; Smith et al. 2006)) human papilloma virus and Hepatitis B VLPs, have been modified to function as scaffolds for the surface display of peptide epitopes (Jennings and Bachmann 2008). Repetitive antigen display systems as B-cell epitope carriers have so far largely involved

viral capsid structures. As an alternative, we have recently designed a novel tool for repetitive antigen display: using different protein oligomerization domains we have designed peptide nanoparticles with predicted icosahedral symmetry similar to viral capsids (Raman et al. 2006).

Like VLPs, the polyhedral symmetry of peptide nanoparticles represents an ideal 'rig' for repetitive antigen display, but nanoparticles offer additional advantages. In particular, the expression vector used in this study can easily be customized with an antigenic epitope at either end of the sequence as both, the N-terminal and the C-terminal ends of the peptide sequence extend from the nanoparticle surface. Hence, an antigenic peptide sequence at the C-terminus of the construct will be repetitively displayed at the surface of the nanoparticle. It has previously been shown that such a repetitive antigen display will substantially increase the level and specificity of antibodies in response to a given antigen (Baschong et al. 2003).

The backbone peptide chain of the first generation nanoparticles was produced by solid-phase peptide chemistry (Raman et al. 2006). In this study, we have generated an expression vector which allows not only C-terminal modification of the peptide by genetic engineering, but also the easy and fast recombinant expression of the epitope-tagged peptides in *E. coli*. Furthermore, a hexahistidine tag at the N-terminus facilitates downstream purification of nanoparticle peptides. The ultrastructural morphology of basic nanoparticles assembled from recombinantly expressed backbone peptide is comparable to that of nanoparticles assembled from the synthetic peptide. The size of both types of negatively stained nanoparticles was determined to be approximately 25 nm in diameter. After taking into account artifacts introduced by sample preparation and negative staining, this number corresponds well to the diameter of 20.3 nm calculated from the computer model. For negatively stained NP-L/S, which carry the hydrophobic loop epitope at the C-terminus of the backbone polypeptide, the average diameter was 22.1 nm. Thus, the NP-L/S appear to be not only smaller than the calculated 23.3 nm, but also smaller than the nanoparticle without the epitope. It is possible that the epitope affects the folding and assembly of the core polypeptide in such a manner that it differs from the modelled icosahedral structure. Our ongoing biophysical analyses with other nanoparticle constructs indicate that in fact the number of peptide chains that assemble into a single nanoparticle may differ from the 60 peptide chains that are expected to form an T1 icosahedron. Nevertheless, the immunoprecipitation experiments and FCCS using NP-L/S indicate that the epitope is indeed exposed on the surface of these particles.

That folding and assembly of nanoparticles are sensitive to the nature of the epitope is further confirmed by the introduction of an additional cysteine at the base of the actin loop sequence, which resulted in the aggregation of NP-L/C particles under oxidizing conditions. It is possible that during assembly this cysteine residue is buried whereas the C-terminal cysteine is fully exposed in high density on the surface of the nanoparticles, and thus, disulfide bonding more readily occurs between the C-terminal cysteines of neighboring particles even at low concentration. This aggregation may even have played an adjuvant

role in the overall immune response raised against NP-L/C particles by promoting a local inflammatory response. However, administration of disperse peptide nanoparticles carrying a profilin epitope effectively triggered the immune response (Murk et al., manuscript under revision). In addition, recent studies demonstrate that 25 nm-nanoparticle vaccines were significantly more efficient than 100 nm-particles in stimulating adaptive immunity (Reddy et al. 2007).

Immunization with NP-L/C allowed the establishment of several different hybridoma cell lines. The subclass of the mAbs were all of the IgG2b isotype indicating that using nanoparticles as a platform for repetitive antigen display shifts the immune response towards a less inflammatory T helper type 2-like response (Chackerian et al. 2006).

Antibody specificity

To demonstrate the specific binding of monoclonal loop antibodies to the actin epitope exposed on NP-L/S particles at the molecular level, we used fluorescence correlation spectroscopy. The advantage of this emerging technique is that interactions between molecules can be determined through their correlated motion in equilibrium solution, independent of molecular orientation. A number of recent studies have used fluorescence correlation spectroscopy to measure antigen-antibody interactions (Lagerkvist et al. 2001; Grunwald et al. 2005; Ruan and Tetin 2008). The combination with a confocal microscope will not only improve signal to noise ratios in spectroscopic measurements, but also allows simultaneous confocal imaging of the labeled specimen. Confocal images (Figure 24) of Alexa 488-labeled particles and Alexa 633-labeled antibodies revealed that some aggregation had occurred in both specimens even at optimized concentrations. Although individual nanoparticles, not to mention the significantly smaller antibodies, are below the limits of resolution, aggregation resulted in dot sizes that were within the resolution of the light microscope. Correct conclusions about the number of antibodies bound or binding constants are difficult because the fluorescence intensity of labeled particles is modified by intermolecular quenching and thus, determination of the actual number of fluorescently labeled epitopes very arduous. Another reason for the difficulty to determine stoichiometry and binding affinity is related to the fact that the number of fluorophores coupled to an antibody cannot be standardized. For instance, it has been shown that when IgGs, which contain two independent epitope binding sites, statistically carry one fluorophore, approximately one third of the molecules are not labeled and will lead to a significant reduction of the cross-correlation amplitude. Nanoparticles, which are assembled from presumably sixty peptides, are even more prone to being nonuniformly labeled. Moreover, because of the close spacing of the epitopes with respect to the dimensions of the antibody, there will be significant steric hindrance. Although we do not know how many antibodies are bound to an individual particle, merged images of labeled loop antibodies versus control antibodies clearly demonstrate a specific

interaction between loop antibodies and NP-L/S. The specificity was further confirmed by using nanoparticles with an unrelated epitope (data not shown).

Improvement of labeling protocols and careful optimization of the instrumentation will be necessary to achieve the highest cross-correlation signal and for further characterization of the NP-L/S interactions with the loop antibodies.

Antibodies raised against loop nanoparticles detect cellular actin

Immunolabeling of HeLa cells with mAbs raised against NP-L/C revealed that the loop epitope, which corresponds to aa 262 - 274 in actin, is also recognized in its native structure *in situ*. According to the F-actin filament model (Holmes et al. 1990), the hydrophobic loop structure is involved in contacts between axial strands and thus is buried in the filament (Figure 21 B). Moreover, a detachment of the hydrophobic loop 262 - 274 from the monomer surface, and its perpendicular extension and insertion into protomers of the opposite strand is required for F-actin filament formation and stability. As a consequence of this protected location, loop mAbs 1F1 and 5B4 predominantly recognized non-filamentous actin with a more accessible loop structure in the cytoplasm of formaldehyde fixed cells. This staining pattern is similar to the one observed with the previously published actin mAb 1C7 that binds to amino acids 194 - 202, which also lie buried within the filament (Schoenenberger et al. 2005). However, treatment with ice-cold methanol at least partially uncovered the loop epitope and revealed a stressfiber-like pattern in 1F1 and 5B4 labeled cells. In contrast, the epitope recognized by 1C7 is involved in subunit contacts along the helical strands and remains shielded even after methanol treatment. Intriguingly, 1F1 seems to bind to the hydrophobic loop in non-filamentous and filamentous actin under these conditions, although the loop is predicted to undergo a conformational change to stabilize the filament in the prevailing Holmes model (Holmes et al. 1990).

Our data show that by grafting an actin-related epitope onto the surface of designed peptide nanoparticles we were able to tailor antibodies that bind to a specific actin structure *in situ*. To substantiate that a nanoparticle-induced immune response is generally applicable for isolating antibodies against refractory antigens, we recently employed this innovative method to produce profilin1-specific mAbs, which can be used elucidate the different functions of profilin isoforms (Murk et al., manuscript under revision). Therefore, nanoparticles could serve as a highly versatile and convenient platform for the development of synthetic subunit vaccines.

Acknowledgments

We gratefully acknowledge the help of Rosmarie Sütterlin (M.E. Müller Institute for Structural Biology, University of Basel) with immunofluorescence. This work was supported by a grant from the Swiss National Science Foundation (to CAS), the Deutsche Forschungsgemeinschaft (BMJ) and the M.E. Müller Foundation.

2.6 Immunoelectron microscopy of peptide nanoparticles

2.6.1 Immunoelectron microscopy of peptide nanoparticles yielded ambiguous results

To further characterize the binding of antibodies to nanoparticles at the ultrastructural level, we attempted to employ immunogold electron microscopy.

Direct immunogold labeling of nanoparticles in solution with 5B4-Au yielded gold particles attached not only to the nanoparticles but also to the EM-grid itself (Figure 29). Hence, actual binding events could not be distinguished from background noise.

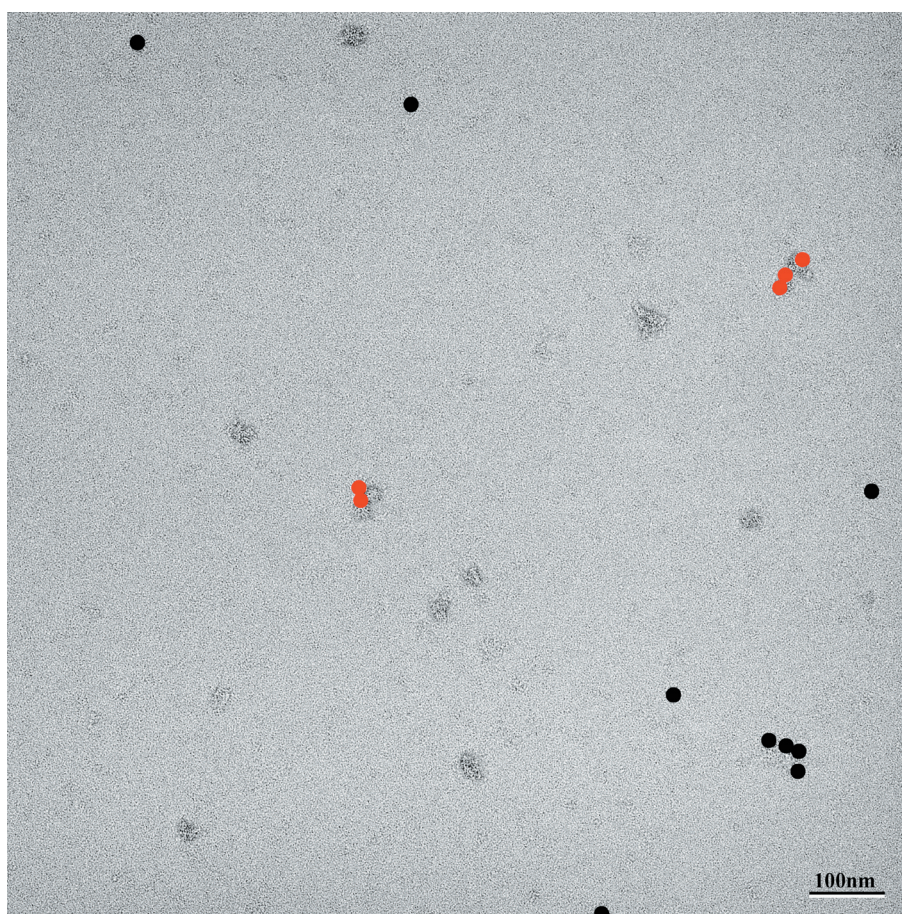


Figure 29. Direct immunogold-labeling in solution. Gold particles, indicating the mAb 5B4 were found associated with nanoparticles (enlarged and pseudocoloured red) but also randomly adsorbed to the grid (enlarged and coloured black).

To get more conclusive results for immunogold labeling of nanoparticles, we pursued several strategies to improve the specificity of this technique.

For direct immunogold labeling of nanoparticles on the EM-grid, NP-L/S and NP were applied to gently glow discharged copper EM-specimens. Subsequently, the specimens were incubated on droplets of serially diluted, gold-coupled mAb 5B4 (5B4-Au) and a gold-coupled unrelated mAb. After careful washing, labeled specimens were processed for CTEM as described in Chapter 1.3.

Incubation with moderate concentrations of 5B4-Au yielded gold particles attached to the nanoparticles and also to the EM-grid. Similar to the direct labeling in solution, actual binding events and background noise could not be distinguished (data not shown).

5B4-Au was further titrated in order to establish conditions where unspecific binding to the grid was minimal. Immunogold labeling of different nanoparticles with 5B4-Au and the gold-conjugated unrelated mAb under these conditions is illustrated in Figure 30. Despite the presence of multiple epitopes per particle, binding events on NP-L/S were rather scarce (Figure 30 A). Moreover, a similar number of binding events was observed with NP that do not carry the loop epitope (Figure 30 B), and even with the unrelated mAb (Figure 30 C), gold particles were associated with NP-L/S.

This finding suggests that the interaction between 5B4-Au with adsorbed NP-L/S is not strong enough to be significant. Alternatively, epitopes on adsorbed NP-L/S are not sufficiently exposed to be accessed by specific antibody. Independent on the amount of antibody applied, we detected at the most six gold particles on individual, assembled nanoparticles. Since NP-L/S have a diameter of less than 30 nm (see Chapter 2.5) and the approximate size of IgGs is 12 nm (Taschner et al. 2001), the number of binding events could have been limited by spatial hindrance of the antibody.

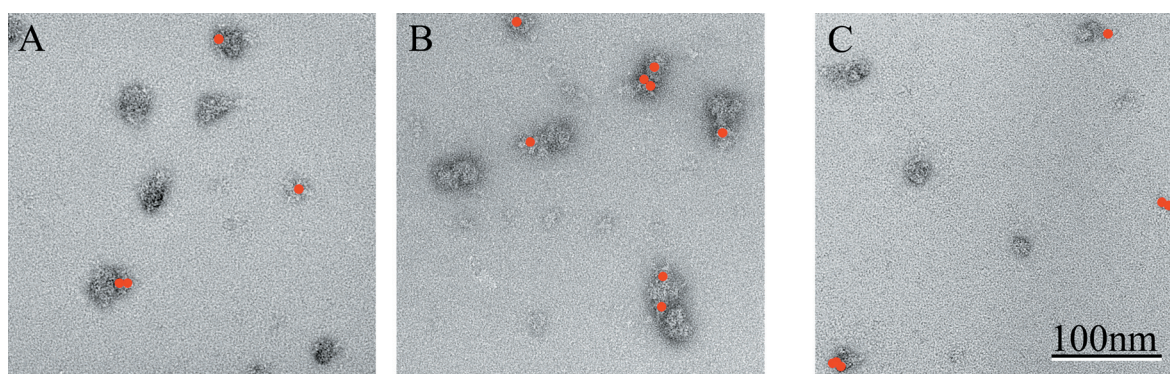


Figure 30. Direct immunogold-labeling of peptidic nanoparticles. (A) NP-L/S labeled with 5nm colloidal gold conjugated 5B4 actin loop mAb (5B4-Au). (B) The same gold-conjugated mAb binds to NP. (C) NP-L/S labeled with 5nm colloidal gold-conjugated unrelated mAb. Gold particles are enlarged and pseudocolored red.

Thus, only a delimited number of antibody-gold complexes were capable to bind to the epitopes on the nanoparticles. This is consistent with the significantly larger number of gold particles detected on aggregated nanoparticles, such as on NP-L/C (data not shown).

Moreover, as displayed in Figure 31, small cluster of gold-labeled antibody have dimensions similar to those of nanoparticles. Hence, in many cases it remained unclear if there was a nanoparticle underneath the gold or if the gold dots represent only aggregates of antibody.

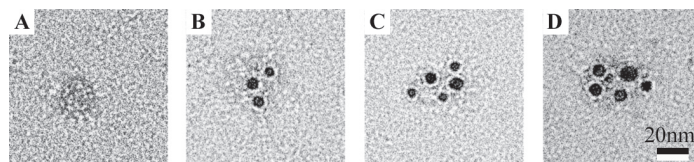


Figure 31. Immunogold-labeling of nanoparticles. In (A) and (B) the structure of the recognized nanoparticle is clearly. However, in (C) and (D) small clusters of gold dots could represent nanoparticles covered by bound antibodies or aggregates of antibodies alone.

In contrast to other labeling strategies, such as indirect immunogold labeling of nanoparticles in solution and on the specimen as well as direct immunogold labeling in solution, direct immunogold labeling of nanoparticles on the specimen was the only technique with which unspecific bound gold particles could be eliminated from the background of the specimen.

In order to achieve a high density of nanoparticles and thereby reduce background noise caused by unspecific adsorption of the antibodies, we also tried immunogold labeling on embedded and thin-sectioned nanoparticles, as was shown for viruses and VLP previously (e.g. (Canto-Nogues et al. 2001; Chiu et al. 2006)). Therefore, we pelleted NP-L/S particles by high-speed centrifugation.

However, the soft nanoparticle pellets easily disintegrated and could not be embedded.

In conclusion, we suggest that immunogold labeling was not an appropriate technique to visualize and verify the specific binding of antibodies with peptide nanoparticles. Due to the small difference in size between nanoparticles and antibodies, the number of specific binding events was too little to distinguish from unspecific binding.

However, immunogold labeling of viruses and virus-like particles (VLPs) is a commonly used technique. In contrast to our nanoparticles, the previously immunogold labeled viruses and VLPs span at least 50 nm and remained visible even with a larger number of gold particles attached (e.g. (Brookman et al. 1995; Berg et al. 2005)). Apart from biochemical and immunofluorescence studies, visualization of specific interactions of antibodies with peptide nanoparticles yielded more convincing results using FCCS (Schroeder et al. manuscript accepted; JMB; Chapter 2.5).

2.7 Conclusions and outlook

As documented in Chapter 2.4, immunization with peptide nanoparticles carrying epitopes that mimic distinct structural elements of the actin molecule yielded antibodies that specifically recognize these particular epitopes *in vitro* and *in situ*.

Currently, we aim at producing antibodies that exclusively recognize the LD. For this purpose, we genetically engineered three novel, designed peptides onto the C-terminus of the core polypeptides. These peptides were designed to mimic surface areas and surface charges that occur at the interface of LD subunits and are specific to the antiparallel arrangement of the subunits. Because the amino acid sequence of the chosen epitopes do not occur in monomeric actin, we suggest that these constructs are suitable to produce antibodies that exclusively react with LD.

Chapter 3

Raver1

**An integral component of muscle contractile elements
and a potential ligand for actin**

3.1 Introduction

3.1.1 Raver1 – a heterogeneous nuclear ribonucleoprotein

By screening a yeast two-hybrid library for new ligands of the actin-binding proteins (ABPs) vinculin/metavinculin, Huettelmaier and coworkers identified a hitherto unknown protein, which they termed raver1 (Huttelmaier et al. 2001). Computational analysis revealed that rat raver1 is composed of 748 amino acids (Mr 80 kDa), which include one Rev-like nuclear export sequence (NES), two nuclear localization signals (NLS), and three amino-terminal RNA recognition motifs (RRMs). Within the RRM, raver1 shares some conserved motifs with proteins of the heterogeneous nuclear ribonucleoprotein (hnRNP) family (Huttelmaier et al. 2001; Jockusch et al. 2003). Thus, in the absence of any other homologues, raver1 is currently considered to be an hnRNP.

3.1.2 Cellular distribution of the dual compartment protein raver1

Raver1 is ubiquitously expressed in all cell lines and tissues tested (Huttelmaier et al. 2001). Striated muscle and organs with a high content of epithelia express the highest levels of raver1, whereas comparatively low amounts are found in brain, lung and spleen tissue (Zieseniss 2005). Expression of raver1 is not restricted to specific developmental stages. Although considered an hnRNP, raver1 is not confined to the nucleus, but is also present in the cytoplasm. Specifically, it is predominantly nuclear in undifferentiated cells and more evenly distributed throughout the nucleus and the cytoplasm after differentiation (Huttelmaier et al. 2001).

The majority of nuclear raver1 is localized in perinucleolar bodies, where it colocalizes with the hnRNP polypyrimidine tract binding protein (PTB), which is involved in RNA splicing of certain actin binding proteins (ABP), such as α -actinin and tropomyosin (Valcarcel and Gebauer 1997). Consistent with an association of raver1 with PTB, native protein complexes containing raver1 and PTB could be isolated from undifferentiated C2C12 myoblasts (Zieseniss 2005). Intriguingly, actin was also a constituent of this complex.

During the differentiation of myoblasts to myotubes, raver1 was seen to redistribute from the nuclear to the cytoplasmic compartment (Huttelmaier et al. 2001), indicating that translocation possibly depends on the differentiation stage and/or the transcriptional activity of cells (Huttelmaier et al. 2001; Zieseniss 2005; Zieseniss et al. 2007). However, studies with C2C12 myoblasts and heterokaryon HeLa cells showed a continuous shuttling of raver1 between the cytoplasm and the nucleus (Huttelmaier et al. 2001).

The localization of cytoplasmic raver1 was intensively studied in isolated myotubes, and in striated as well as smooth muscle tissues (Huttelmaier et al. 2001; Zieseniss 2005; Zieseniss et al. 2007). Immunofluorescence and immunoelectron microscopy revealed a

distinct labeling pattern of raver1 in the cytoplasm, which was similar in myotubes and different striated muscle tissues. In myotubes, raver1 colocalized with vinculin/metavinculin and α -actinin at microfilament attachment sites (Huttelmaier et al. 2001). Likewise, raver1 was abundant at the microfilament attachment sites in sarcomers and costamers of skeletal muscle tissues (Zieseniss 2005; Zieseniss et al. 2007). However, in heart tissue raver1 was predominantly detected at intercalated discs (Huttelmaier et al. 2001), but also at the I-bands (Zieseniss 2005; Zieseniss et al. 2007).

In Chapter 3.3, the detailed localization of raver1 in different types of muscle tissue revealed by immunofluorescence and immunoelectron microscopic analyses is presented. In the following Chapter 3.4, this published study was extended to immunolabeling of raver1 in different cultured cell lines and in nuclei from *Xenopus laevis* oocytes.

3.1.3 Raver1 - a potential ligand for actin

Despite a distinct distribution of raver1 in cells and tissues, and biochemical evidence for its interaction with specific ABPs and PTB, the function of raver1 remains unknown. Interestingly, a number of findings suggest that actin might be a possible target protein for raver1. For instance, raver1 accumulates at the I-band of sarcomers where F-actin filaments are the predominant structure. In addition, both proteins have some binding partners in common. Consistent with the notion of a direct interaction of raver1 and actin in the nucleus, preliminary data suggest that both proteins are constituents of the same nuclear complex.

Actin has been shown to play a role in the nuclear export of retroviral RNAs but also of host proteins such as protein kinase inhibitor (Hofmann et al. 2001; Hofmann et al. 2006). Similarly, raver1 has been suggested to be involved in the translocation machinery that escort proteins to their specific microfilament adhesion sites into the cytoplasm (Huttelmaier et al. 2001; Jockusch et al. 2003).

Another common feature of raver1 and actin is their involvement in the readout of genetic information. Nuclear actin has been recently identified as a component of the transcription apparatus (reviewed by (Grummt 2006)), which implies an important role of actin in RNA processing, whereas raver1 through its interaction with PTB, is involved in mRNA stability. Genes whose alternative splicing is regulated by PTB include α -tropomyosin (TM), β -TM and α -actinin, which are binding partners of actin in the sarcomere (reviewed in (Wagner and Garcia-Blanco 2001)).

Preliminary evidence for a direct interaction of raver1 and actin *in vitro* has recently been provided (Zieseniss 2005). For a more detailed analysis, we carried out cosedimentation assays with purified rabbit skeletal muscle actin and recombinantly expressed raver1. The results of the biochemical and microscopic analysis of the protein complexes are summarized Chapter 3.4.

3.2 Material and methods

Most of the methods applied will be included in the publication in Chapter 3.3.

Preparation of *Xenopus laevis* oocyte nuclei

Mature (stage VI) oocytes were surgically removed from female *X. laevis* (Jarnik and Aebi 1991) and kept in modified Barth saline (10 mM HEPES containing 88 mM NaCl, 1 mM KCl, 0.82 mM MgSO₄, 0.33 mM Ca(NO₃)₂, 0.41 mM CaCl₂, 100 U/ml penicillin-streptomycin, pH 7.5; MBS) at 4°C. Oocytes were defolliculated by treatment with 5 mg/ml collagenase (Sigma, St. Louis, MO) in calcium-free MBS for 3 hrs at RT.

For CTEM, nuclei were manually dissected from stage VI oocytes and collected in low salt buffer (10 mM HEPES containing 1 mM KCl, 0.5 mM MgCl₂, pH 7.5; LSB), fixed for 15 min in LSB containing 4% formaldehyde, and then processed for thin-section electron microscopy as described elsewhere (Fahrenkrog et al. 2002; Paulillo et al. 2005).

Cosedimentation of raver1 and actin

Purified skeletal muscle G-actin (see Chapter 1.3) and recombinant full-length raver1 protein (R1-FL) and a carboxy-terminal raver1 fragment (R1-ΔN), which were expressed in insect cells, were precleared from aggregates by ultracentrifugation at 100.000 g for 1 hr at 4°C. The upper fraction of the corresponding supernatants was removed and the protein content was determined by measuring UV absorption.

For cosedimentation, G-actin and raver1 fragments were mixed at final concentrations of 3 μM and 2 μM, respectively, and incubated on a roller for 1 hr at 4°C. Subsequently, high-speed pelleting and SDS-PAGE analysis were performed as described in Chapter 1.3. The SDS-PAGE gels were silver stained as published (Ansorge 1985).

For cosedimentation of prepolymerized F-actin filaments and R1-FL or R1-ΔN, G-actin was first polymerized in the presence of 100 mM KCl and a two-fold molar excess of phalloidin over F-actin. The resulting filaments were separated from non-polymerized actin by high-speed pelleting according to Chapter 1.3. The pellets were resuspended in actin filament buffer and used for cosedimentation assays with R1-FL or R1-ΔN. The experimental conditions were similar to those described for cosedimentation with G-actin, except that actin filament buffer was used for washing and resuspension of the filament pellets.

Chapter 3.3

Raver1 is an integral component of muscle contractile elements

Anke Zieseniss^{1,4}, Ulrich Schroeder², Sabine Buchmeier¹, Cora Ann Schoenenberger², Joop van den Heuvel³, Brigitte M. Jockusch¹ and Susanne Illenberger^{1*}

¹ Cell Biology Group, Zoological Institute, TU Braunschweig, D-38092 Braunschweig, Germany

² Maurice E. Mueller Institute for Structural Biology, Biozentrum, University of Basel, CH-4056 Basel, Switzerland

³ Division of Structural Biology, German Research Centre for Biotechnology, D-38124 Braunschweig, Germany

⁴ Department of Cell Biology and Anatomy, The University of Arizona, Tucson, AZ 85724 USA

Key words: hnRNP, striated muscle, smooth muscle, sarcomere, myofibril

Corresponding author: Susanne Illenberger
Cell Biology, Zoological Institute
Technical University of Braunschweig
Biocentre, Spielmannstr. 7
D-38092 Braunschweig

Tel. (+) 49 531 391 3191; Fax (+) 49 531 391 8203

Email: S.Illenberger@tu-bs.de

Abstract

Raver1, a ubiquitously expressed protein was originally identified as a ligand for metavinculin, the muscle specific isoform of the microfilament-associated protein vinculin. The protein resides primarily in the nucleus, where it colocalizes and may interact with the polypyrimidine-tract binding protein PTB, which is involved in alternative splicing processes. During skeletal muscle differentiation, raver1 translocates to the cytoplasm and eventually targets to the Z-line of sarcomeres. Here, it colocalizes with metavinculin, vinculin and alpha-actinin, all of which have biochemically been identified as raver1 ligands. To obtain more information on the potential role of raver1 in muscle structure and function, we investigated its distribution and fine localization in striated and smooth muscle of mouse. Three monoclonal antibodies that recognize epitopes in different regions of the raver1 protein were employed in immunofluorescence and immunoelectron microscopy. Our results show that cytoplasmic accumulation of raver1 is not confined to skeletal muscle, but occurs also in heart and smooth muscle. Unlike vinculin and metavinculin, cytoplasmic raver1 is not restricted to costameres, but also represents an integral part of the sarcomere. In isolated myofibrils and in ultrathin sections of skeletal muscle, raver1 was found concentrated at the I-Z-I band. In addition, a minor fraction of raver1 was present in the nuclei of all three types of muscle. These data indicate that during muscle differentiation raver1 might link gene expression with structural functions of the contractile machinery of muscle.

Introduction

Muscle contraction critically depends on the precise interplay of myofibrils anchored to and associated with structural as well as regulatory proteins. This is best demonstrated for striated muscle, where the contractile apparatus is organized into regular repeating units, the sarcomeres, whose integrity is essential for proper muscle function. Metabolic labeling and transfection studies have shown that fully differentiated muscle, in spite of its rigid appearance, is a highly dynamic structure with a constant turnover of individual components albeit at different rates (Zak et al. 1977; Martin 1981; Michele et al. 1999; Littlefield et al. 2001). Even proteins previously perceived as static components of the Z-disc such as alpha-actinin or myotilin are in a continuous exchange with a cytoplasmic pool (Wang et al. 2005). Furthermore, muscle is able to respond to changes in mechanical strain by altering the equilibrium between protein synthesis and degradation (Janmey 1998; Ruwhof and van der Laarse 2000; Russell et al. 2000). However, it is still poorly understood how the turnover of individual components is achieved while muscle function is being maintained.

Some of the muscle proteins exhibit a dual residency, at the sarcomere and in the nucleus. They have been suggested to function as messengers that link gene expression to myofibril signalling pathways. Indeed, there is increasing evidence that sarcomeric constituents may appear at different subcellular locations in response to different stimuli, both within the

sarcomere as well as in other cellular compartments, such as the nucleus (reviewed in (Clark et al. 2002; Lange et al. 2006)). These findings imply that the sarcomere not only provides the structural basis for muscle contraction, but also serves as a communicative platform where signals are both, perceived and transmitted, allowing for functional plasticity of muscle tissue.

A candidate messenger protein in muscle differentiation or maintenance is raver1 (Figure 32 A), a ubiquitously expressed 80 kDa protein that contains three RNA-recognition motifs (RRMs) with a high sequence homology to members of heterogeneous ribonucleoprotein family (Huttelmaier et al. 2001; Jockusch et al. 2003). In most cell types, raver1 is found in the nucleus, but displays nucleocytoplasmic shuttling presumably mediated by two nuclear localization signals at the N- and C-termini and a putative export sequence located within the central leucine-rich region. In the nucleus, raver1 may associate with another hnRNP, the polypyrimidine tract binding protein (PTB), a potent regulator of alternative splicing of several genes (Valcarcel and Gebauer 1997). Direct binding of raver1 to PTB has been demonstrated *in vitro* and both proteins colocalize in the perinucleolar compartment (PNC), an RNA-dependent structure that is characterized by the accumulation of PTB (Ghetti et al. 1992). Furthermore, raver1-PTB complexes can be immunoprecipitated from vertebrate cells (Huttelmaier et al. 2001). While direct RNA binding of raver1 has yet to be demonstrated, the protein may assist in PTB-mediated splicing events in smooth muscle (Gromak et al. 2003; Spellman et al. 2005). Apart from its association with PTB in the nucleus, raver1 interacts with the microfilament-associated proteins vinculin, its muscle-specific splice variant metavinculin and alpha-actinin (Huttelmaier et al. 2001). In fact, raver1 was originally identified through its interaction with metavinculin in a yeast two hybrid screen. During myotube formation of C2C12 cells, nuclear raver1 was shown to translocate to the cytoplasm and eventually associate with myofibrils at the position of the Z-line. In differentiated skeletal muscle, raver1 colocalized with its cytoplasmic ligands (meta)vinculin and alpha-actinin at the region of sarcomeric Z-lines and costameres (Huttelmaier et al. 2001).

To gain further information on raver1 and its role in muscle differentiation, we embarked on a detailed analysis of the localization of raver1 in skeletal, heart and smooth muscle of the mouse. To this end, we generated and characterized three monoclonal antibodies against different regions of the raver1 protein and employed them in immunofluorescence and immunoelectron microscopy. Our data reveal that raver1 is associated with cytoplasmic contractile elements in all three muscle types. Furthermore, raver1 is not restricted to costameres, but the protein is a prominent component of the I-Z-I region in striated muscle and the intercalated disc in heart. In addition, nuclear localization of raver1 was noted for all tissues examined.

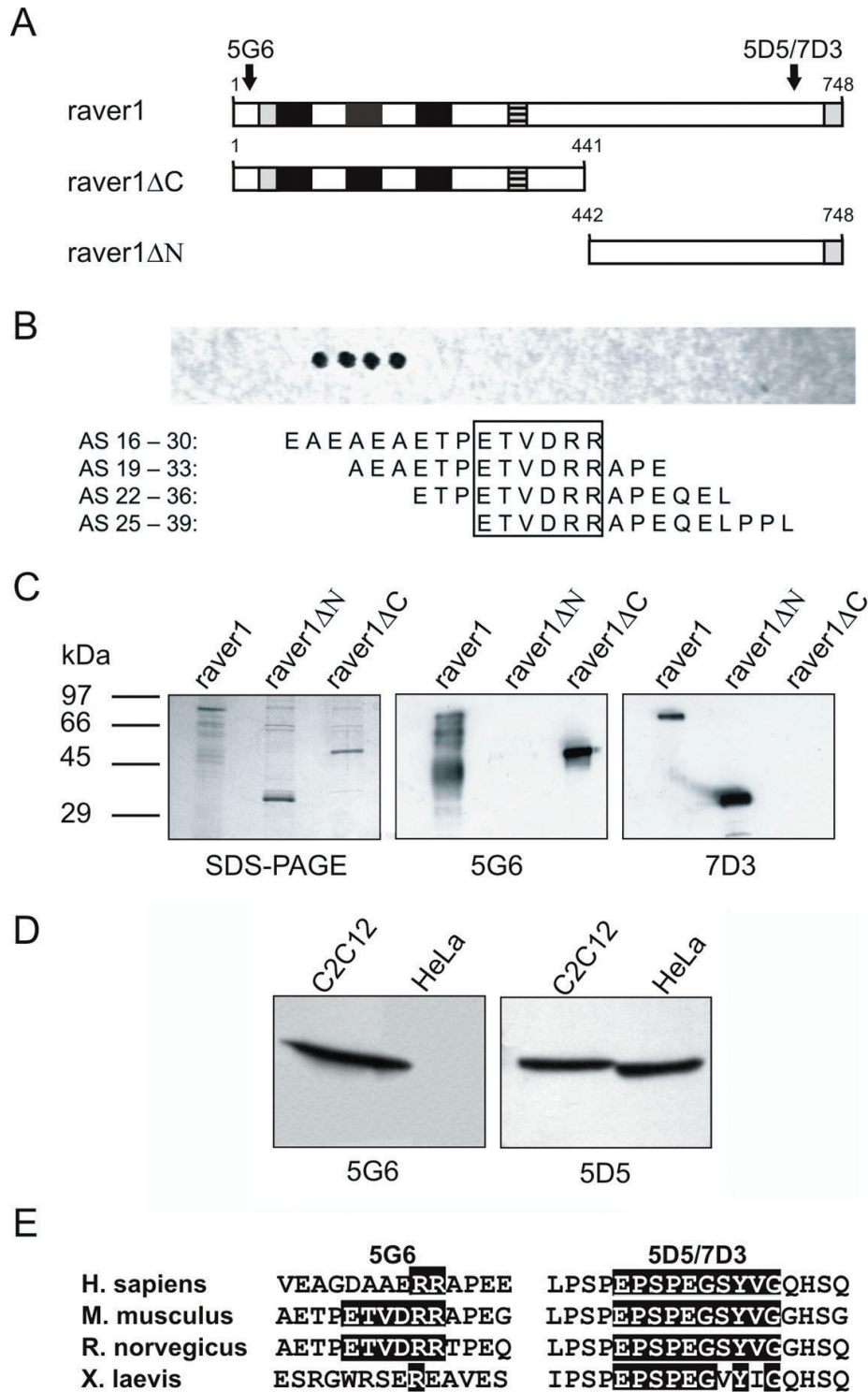


Figure 32. Characterization of monoclonal antibodies against different raver1 epitopes. (A) Schematic representations of full-length raver1 and two complementary deletion constructs used in this study. The first and last amino acids of each construct are given. RNA recognition motifs are shown as black boxes, nuclear localization signals are indicated in grey. A central leucine-rich region (putative NES) is depicted as a hatched box. Arrows indicate the binding positions of the monoclonal antibodies 5G6, 5D5 and 7D3. (B) The epitope recognized by 5G6 comprises amino acids 25 - 30 of raver1 as revealed by pepscan analysis. (C) Reactivity of the raver1 antibodies with recombinant raver1 and its deletion fragments (SDS-PAGE, left panel) in immunoblots.

5G6 (centre panel) recognizes full-length *raver1*, a bouquet of its degradation products and *raver1* Δ C, while 7D3 (right panel) and 5D5 (not shown) react with full length *raver1* and *raver1* Δ N. (D) Reactivity of the *raver1* antibodies with cell extracts. Equal amounts of proteins from murine C2C12 and human HeLa were subjected to SDS-PAGE, blotted and incubated with 5G6 (left), 5D5 (right) and 7D3 (not shown). While the C-terminal antibodies recognize *raver1* protein in samples of both cell types, 5G6 detects only murine *raver1*. (E) Part of the amino acid sequence of *raver1* comprising the epitopes for 5G6 (left) and 7D3/5D5 (right) from different species. Note that the C-terminal sequence is highly conserved among vertebrate *raver1* proteins, whereas the 5G6 epitope is only conserved in mouse and rat.

Materials and methods

Raver1 antibodies

Three monoclonal antibodies of the IgG type were generated. The antibody 5G6 was raised against an N-terminal fragment of *raver1* (Huttelmaier et al. 2001). In the present study, the epitope of this antibody was mapped by pepscan analysis. Peptides (15mers) of the *raver1* sequence with an overlap of twelve amino acids between consecutive peptides were spot-synthesized on a cellulose membrane (Frank and Overwin 1996) and analyzed for antibody binding as described (Mayboroda et al. 1997). Two additional antibodies (5D5 and 7D3) were raised against a C-terminal peptide (EPSPEGSY, corresponding to amino acids 718 - 727) of the protein, following standard protocols. The antibodies obtained were tested in solid phase binding assays (enzyme-linked immunosorbent assay) on recombinant protein and in immunoblots using total extracts of HeLa and C2C12 cells subjected to SDS-PAGE. HRP-coupled goat anti-mouse antibodies (Sigma) were used as secondary antibodies in both assays.

The *raver1* antibodies were purified from hybridoma culture supernatants by affinity chromatography using anti-mouse IgG agarose (Sigma) columns. Binding and elution of antibodies was performed according to the supplier's protocol. 500 μ l fractions were collected and immediately neutralized to pH 7.0 with 1 M Tris pH 9.5. Aliquots were analyzed by SDS-PAGE. Fractions containing high antibody concentrations were pooled and dialyzed against PBS overnight. The concentration of purified antibody was calculated from the absorption at OD280 nm using an extinction coefficient of 1.35.

Cryosectioning and immunofluorescence labeling

Freshly isolated murine tissues (extensor digitorum longus, heart, uterus, urinary bladder) were mounted on egg white and cork (Jockusch and Voigt 2003) with Polyfreeze tissue-freezing medium (Polysciences Inc.). To prevent contraction, muscles were fixed with

minutien pins. Specimens were frozen in melting isopentane, prechilled in liquid nitrogen and stored at -80°C . They were sectioned (5 - 10 μm) in a cryostat microtome at -20°C , mounted on glass slides and dried for at least 30 min. After washing with PBS, the sections were briefly (10 - 20 s) incubated with 1% Triton X-100 and then fixed with 4% formaldehyde for 20 min. After additional washing steps, they were permeabilised with 0.2% Triton X-100 at room temperature (RT) for 30 min. For indirect immunofluorescence, unspecific background labeling was first quenched by incubation with 5% bovine serum albumin and 0.25 mg/ml Fab fragments (goat anti-mouse IgG, Dianova) in PBS at RT for 1 hr. The sections were then washed in PBS and incubated with the monoclonal raver1 antibodies (cell culture supernatants) at RT for 1 hr, washed three times in PBS and then incubated with goat anti-mouse Cy3 (diluted 1:200, Jackson Immuno Research). Samples were counterstained for F-actin and DNA with FITC-conjugated phalloidin (Sigma) and DAPI, respectively. Finally, samples were extensively washed in PBS, mounted in Mowiol, and examined with a Zeiss Axiophot microscope equipped with epifluorescence optics.

Preparation and staining of myofibrils

Skeletal muscles were dissected from adult mice and incubated in Ringer's solution (100 mM NaCl, 2 mM MgCl_2 , 5 mM EGTA, 10 mM NaH_2PO_4 , 0.1% glucose, 20 μM leupeptin, pH 7.4) on ice for 30 min. The tissue was transferred to rigor buffer (100 mM KCl, 2 mM MgCl_2 , 2 mM EGTA, 0.3 mM DTT, 20 μM leupeptin pH 7) using 5 ml per 0.5 g of tissue. After homogenisation using a dounce homogeniser, samples were incubated for 10 min on ice under constant agitation, centrifuged at 1.500 g for 30 min and resuspended in 10 volumes of ice-cold rigor buffer. These steps were repeated three times. Isolated myofibrils were stored in rigor buffer containing 50% glycerol at -20°C until use. For immunofluorescence, the myofibrils were allowed to adhere to glass slides for 1 min, rinsed with PBS and fixed with 4% formaldehyde for 10 min. After washing the samples were blocked with 5% bovine serum albumin in PBS at RT for 2 hrs, to reduce background labeling and stained for immunofluorescence as described above. Sarcomeric alpha-actinin was stained using a monoclonal antibody (Sigma).

Immunoelectron microscopy

For immunogold labeling, ultrathin sections were mounted on 200 mesh carbon/parlodion-coated copper grids. After blocking unspecific binding sites by two 5 min incubations in 2% BSA/PBS, grids were incubated on droplets of raver1 antibody solutions in a moist chamber at RT for 2 hrs. The optimal antibody concentrations were determined by titration experiments. For direct labeling, purified raver1 antibodies were conjugated to colloidal gold (Slot and Geuze 1985). For indirect labeling, grids were rinsed with PBS after primary

antibody incubation, blocked with 2% BSA in PBS for two times 5 min, and then incubated with a secondary 10 nm gold-conjugated goat anti mouse IgG (BBInternational) for 1 hr at RT. After washing in PBS and dH₂O, grids were stained with 6% uranyl acetate for 1 hr, rinsed with dH₂O and then counterstained with lead-citrate for 2 min. For control experiments the primary antibody was omitted (data not shown). Electronmicrographs of stained specimens were recorded with either a Hitachi H 7000 (Hitachi Ltd., Tokyo, Japan) on Kodak® electron image film SO-163 or digitally with a Philips Morgagni 268D (Philips Electron Optics BV, Eindhoven, Netherlands) transmission electron microscope operated at an acceleration voltage of 100 kV and 80 kV, respectively.

Gel electrophoresis and immunoblotting

Total protein extracts from C2C12 and HeLa cells were obtained as described (Huttelmaier et al. 2001). Equal amounts of total protein were loaded onto 10% polyacrylamide gels. After electrophoresis, samples were transferred onto nitrocellulose membranes and analyzed for raver1 proteins following standard procedures as described (Huttelmaier et al. 2001).

Recombinant protein expression and purification

Recombinant raver1 proteins were expressed using the Bac-to-Bac™-system according to the manufacturer's (Invitrogen) protocol. Briefly, cDNAs encoding full-length raver1, raver1 Δ C (amino acids 1 - 441) and raver1 Δ N (amino acids 442 - 748) were cloned into a modified pFastBac™ donor plasmid harbouring an additional FLAG tag sequence downstream of the histidine tag and transformed into E.coli DH10Bac cells. Recombinant bacmid DNA was isolated and transfected into sf9 (*Spodoptera frugiperda*) cells. The virus-containing supernatant was harvested and used for the infection of High Five™ insect cells. Cells were collected by centrifugation at 500 g for 5 min, washed with PBS containing leupeptin (20 μ M) and stored at -70°C. His-tagged proteins were purified from insect cells according to the manufacturer's instructions (Qiagen) with slight modifications as described (Witt et al. 2004). Fractions containing the protein of interest were dialyzed against storage buffer (50 mM sodium phosphate buffer, pH 7.2, containing 0.2 mM EGTA, 4 μ M pepstatin A, 40 μ M leupeptin, Trasylol® (2.8 mg/ml in H₂O) and 14.3 mM β -mercaptoethanol) and stored on ice until use.

Results

Characterization of raver1 antibodies

In the present study three monoclonal antibodies, directed against different regions in the raver1 sequence (Figure 32 A) were employed to analyze the subcellular distribution of raver1 protein in muscle. The 5G6 antibody was raised against a recombinant MBP-tagged N-terminal raver1 fragment (amino acids 1 - 625) for the initial characterization of raver1 (Huttelmaier et al. 2001). We mapped the epitope of this antibody by pepscan analysis (Frank and Overwin 1996) and found that it recognizes a series of four 15mer peptides (Figure 32 B). From the minimal sequence overlap the epitope ETVDRR was deduced, which corresponds to amino acids 25 - 30 of raver1. The antibodies 5D5 and 7D3 were raised against a C-terminal synthetic peptide (EPSPEGSY, comprising amino acids 718 - 727) and specifically recognized this peptide in ELISA and immunoblot assays (data not shown).

All three antibodies were tested for their reactivity with recombinant raver1 proteins in immunoblot assays (Figure 32 C and data not shown). Full-length raver1 and the two complementary deletion constructs raver1 Δ C (amino acids 1 - 441) and raver1 Δ N (amino acids 442 - 748) were purified from insect cells and subjected to SDS-PAGE (left panel), revealing major protein bands of 80 kDa for full-length raver1, approximately 51 kDa for raver1 Δ C and approximately 35 kDa for raver1 Δ N. Degradation was only noted for the full-length protein. In immunoblots, antibody 5G6 recognized full-length raver1 and its proteolytic fragments as well as the N-terminal fragment raver1 Δ C (Figure 32 C, middle). In contrast, antibodies 5D5 and 7D3 bound to the C-terminal construct raver1 Δ N in addition to the full-length protein, but failed to detect any degradation products (Figure 32 C, right and data not shown). This indicates that the full-length protein is degraded from its C-terminus.

When tested on cell extracts (Figure 32 D), all three antibodies recognized a protein band of approximately 80 kDa in murine C2C12 cells. In (human) HeLa cells, however, endogenous raver1 protein was only detected by the C-terminal antibodies (Figure 32 D, right and data not shown). Consistent with this finding, a comparison of known raver1 sequences reveals that the 5G6 epitope is not highly conserved among vertebrate species, whereas the epitope recognized by 5D5 and 7D3 is present in man, mouse, rat and *Xenopus* raver1 (Figure 32 E).

Identification of raver1 as a myofibril component

In striated muscle, the raver1 ligand vinculin is restricted to attachment sites of the contractile apparatus to the sarcolemma, such as costameres and intercalated disks (Tokuyasu et al. 1981; Koteliensky and Gneushev 1983; Pardo et al. 1983; Witt et al. 2004), whereas alpha-actinin, another raver1 binding partner, is additionally present in the Z-disc (Tokuyasu et al. 1981; McKenna et al. 1986).

We therefore wanted to determine whether raver1 was confined to the costamere or constitutes an integral part of sarcomeric structures. Frozen longitudinal sections of skeletal muscle from adult mice (*extensor digitorum longus*) yielded an identical staining pattern with all three raver1 antibodies (Figure 33 and data not shown). Raver1 was present as a doublet in the I-Z-I region, which was identified in the corresponding phase contrast image. Notably, these doublets could only be seen in well relaxed or stretched muscle. In contracted muscle, raver1 appeared as a single band colocalizing with the Z-line, which may account for the staining observed in our previous investigation (Huttelmaier et al. 2001).

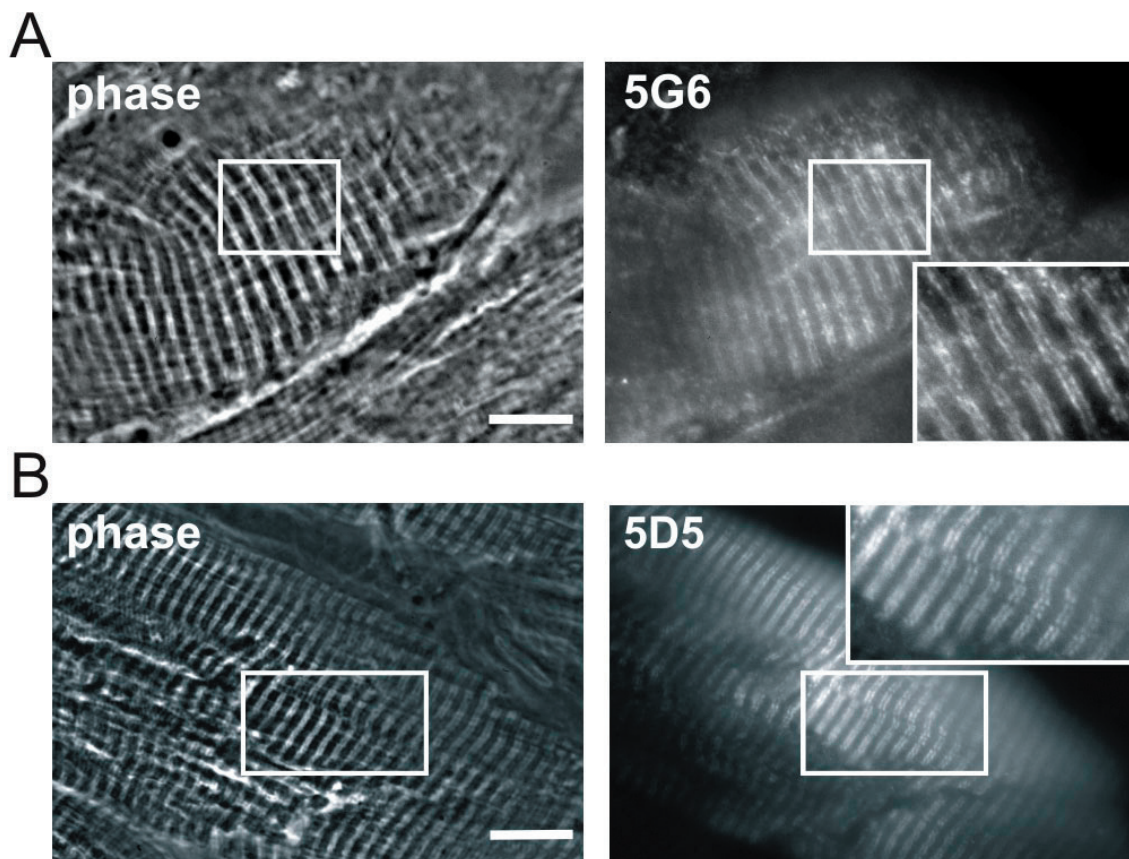


Figure 33. Localization of raver1 in skeletal muscle of the mouse (*extensor digitorum longus*). Immunofluorescence analysis of frozen sections (A, B left panels) stained for raver1 with 5G6 (A) 5D5 (B) and 7D3 (not shown) revealed a striated pattern for each antibody. Higher magnifications (insets) of well stretched muscle tissue (boxed regions) suggest that raver1 is localized as a doublet embracing the Z-lines. Bars, 10 μ m.

To further ascertain the localization of raver1 in muscle, myofibrils were isolated from murine skeletal muscle and labelled with raver1 antibodies yielding identical staining pattern (Figure 34 A and data not shown).

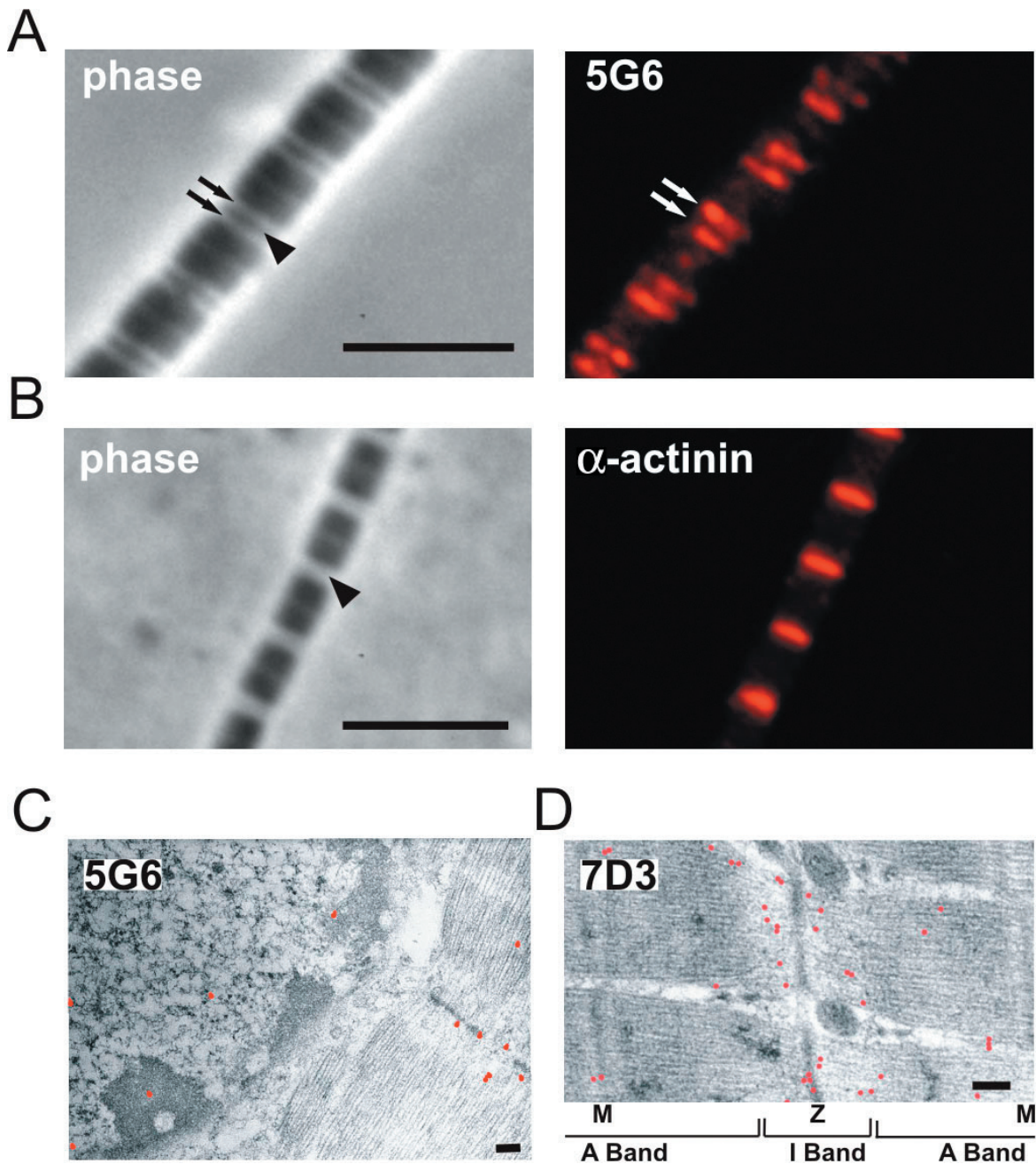


Figure 34. Identification of raver1 as an integral component of skeletal muscle myofibrils. In phase contrast images of myofibrils isolated from mouse skeletal muscle (A and B, left panels), I-bands (arrows) and Z-lines (arrowheads) are well discernible. Immunostaining of myofibrils for raver1 (5G6, A) and alpha-actinin (B) reveals that raver1 concentrates as a doublet in the I-Z-I region whereas alpha-actinin clearly marks the Z-line. Bars, 5 μ m. (C, D). Electron micrographs of ultrathin sections of mouse skeletal muscle directly labelled with 10 nm gold-conjugated raver1 antibody 5G6 (C) and 7D3 (D) show prominent labelling of the I-band with some accumulation in the vicinity of the Z-line. Fewer gold particles are also found at the M-band (M in D) and within the nucleus (C). In both pictures, gold is enlarged and pseudocoloured red. Bars, 200 nm.

Again, raver1 was present as a doublet flanking the Z-disc on both sides as was evident from comparison with the corresponding phase contrast images (Figure 34, left) and the staining of myofibrils for alpha-actinin (Figure 34 B) or actin (data not shown).

The sarcomeric localization of raver1 was further examined by immunoelectron microscopy (Figures 34 C and D). Gold particles were mainly distributed along the Z-disc in the I-Z-I region, but were occasionally also found at the M-line (Figure 34 D). Additionally, sections including the nucleus revealed raver1 also as an intranuclear component (Figure 34 C).

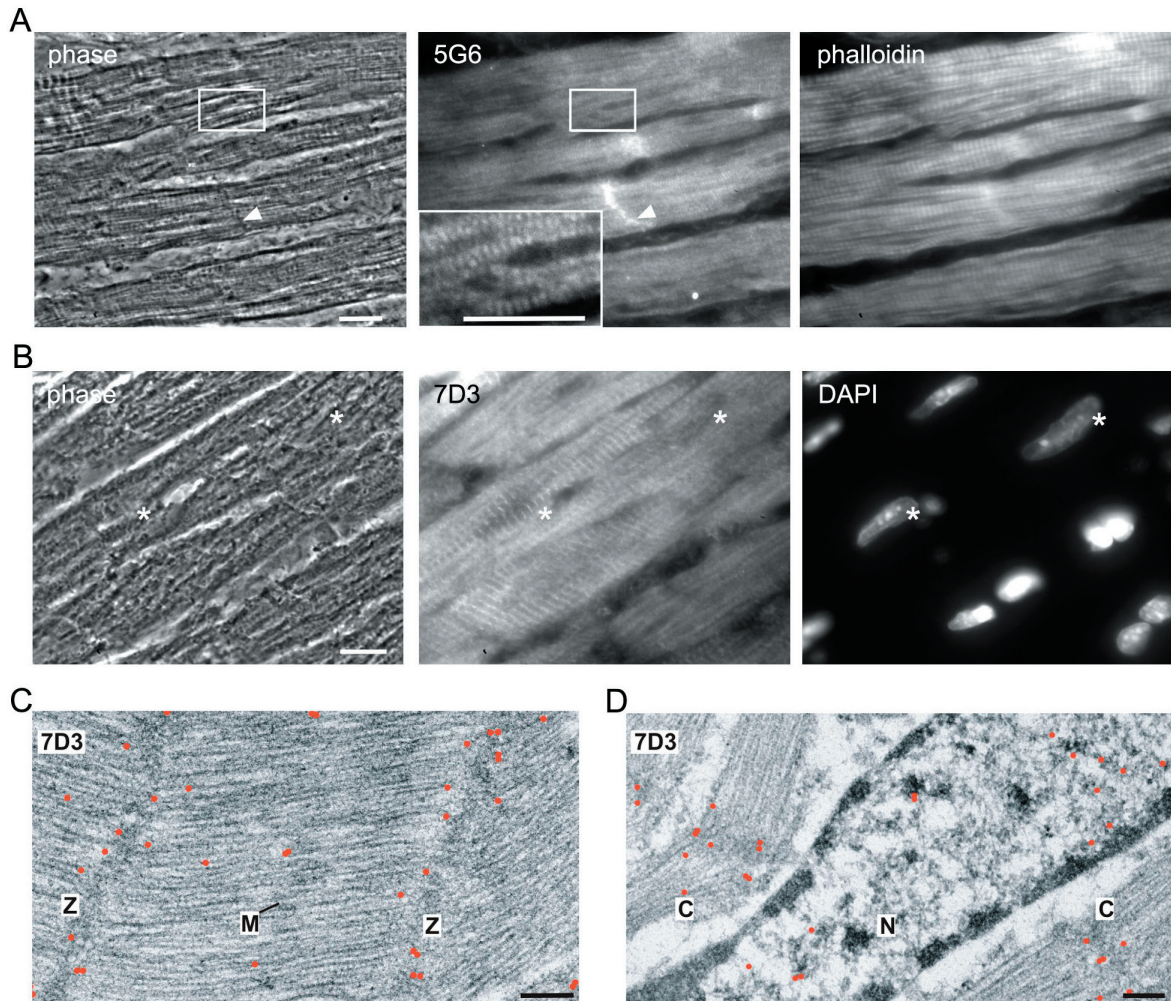


Figure 35. Subcellular localization of raver1 in cardiomyocytes. Frozen longitudinal sections (A, B) of mouse heart muscle were analysed for raver1 by 5G6 (A) and 7D3 (B) and counterstained with either FITC-conjugated phalloidin (A) or DAPI (B) to visualize the filamentous actin cytoskeleton or nuclei, respectively. Left panels (A, B) represent the corresponding phase contrast images. (A, B centre panel): Raver1 is present in a striated pattern in cardiac sarcomeres (inset in A represents a higher magnification of the boxed area) and in intercalated discs (arrowheads in A). A comparably weak raver1 signal which is mainly obscured by sarcomeric striations is detected in the centrally located nuclei of cardiac cells (asterisks in B, placed immediately right to nuclei) which were counterstained by DAPI (right panel). Bars: 10 μ m. (C, D) Ultrathin sections of neonatal rat heart muscle, indirectly labelled with 7D3 and 10 nm gold (enlarged and pseudocoloured red). The sarcomeric (C, D) and nuclear (D) localization of raver1 seen at the light microscopic level is confirmed. M: M-band, N: nucleus, Z: Z-line, Bars, 200 nm.

Localization of raver1 in cardiac muscle

To study the distribution of raver1 in cardiac muscle, immunolabelling experiments were performed on murine ventricular heart tissue (Figure 35). Frozen sections were stained with 5G6 (Figures 35 A) and 7D3 (Figure 35 B). In longitudinal sections, a distinct sarcomeric banding pattern was observed that colocalized with the Z-discs of cardiomyocytes (Figure 35 A). Distinct doublets were not as well resolved as in skeletal muscle (compare inset in Figure 35 A with Figure 33). In addition, a strong raver1 signal was also present at the intercalated discs connecting cardiomyocytes (arrowheads in Figure 35 A). Raver1 staining in cardiomyocyte nuclei was weak (asterisks in Figure 35 B) and often obscured by the sarcomeric signals. A similar reduction of nuclear signal intensity has already been described during the differentiation process of skeletal muscle (Huttelmaier et al. 2001). Ultrastructural analyses by immunoelectron microscopy with 7D3 confirmed the dual residency of raver1 (Figures 35 C, D). Immunogold labelling was prominent at the I-Z-I region (Figure 35 C) and in the nucleus (Figure 35 D). These data reveal that the localization of raver1 at the sarcomeric boundary and in the nucleus is a common feature of striated muscle.

Analysis of raver1 distribution in smooth muscle

We also investigated the subcellular distribution of raver1 in smooth muscle, where the contractile apparatus is not organized in sarcomeres. Sections of murine urinary bladder (Figure 36 A) and uterus (Figure 36 B) were analyzed with 7D3 or 5D5, respectively. The smooth muscle cells of the urinary bladder (Figure 36 A, top left) were readily distinguished from adjacent connective tissue by strong cytoplasmic staining for raver1 (Figure 36, top right), and by the bright staining of filamentous actin by phalloidin (Figure 36, bottom left). A comparison of these images with DAPI staining (Figure 36, bottom right) clearly showed that raver1 was also present smooth muscle nuclei (Figure 36, A arrows). Increased raver1 staining was also noted for the smooth muscle layer of blood vessels (Figure 36 A, boxed areas). Sections of the uterine smooth muscle (Figure 36 B, top left) confirmed the presence of raver1 in myofibrils (Figure 36 B, top right), which were identified by phalloidin staining (Figure 36 B, bottom left) and the characteristic elongated shape of their nuclei (Figure 36 B, bottom right). The presence of raver1 in smooth muscle myofibrils was evident (see Figure 36 B), but the resolution of the immunofluorescence images was not good enough to claim unambiguously its presence in smooth muscle nuclei.

At the ultrastructural level, the distribution of raver1 was examined in ultrathin sections of urinary bladder labelled with 5D5 (Figure 37). Indirect immunogold labelling revealed that raver1 was present in both, nuclei and cytoplasm. In some instances, an association of raver1 with cytoplasmic filamentous structures that could represent microfilaments was observed.

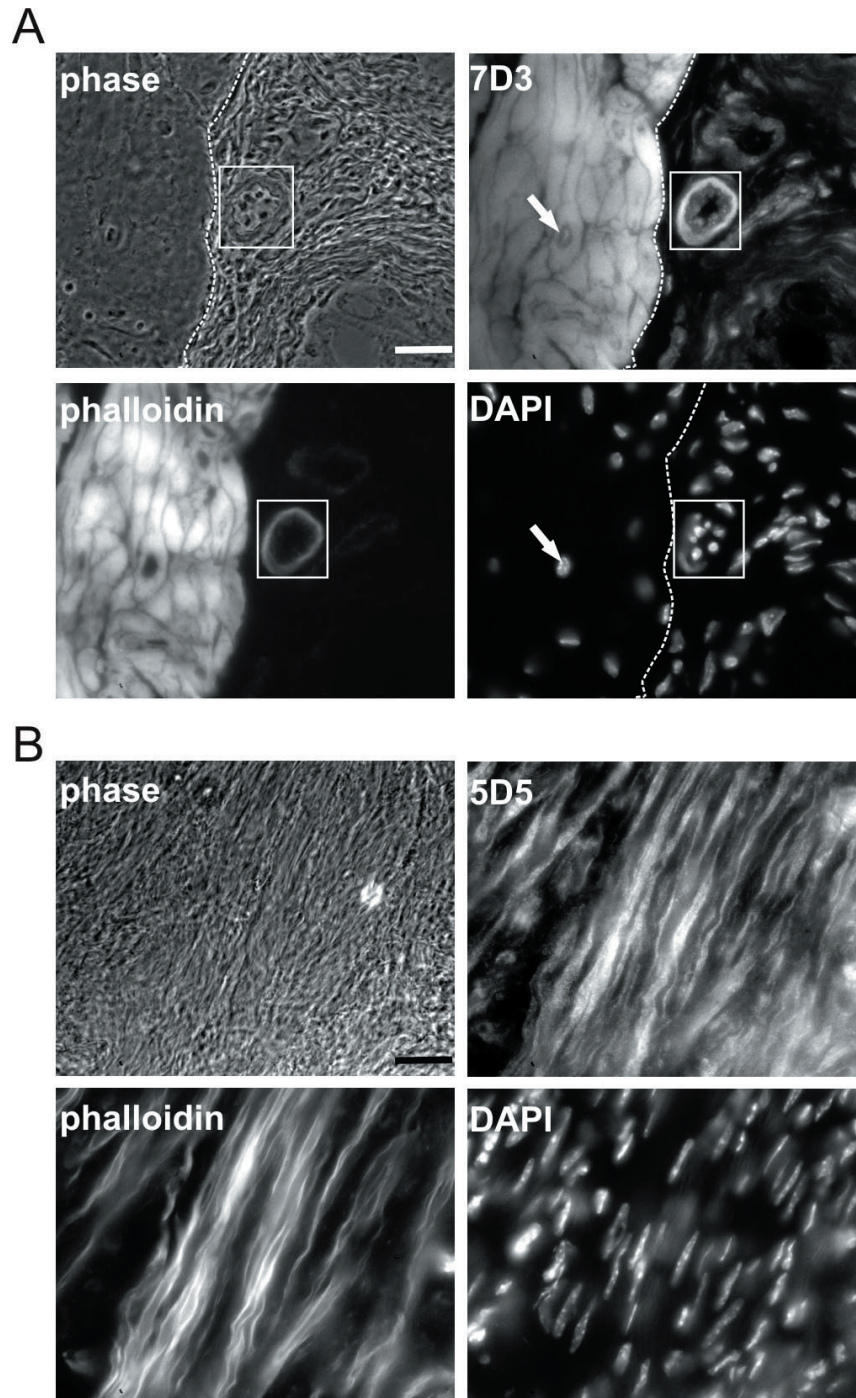


Figure 36. Immunolocalization of raver1 in smooth muscle. (A) Urinary bladder. The phase contrast image (upper left) shows smooth muscle (left), identified by the intense staining of filamentous actin by phalloidin (left lower panel) and connective tissue (right), separated by the dotted line. The position of a blood vessel is indicated (boxed area). Immunostaining with 7D3 (upper right) reveals a cytoplasmic concentration of raver1 in the smooth muscle layers of the urinary bladder and the blood vessel. Less prominent raver1 staining was observed in smooth muscle nuclei (arrows) identified by DAPI staining (lower right). Cells of the connective tissue show primarily a nuclear localization of raver1. (B) Mouse uterus. The smooth muscle fibres seen in the phase contrast image (upper left) and recognized by their fibrillar actin staining with phalloidin (lower left) are intensely stained for raver1 with 5D5. Nuclei were identified by DAPI staining (lower right), but a nuclear localization of raver1 could not be determined at the resolution of such images. Bars, 20 μm .

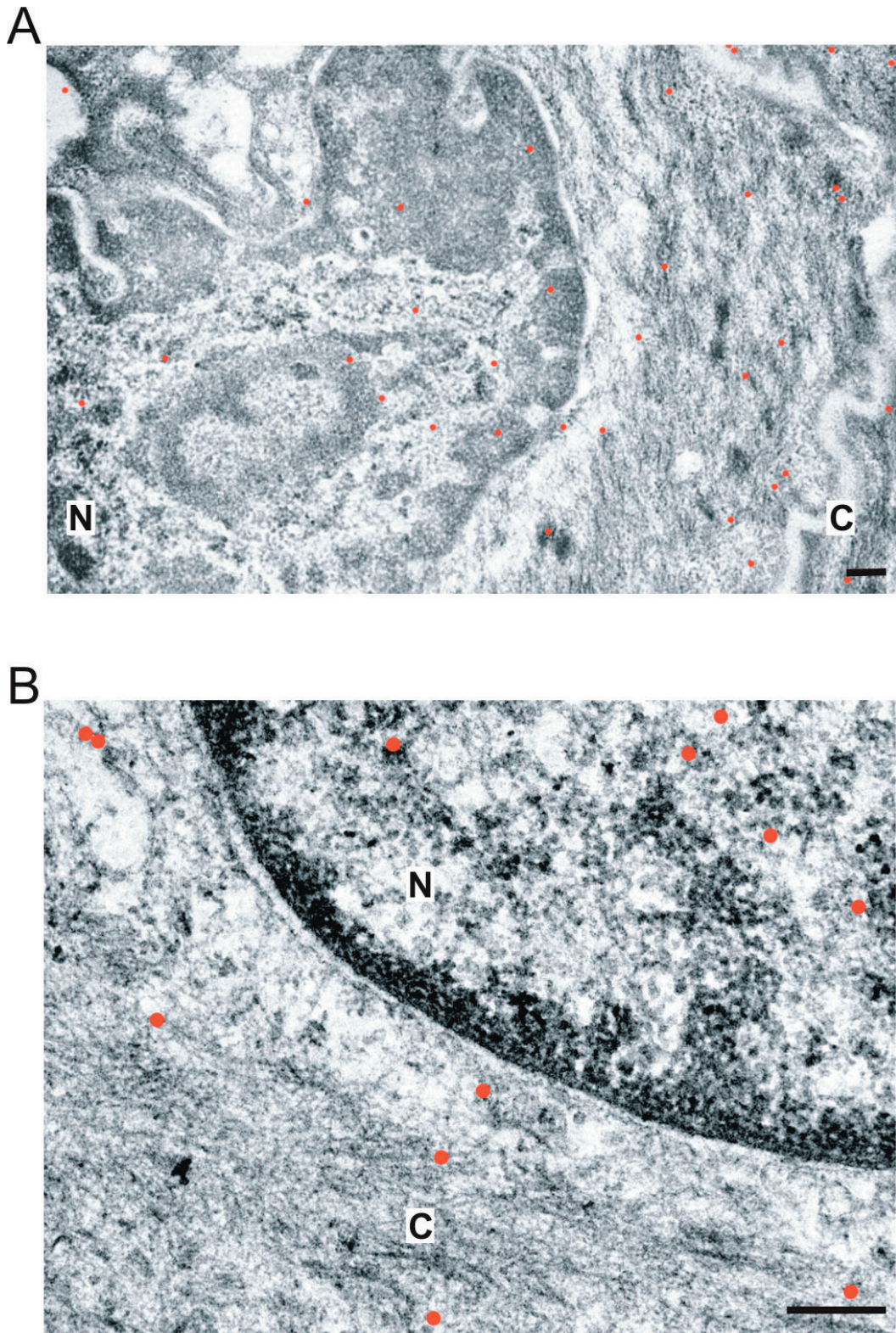


Figure 37. Immunoelectron microscopic analysis of *raver1* in smooth muscle tissue. (A and B) Ultrathin sections of smooth muscle from mouse urinary bladder (A) and mouse aorta (B) were labelled with 5D5 and a 10 nm gold-conjugated secondary antibody (enlarged, pseudocoloured red). *Raver1* is seen present in the nuclei (N) and the cytoplasm (C) of both types of smooth muscle cells. Bars, 200 nm

Discussion

We have previously observed that during skeletal muscle differentiation the hnRNP-like protein raver1 translocates from the nucleus to microfilament attachment sites in differentiated skeletal muscle at the sarcolemma (Huttelmaier et al. 2001). Based on these findings, we analyzed the subcellular distribution of raver1 in skeletal muscle in more detail and expanded our investigation to heart and smooth muscle. We demonstrate that the cytoplasmic accumulation of raver1 and its association with contractile elements is a common feature of all three types of muscle. In addition, a minor fraction of the protein was always present in the nucleus. A detailed analysis of stretched myofibrils and ultrathin sections of skeletal muscle showed that raver1, like alpha-actinin but unlike vinculin, is not restricted to the costameres. Instead, it is also an integral sarcomeric component, mainly localized in the I-Z-I region. In heart muscle, raver1 was also found as a prominent component of intercalated discs, which are also rich in vinculin, metavinculin and alpha actinin (Tokuyasu et al. 1981; Witt et al. 2004).

Immunolabelling of myofibrils (Figure 34) revealed that the distribution of raver1 does not exactly correspond to that of its ligand alpha-actinin. As expected, the latter is strictly confined to the Z-disc (Tokuyasu et al. 1981; McKenna et al. 1986), whereas raver1 flanks this structure being thus mainly located in the I-regions. This partial overlap *in situ* may either reflect a true differential localization of the two proteins, or, alternatively, it could be the consequence of steric hindrance of antibody binding caused by additional proteins. *In vitro*, raver1 directly interacts with vinculin and alpha-actinin and complexes containing all three proteins can be recovered from cell extracts by immunoprecipitation (Huttelmaier et al. 2001). Based on our immunolabelling analyses, a direct interaction between raver1 and alpha actinin *in situ* might be possible, but cannot be proven.

As revealed by immunoelectron microscopy, raver1 was occasionally also found at the M-band (Figures 34 and 35). Different locations within the sarcomere have also been described for other proteins such as obscurin (Young et al. 2001) and FHL2/DRAL (Lange et al. 2002), but at present it is not clear whether translocations of such proteins occur within the sarcomere, or whether there are distinct subpopulations of these components present at different sites (Lange et al. 2006).

The dual localization of raver1 in the nuclear and sarcomeric compartment of muscle, together with its structural organization, based on which it was identified as a member of a protein family engaged in RNA modification, suggests that raver1 may also have a dual function. Since raver1 harbours three RRM and affects PTB-mediated RNA splicing *in vitro* (Gromak et al. 2003) it has been speculated that raver1 could be involved in processing and delivery of specific mRNAs to the sarcomere and thus mediate site-specific synthesis of sarcomeric proteins (Jockusch et al. 2003). Such sarcomeric localization has been reported for the mRNAs of vimentin, desmin and vinculin (Morris and Fulton 1994). However, direct RNA binding of raver1 remains to be shown. Alternatively, the RRMs may act as binding

modules mediating protein-protein interactions and could be involved in vinculin binding (Huttelmaier et al. 2001).

However, other possibilities need to be considered. It is commonly accepted that the functional plasticity of muscle critically depends on intracellular communicators, which translate mechanical signals into altered protein activities or gene expression profiles. For example, a signalling complex involving the kinase domain (TK) of the giant sarcomeric protein titin regulates nuclear translocation of MURF-2. Nuclear MURF-2 interacts with the transactivation domain of serum response factor (SRF), which indirectly leads to suppression of SRF-dependent muscle gene expression (Lange et al. 2005). MURF-2 thus represents a member of a constantly growing, heterogeneous group of proteins that may translocate from the sarcomere to the nucleus to perform a sensory or messenger function. Other examples of such proteins are for example myopodin (Weins et al. 2001; Sanchez-Carbayo et al. 2003), myopalladin (Bang et al. 2001) and CARP (Jeyaseelan et al. 1997; Bang et al. 2001; Miller et al. 2003). However, for most proteins the physiological consequences of these translocations remain to be shown (Lange et al. 2006).

At present, we cannot determine whether raver1 exerts primarily structural, transport, signalling or regulatory functions in muscle. Raver1 knock-out mice are viable and fertile and myofibrils isolated from these animals are morphologically indistinguishable from their wild type counterparts (B. Kleinhenz and H.H. Arnold, personal communication). Even though we recently identified a raver1-related protein (raver2, Kleinhenz et al. 2005) the possibility of mere functional redundancy is rather unlikely, since raver2 is not expressed in muscle tissue. Furthermore, genetic analyses do not indicate any other raver isoforms.

In summary, these facts argue against a purely structural function of raver1. Apparently, the protein is not required for initial sarcomere formation and maintenance. However, the possibility remains that raver1 in costameres and intercalated disks contributes to proper muscle function by modulating either the molecular architecture of microfilament attachment sites or signalling pathways that target these attachment sites. Further studies, involving physiological analyses of animals, muscle and isolated myofibrils on raver1-depleted mice are required to clarify these issues.

Acknowledgements

We thank R. Frank for providing us with the raver1 spot-synthesized peptides (German Research centre for Biotechnology, GBF, Braunschweig) and T. Messerschmidt for technical assistance. We gratefully acknowledge permission from B. Kleinhenz and H.H. Arnold (TU Braunschweig) to quote their unpublished results and the assistance of V. Oliveri and U. Sauder (Biozentrum, Basel) with sample preparation for electron microscopy. This work was supported by grants of the Swiss National Science Foundation and the M.E. Müller Foundation (to CAS) and the Deutsche Forschungsgemeinschaft (to SI. and BMJ), and of the 'Fonds der Chemischen Industrie' (to BMJ). A.Z. was the recipient of a 'G. Lichtenberg fellowship', within an International Graduate College funded by the Land Niedersachsen, Germany.

3.4 Localization of raver1 in tissues and cells by immunoelectron microscopy

For an extended characterization of raver1 distribution, we have performed additional immunoelectron microscopy studies on a variety of different muscle tissues, cultured cell lines and isolated oocyte nuclei.

3.4.1 Raver1 in rodent muscle tissues

The immunogold labeling studies that were carried out on ultrathin sections of rodent muscle tissue are summarized in Table 6.

Table 6. Immunoelectron microscopic analysis of rodent muscle tissues with raver1 antibodies; nd, not done.

	Raver1 antibody	
	N-terminal	C-terminal
Striated muscle		
Rat neonatal heart	nd	+
Murine adult heart	nd	+
Murine skeletal muscle	+	+
Smooth muscle		
Murine aorta	+	+
Murine urinary bladder	nd	+
Murine uterus	+	+

Immunofluorescence labeling of mouse uterine smooth muscle tissue with 5D5 revealed raver1 to be present predominantly in the cytoplasm of myofibrils, whereas in the nucleus, raver1 appeared to be absent (Zieseniss 2005; Zieseniss et al. 2007). However, at the ultrastructural level, raver1 was shown to localize to both, the cytoplasm as well as the nucleus (Figure 38 A). An association with distinct structures was not evident in any cellular compartment. Instead, raver1 appeared to be randomly distributed.

A similar distribution of raver1 in the nucleus and the cytoplasm was also observed in neonatal rat heart labeled with the raver1 antibody 5G6, which binds to an N-terminal epitope in raver1 (Figure 38 B).

Previous immunofluorescence studies with raver1 antibody 7D3, which binds to the C-terminal region of raver1, revealed a pronounced labeling of the sarcomeric I-regions resulting in a typical cross-striation pattern (Zieseniss et al. 2007). However, at the ultrastructural level, labeling with the 5G6 antibody did not reveal accumulation in a distinct band of the sarcomere.

In summary, observations at the ultrastructural level supplement previous immunofluorescence microscopy studies (Huttelmaier et al. 2001; Jockusch et al. 2003; Zieseniss 2005; Zieseniss et al. 2007). In particular, the data support the dual residency of raver1 in the nucleus and cytoplasm in all types of muscle tissues tested. In striated muscle, antibodies against the C-terminal region of raver1 revealed an accumulation of raver1 at the I-bands of sarcomers at the cellular and ultrastructural level, leading to a distinct striated pattern (Zieseniss et al. 2007).

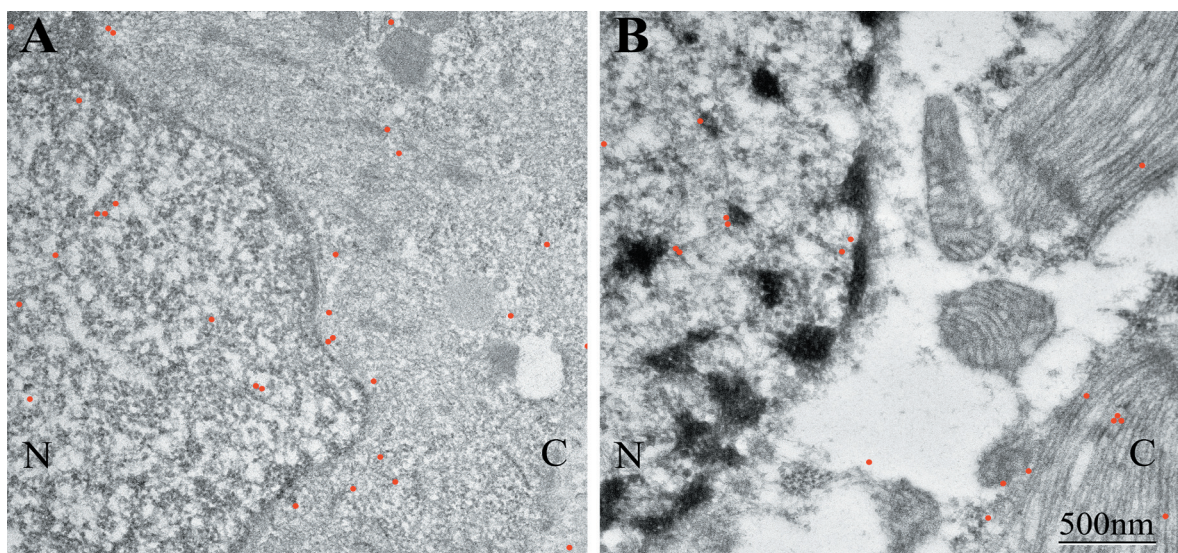


Figure 38. Localization of raver1 in muscle tissues by indirect immunoelectron microscopy. Ultrathin sections of (A) mouse uterine smooth muscle and (B) neonatal rat heart were labeled with the raver1 antibodies 5D5 and 5G6, respectively. Gold particles (enlarged, pseudocoloured red) were seen in both, the cytoplasm (C) and the nucleus (N).

3.4.2 Distribution of raver1 in cultured cells

As listed in Table 7, immunolocalization studies at the ultrastructural level were carried out on a number of cultured cell lines, on primary rat neonatal ventricular cardiomyocytes (NVCM) (Pinson 1990), primary rat aortic smooth muscle cells, and on isolated nuclei from *Xenopus laevis* oocytes (Reichelt et al. 1990; Jarnik and Aebi 1991).

Table 7. Indirect immunoelectron microscopic studies on ultrathin sections of cultured cells and isolated *Xenopus laevis* oocytes with raver1 antibodies; nd, not done.

	Raver1 antibody	
	N-terminal	C-terminal
Cultured cells		
HeLa	nd	+
Rat2	nd	+
C2C12	+	+
Rat aortic smooth muscle cells	+	+
NVCM	nd	+
Isolated nuclei		
<i>Xenopus</i> oocyte nuclei	+	+

Immunogold labeling of ultrathin sections from different cultured cell lines with raver1 antibodies showed that raver1 was evenly distributed in the cytoplasm (C) and the nucleus (N) in all cells tested (Figure 39). An association of raver1 with distinct cellular structures was not evident. In Rat2 fibroblasts, raver1-associated gold particles were less frequent than in HeLa cells (Figure 39 A, B). The highest levels of raver1 were detected in aortic smooth muscle cells using 5G6, which binds to the N-terminus of raver1 (Figure 39 C).

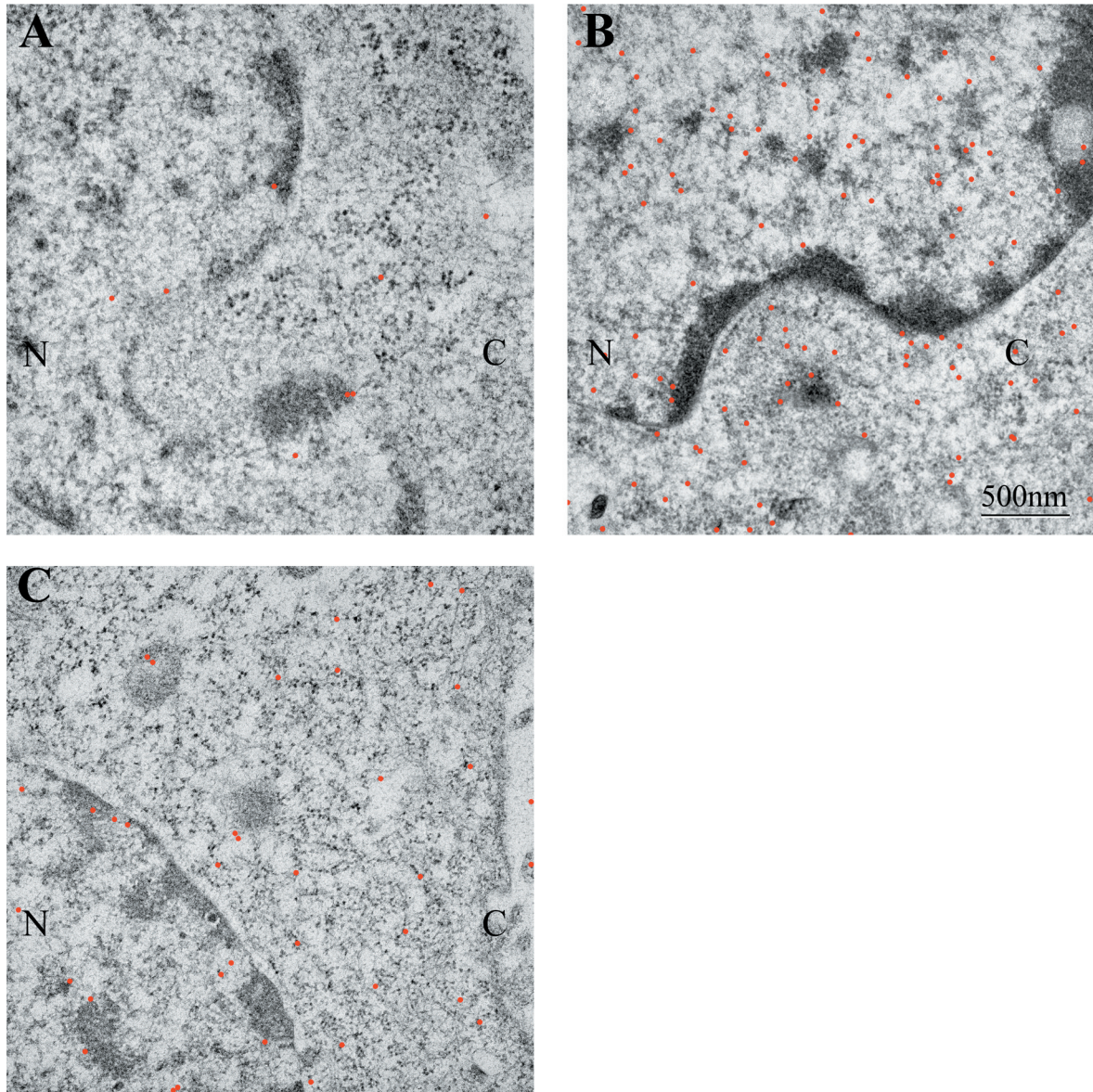


Figure 39. Localization of raver1 in cultured cells by indirect immunoelectron microscopy. (A) Rat2 cells were reacted with raver1 antibody 7D3, (B) HeLa cells with 5D5 and (C) aortic smooth muscle cells with 5G6. Gold particles (enlarged, pseudocoloured red) were seen in both, the cytoplasm (C) and the nucleus (N) of all cells tested.

3.4.3 Raver1 localizes to the nuclear face of oocyte nuclei

In order to study a potential role of raver1 in nucleocytoplasmic transport, the distribution of raver1 at the nuclear envelope was examined at the ultrastructural level by pre-embedding labeling of nuclei from *X. laevis* oocytes. For this purpose, nuclei were manually dissected (Reichelt et al. 1990; Jarnik and Aebi 1991) and incubated with 8 nm colloidal gold-coupled raver1 antibodies 5G6, 5D5 and 7D3. Subsequently, the nuclei were fixed, thin-sectioned and processed for CTEM analysis.

As illustrated in the electronmicrograph in Figure 40, incubation of nuclei with 5D5 antibody yielded the most pronounced labeling of the nuclear envelope (NE), with the majority of gold particles residing at the nuclear face (NF). The schematic representation of the nuclear pore complex (NPC) shown in Figure 40 B illustrates that in cross section, the distal ring (DR), nuclear ring (NR), and cytoplasmic ring (CR) are generally located between -120 nm to -50 nm, -50 nm to 0 nm, and 0 nm to 60 nm from the central plane, respectively (Fahrenkrog et al. 2002; Beck et al. 2004). Because raver1 appeared to reside at a consistent location with respect to the NPC, we measured the vertical distance of the gold particles from the central plane of the NE. The corresponding histograms are presented in Figure 40 C.

In total, 145 gold particles were scored, 97.9% of which were located at the NF and only 2.1% of gold particles were found on the cytoplasmic face (CF) of the NE. The vast majority of gold particles on the NF (97.1%) were associated with the DR of the nuclear basket. A similar distribution was observed with gold-conjugated 7D3 antibody, where 85.7% of the 56 scored gold particles were located at the NF. Again, these gold particles accumulated at the DR. Labeling with gold-conjugated 5G6 antibody, which recognizes an epitope at the N-terminus of raver1, revealed a corresponding distribution of gold particles.

In summary, immunogold electron microscopy with three different raver1 antibodies suggests that raver1 interacts with the NPC of *Xenopus* oocyte nuclei. At the NPC, raver1 seems to preferentially associate with the DR of the nuclear basket. However, because the nucleoplasm is not structurally preserved during pre-embedding labeling experiments, the distribution of raver1 throughout the nucleus remains unresolved.

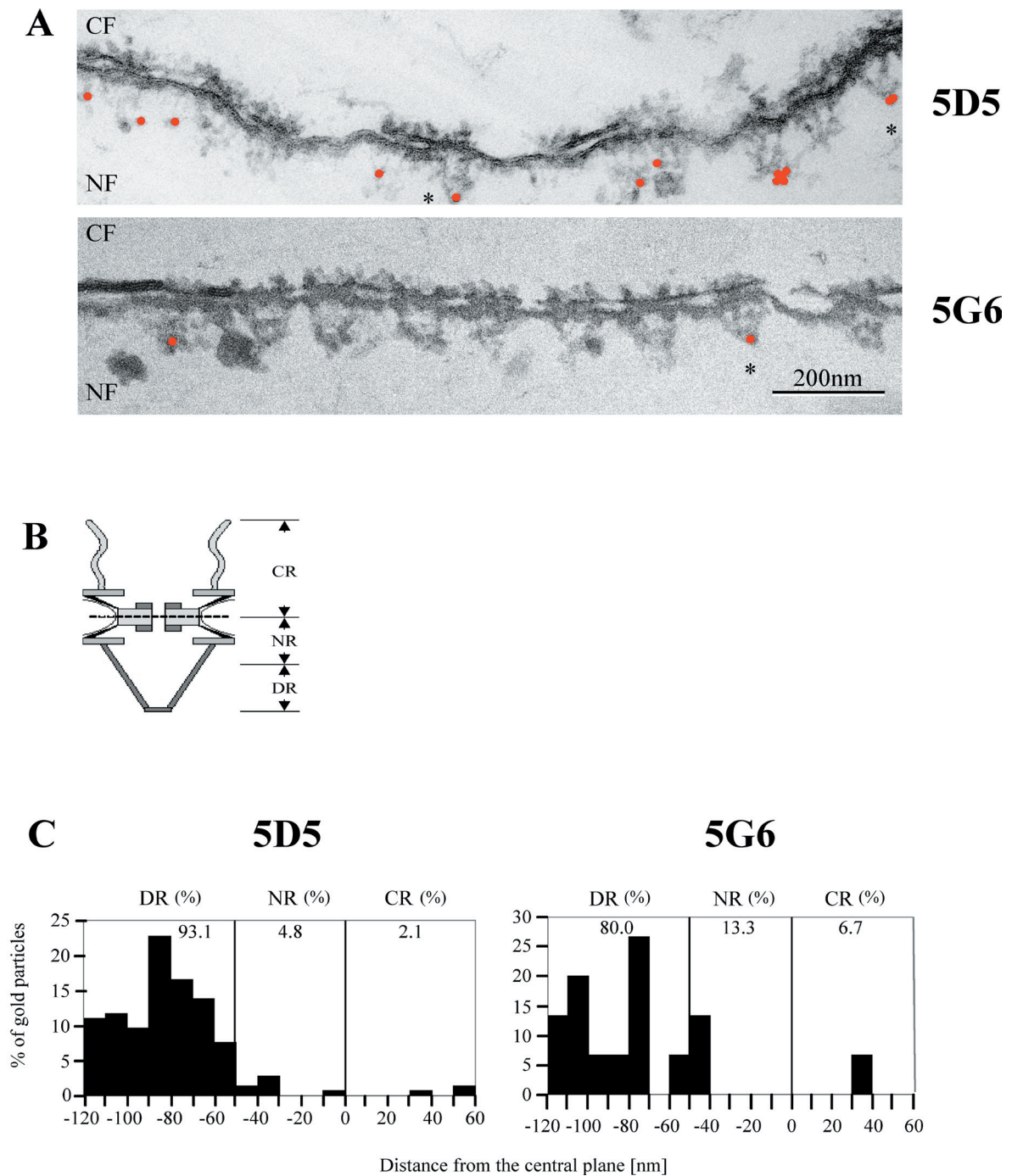


Figure 40. Raver1 at the NPC of nuclei from *X. laevis* oocytes. Isolated nuclei were pre-embedding labeled with the 8 nm gold-coupled raver1 antibodies 5D5 and 5G6, and processed for CTEM. (A) The gold particles (enlarged, pseudocoloured with red) either antibody were seen predominantly at the DR of the NPC. Asterisks indicate raver1 directly located at the DR of longitudinal cross-sectioned NPCs. CF; cytoplasmic face, NF; nucleoplasmic face. (B) Schematic cross-section through the NPC from *Xenopus laevis* oocyte nuclei. The dashed line represents the central plane of the nuclear envelope. CR, cytoplasmic ring; NR, nuclear ring, DR, distal ring. (Adapted from Stoffler et al. 1999). (C) Quantification of the gold particles.

3.4.4 Raver1 is a ligand for actin *in vitro*

Because previous studies suggested that raver1 might be a direct binding partner for actin (Huttelmaier et al. 2001) and more recent data indicates that the presence of raver1 induces bundling and networking of prepolymerized F-actin filaments *in vitro* (Zieseniss 2005), we wanted to examine the interaction of actin with raver1 in more detail.

In the study presented below, we examined the interaction of i) recombinantly expressed full-length raver1 protein (R1-FL) and ii) a C-terminal raver1 fragment (R1-ΔN) with highly purified rabbit skeletal muscle actin. In particular, we incubated G-actin and prepolymerized F-actin filaments with R1-FL and R1-ΔN, respectively, and analyzed their interaction by high-speed cosedimentation and subsequent SDS-PAGE analysis. In addition, high-speed pellets were examined at the ultrastructural level to visualize the effects of raver1 on the supramolecular organization of actin.

The basic molecular characteristics of R1-FL and R1-ΔN are summarized in Table 8.

Table 8. Molecular characteristics of recombinantly expressed full-length raver1 (R1-FL) and a C-terminal raver1 fragment (R1-ΔN). Both constructs comprise N-terminal polyhistidine tags; RRM, RNA-recognition motif; NLS, nuclear localization signal.

Construct	Amino acids		Mw [kDa]	RRM	NLS
R1-FL	748	(1 – 748)	86	3	2
R1-ΔN	306	(442 – 748)	35	---	1

In the standard actin sedimentation assay (see Chapter 1.3), G-actin exclusively remains in the supernatant (data not shown). Similarly, control experiments with recombinantly expressed R1-FL alone showed that after high-speed centrifugation, the 86 kDa raver1 and numerous degradation products remained in the supernatant (Figure 41 A, left). It should be noted that recombinant R1-FL and the R1-ΔN fragment, could only be produced in insect cells and both proteins were difficult to efficiently purify, as well as extremely prone to degradation. Cosedimentation of mixtures of G-actin and R1-FL at high speed resulted in a partial redistribution of both, actin and R1-FL to the pellet fraction (Figure 41 A, middle),

suggesting that a pelletable supramolecular structure was formed by the association of raver1 with actin. If prepolymerized, phalloidin-stabilized F-actin filaments were incubated with R1-FL, virtually all of the actin was pelleted. This finding indicates, that the interaction with raver1 did not result in a depolymerization of preformed filaments. Consistent with the results obtained for R1-FL alone (Figure 41 A, right), approximately half of the R1-FL and interestingly most of the degradation products remained in the supernatant. As revealed by electronmicrographs of negatively stained samples of the resuspended pellet fraction, the interaction of R1-FL with F-actin filaments led to their bundling (Figure 41 B).

To narrow down which region of the raver1 molecule interacts with actin, we performed cosedimentation assays with R1- Δ N, a \sim 35 kDa fragment corresponding to the C-terminus of raver1. High-speed centrifugation of R1- Δ N by itself left the fragment in the supernatant (Figure 41 A, left, S). If purified G-actin was mixed with R1- Δ N, most of the raver1 fragment and a significant fraction of the G-actin were found in the pellet (Figure 41 A, right, P). Currently, we do not know if in (S), the weak band at \sim 35 kDa represents raver1 fragment or a characteristic actin degradation product. In addition, the origin of the higher molecular weight band is unclear but might represent an aggregated form of R1- Δ N. Because the partial cosedimentation with G-actin was observed for the full-length and the C-terminal raver1 fragment, one might conclude that raver1 interacts with G-actin via its C-terminal region. It is also possible that this interaction induces the polymerization of actin into filaments that are pelleted. However, CTEM analysis of the cosedimented pellet fraction (Figure 41 B) revealed that pellets mainly consisted of unstructured protein aggregates (left) and filamentous structures (Figure 41 B, right) were rarely detected.

If prepolymerized, phalloidin-stabilized F-actin filaments were mixed with R1- Δ N (Figure 41 C), basically all of the raver1 fragment was pelleted together with the actin filaments. Electron microscopy analysis of the pellet fraction revealed that the presence of R1- Δ N induced the bundling of F-actin filaments (Figure 41 D), similar to the bundling activity observed for the full-length protein (Figure 41 B).

Together, the results from cosedimentation assays and the ultrastructural inspection corroborates the preliminary finding that raver1 interacts with actin *in vitro* (Zieseniss 2005). Furthermore, the bundling of prepolymerized F-actin filaments indicates that raver1 contains at least one binding site for filamentous actin, which appears to be located in the C-terminal part of the molecule.

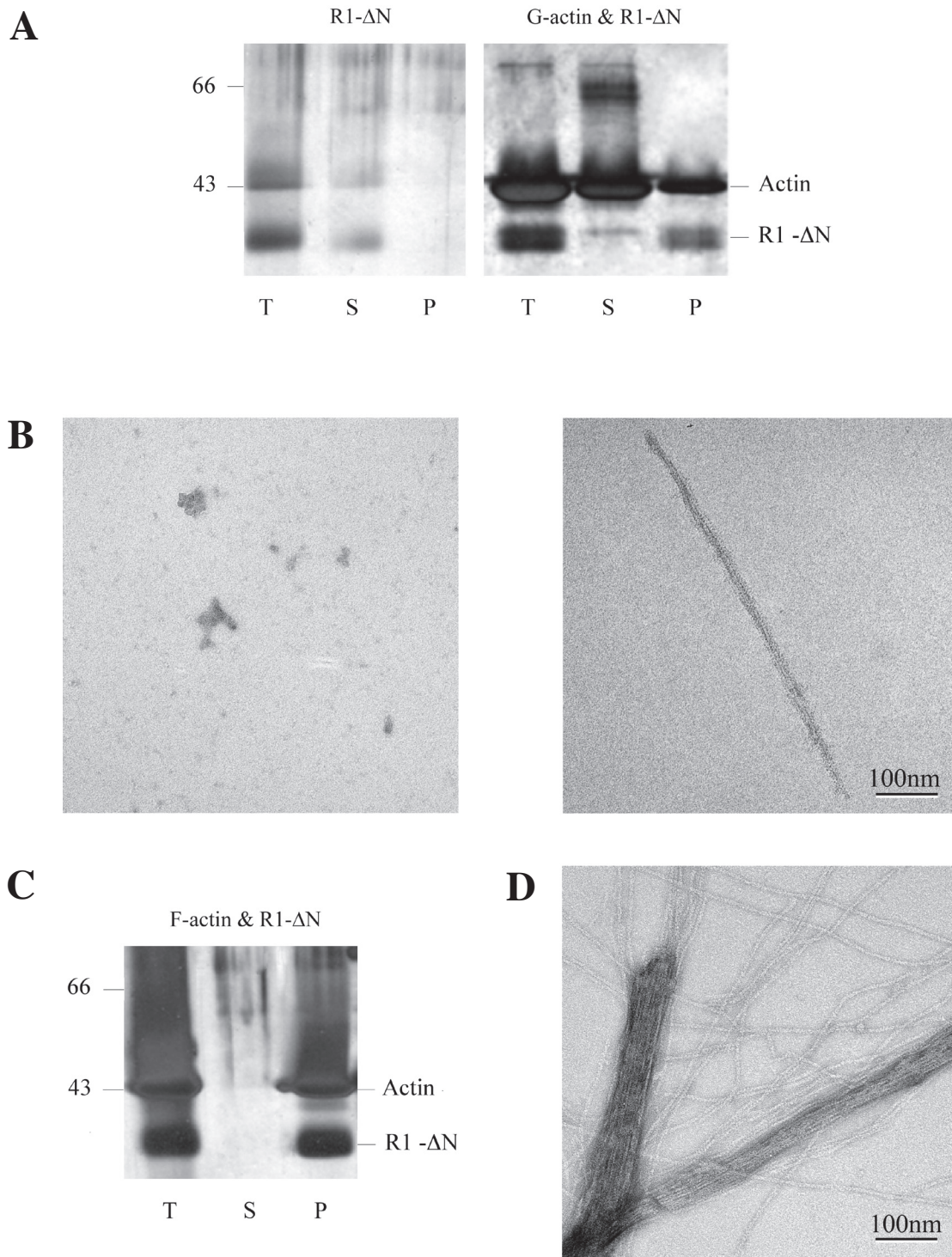


Figure 41. Interaction of actin with R1- Δ N. Aliquots of the total protein inputs (T), the supernatants after high-speed centrifugation (S) and the resuspended pellets (P) were subjected to a 12% SDS-PAGE and silver stained. In addition, aliquots of the resuspended pellets were negatively stained and analyzed by CTEM. (A, left panel) R1- Δ N remained entirely in the supernatant (S), whereas (A, right panel) R1- Δ N cosedimented with G-actin, forming mainly unstructured aggregates (B, left panel) and a minor fraction of filamentous structures (B, right panel). (C) R1- Δ N was entirely pelleted with phalloidin stabilized F-actin filaments and (D) induced the formation of actin filament bundles. The molecular masses in kDa of standard proteins are indicated on the left.

3.5 Conclusions and outlook

Cosedimentation assays and electron microscopy provide evidence that the hnRNP protein raver1 interacts with preformed F-actin filaments *in vitro*. In particular, it induced the formation of thick F-actin filament bundles. The number of ABPs with filament bundling activity is increasing (Ruzanov et al. 1999; Mulder et al. 2003, Michelot et al. 2005). At first sight, the nuclear localization of raver1 might appear inconsistent with its bundling activity, specifically since actin filaments are not observed in the nucleus under physiological conditions. However, we have also shown that raver1 is not only a nuclear protein, but is present in the cytoplasm as well. Moreover, other ABPs with bundling activity such as formins have also been detected in the nucleus. The actin-binding properties of the C-terminal deletion construct R1- Δ N were comparable to that of the full-length protein. This result indicated that the actin binding site(s) is located in the C-terminal region of raver1. Similarly, the binding site for alpha-actinin has been allocated to the C-terminal region, whereas binding of raver1 to its cytoplasmic ligands (meta)vinculin is mediated by the N-terminal region of the molecule (Hüttelmaier et al. 2001; Zieseniss 2005). Our data support and extend previous observations, which suggested that recombinantly expressed raver1 binds directly to actin *in vitro* (Zieseniss 2005).

Isolation of protein complexes containing actin, raver1 and PTB from undifferentiated C2C12 myoblasts, where raver1 primarily resides in the nucleus suggested that the interaction with actin might occur in the nucleus (Zieseniss 2005). Consistent with this notion, hnRNP U, another member of the hnRNP family, has been shown to cooperate with nuclear actin for productive transcription (Kukalev et al. 2005). Using three monoclonal antibodies that react with N- and C-terminal epitopes of raver1, our immunoelectron microscopy studies revealed a distinct nuclear localization of raver1 in *Xenopus* oocytes. Specifically, raver1 distinctly accumulated at the distal ring of the NPC baskets. Although actin has also been found to associate with the NPC as well as with a network of 'pore-linked filaments', which extend from the nuclear envelope deep into the nucleus (Hofmann et al. 2001; Kiseleva et al. 2004), the colocalization of raver1 and actin at the NPC remains to be investigated. In addition, structure of the nucleoplasm is not preserved during the pre-embedding labeling procedure, so that the localization of raver1 within the nucleus is not revealed. Hence, we were not able to confirm the localization of raver1 in perinucleolar bodies, which was previously described by immunofluorescence (Hüttelmaier et al. 2001).

Nuclear actin was seen to play an important role in the nuclear export of e.g. retroviral RNAs (Hofmann et al. 2001). Likewise, raver1 has been considered to act as chaperone for mRNAs, accompanying them on their journey from the nucleus to the cytoplasm (Jockusch et al. 2003). Hence, one could speculate that both proteins might be coexported (possibly with specific mRNA cargo) to a common cytoplasmic destination, such for instance to the I-bands of skeletal muscle sarcomers (Hüttelmaier et al. 2001; Zieseniss 2005; Zieseniss et al. 2007). However, a functional interplay of raver1 and actin in the nucleus and combined nuclear

export of both proteins is still hypothetical and has to be elucidated in future experiments.

To study the nuclear export of raver1 and a potential translocation mechanism for raver1 and actin to the cytoplasm, proteins involved in the nuclear export of actin, such as exportin6 (Stuven et al. 2003; Bohnsack et al. 2006), could be probed for their ability to interact with raver1 in colocalization and coimmunoprecipitation experiments.

In addition, other candidate target proteins to be studied are those present at the basket of NPCs, which are thought to participate in nuclear protein export, such as for instance the tumor promoter region protein Tpr and specific nucleoporins (Frosst et al. 2002; Krull et al. 2004).

A major drawback in studying the interactions of raver1 with different target proteins lies in the difficulties expressing recombinant raver1 and fragments thereof. The protein used for our *in vitro* studies was produced in insect cells at low yield. In addition, purified raver1 showed a strong tendency to aggregate and was extremely prone to proteolytic degradation. However, to further characterize the interaction with actin, it is essential to carry out systematic binding experiments with recombinantly expressed raver1 fragments. Therefore, one imminent task is to explore alternative expression systems.

References

- Aebi, U., W.E. Fowler, G. Isenberg, T.D. Pollard and P.R. Smith (1981). "Crystalline actin sheets: their structure and polymorphism." *J Cell Biol* **91**(2 Pt 1): 340-51.
- Aebi, U., R. Millonig, H. Savo and A. Engel (1986). "The three-dimensional structure of the actin filament revisited." *Ann N Y Acad Sci* **483**: 100-19.
- Aebi, U., P.R. Smith, G. Isenberg and T.D. Pollard (1980). "Structure of crystalline actin sheets." *Nature* **288**(5788): 296-98.
- Aebi, U., B. ten Heggeler, L. Onorato and M.K. Showe (1977). "New method for localizing proteins in periodic structures: Fab fragment labeling combined with image processing of electron micrographs." *Proc Natl Acad Sci U S A* **74**(12): 5514-18.
- Allen, T.M. and P.R. Cullis (2004). "Drug delivery systems: entering the mainstream." *Science* **303**(5665): 1818-22.
- Ansorge, W. (1985). "Fast and sensitive detection of protein and DNA bands by treatment with potassium permanganate." *J Biochem Biophys Methods* **11**(1): 13-20.
- Archer, S.K., C. Claudianos and H.D. Campbell (2005). "Evolution of the gelsolin family of actin-binding proteins as novel transcriptional coactivators." *Bioessays* **27**(4): 388-96.
- Bachmann, M.F. and M.R. Dyer (2004). "Therapeutic vaccination for chronic diseases: a new class of drugs in sight." *Nat Rev Drug Discov* **3**, 81-88.
- Bachmann, M.F. and R.M. Zinkernagel (1996). "The influence of virus structure on antibody responses and virus serotype formation." *Immunol Today* **17**(12): 553-58.
- Bang, M.L., R.E. Mudry, A.S. McElhinny, K. Trombitas, A.J. Geach, R. Yamasaki, H. Sorimachi, H. Granzier, C.C. Gregorio and S. Labeit (2001). "Myopalladin, a novel 145-kilodalton sarcomeric protein with multiple roles in Z-disc and I-band protein assemblies." *J Cell Biol* **153**(2): 413-27.
- Barden, J.A., M. Miki, B.D. Hambly and C.G. dos Remedios (1987). "Localization of the phalloidin and nucleotide-binding sites on actin." *Eur J Biochem* **162**(3): 583-88.
- Baschong, W., L. Hasler, M. Häner, J. Kistler and U. Aebi (2003). "Repetitive versus monomeric antigen presentation: direct visualization of antibody affinity and specificity." *J Struct Biol* **143**(3): 258-62.

- Baschong, W., R. Suetterlin and R.H. Laeng (2001). "Control of autofluorescence of archival formaldehyde-fixed, paraffin-embedded tissue in confocal laser scanning microscopy (CLSM)." J Histochem Cytochem **49**, 1565-72.
- Beck, M., F. Forster, M. Ecke, J.M. Plitzko, F. Melchior, G. Gerisch, W. Baumeister and O. Medalia (2004). "Nuclear pore complex structure and dynamics revealed by cryoelectron tomography." Science **306**(5700): 1387-90.
- Belmont, L.D., G.M. Patterson and D.G. Drubin (1999). "New actin mutants allow further characterization of the nucleotide binding cleft and drug binding sites." J Cell Sci **112**(9): 1325-36.
- Berg, M., J. Difatta, E. Hoiczky, R. Schlegel and G. Ketner (2005). "Viable adenovirus vaccine prototypes: high-level production of a papillomavirus capsid antigen from the major late transcriptional unit." Proc Natl Acad Sci U S A **102**(12): 4590-95.
- Blondin, L., V. Sapountzi, S.K. Maciver, C. Renoult, Y. Benyamin and C. Roustan (2001). "The second ADF/cofilin actin-binding site exists in F-actin, the cofilin-G-actin complex, but not in G-actin." Eur J Biochem **268**(24): 6426-34.
- Bohnsack, M.T., T. Stuken, C. Kuhn, V.C. Cordes and D. Görlich (2006). "A selective block of nuclear actin export stabilizes the giant nuclei of *Xenopus* oocytes." Nat Cell Biol **8**(3): 257-63.
- Brandenberger, R., R.A. Kammerer, J. Engel and M. Chiquet (1996). "Native chick laminin-4 containing the beta 2 chain (s-laminin) promotes motor axon growth." J Cell Biol **135**, 1583-92.
- Bremer, A. and U. Aebi (1992). "The structure of the F-actin filament and the actin molecule." Curr Opin Cell Biol **4**(1): 20-26.
- Bremer, A., R.C. Millonig, R. Sütterlin, A. Engel, T.D. Pollard and U. Aebi (1991). "The structural basis for the intrinsic disorder of the actin filament: the "lateral slipping" model." J Cell Biol **115**(3): 689-703.
- Brookman J.L., A.J. Stott, P.J. Cheeseman, N.R. Burns, S.E. Adams, A.J. Kingsman and K. Gull (1995). "An immunological analysis of Ty1 virus-like particle structure." Virology **207**(1): 59-67.
- Bubb, M.R., L. Govindasamy, E.G. Yarmola, S.M. Vorobiev, S.C. Almo, T. Somasundaram, M.S. Chapman, M. Agbandje and R. McKenna (2002). "Polylysine induces an antiparallel actin dimer that nucleates filament assembly: crystal structure at 3.5 Å resolution." J Biol Chem **277**(23): 20999-1006.

- Bubb, M.R., J.R. Knutson, D.K. Porter and E.D. Korn (1994). "Actobindin induces the accumulation of actin dimers that neither nucleate polymerization nor self-associate." *J Biol Chem* **269**(41): 25592-97.
- Bubb, M. R., M.S. Lewis and E.D. Korn (1994). "Actobindin binds with high affinity to a covalently cross-linked actin dimer." *J Biol Chem* **269**(41): 25587-91.
- Buhle, E.L. Jr., W.E. Fowler, P.R. Smith and U. Aebi (1984). "Specific labeling of protein domains with antibody fragments." *J Ultrastruct Res* **89**(2): 165-78.
- Burkhard, P., S. Ivaninskii and A. Lustig (2002). "Improving coiled-coil stability by optimizing ionic interactions." *J Mol Biol* **318**(3): 901-1010.
- Burkhard, P., R. A. Kammerer, M.O. Steinmetz, G.P. Bourenkov and U. Aebi (2000). "The coiled-coil trigger site of the rod domain of cortexillin I unveils a distinct network of interhelical and intrahelical salt bridges." *Structure* **8**(3): 223-30.
- Burkhard, P., M. Meier and A. Lustig (2000). "Design of a minimal protein oligomerization domain by a structural approach." *Protein Sci* **9**(12): 2294-301.
- Burkhard, P., J. Stetefeld and S.V. Strelkov (2001). "Coiled coils: a highly versatile protein folding motif." *Trends Cell Biol* **11**, 82-8.
- Canto-Nogues, C., D. Hockley, C. Grief, S. Ranjbar, J. Bootman, N. Almond and I. Herrera (2001). "Ultrastructural localization of the RNA of immunodeficiency viruses using electron microscopy in situ hybridization and in vitro infected lymphocytes." *Micron* **32**(6): 579-89.
- Chackerian, B., M. Rangel, Z. Hunter and D.S. Peabody (2006). "Virus and virus-like particle-based immunogens for Alzheimer's disease induce antibody responses against amyloid-beta without concomitant T cell responses." *Vaccine* **24**, 6321-31.
- Chen, M. and X. Shen (2007). "Nuclear actin and actin-related proteins in chromatin dynamics." *Curr Opin Cell Biol* **19**(3): 326-30.
- Chik, J.K., U. Lindberg and C.E. Schutt (1996). "The structure of an open state of beta-actin at 2.65 Å resolution." *J Mol Biol* **263**(4): 607-23.
- Chiu, H., J. Morales and S. Gondvind (2006). "Identification and immuno-electron microscopy localization of p40, a protein component of immunosuppressive virus-like particles from *Leptopilina heterotoma*, a virulent parasitoid wasp of *Drosophila*." *J Gen Virol* **87**(pt2): 461-70.
- Cho, M. W. (2003). "Subunit protein vaccines: theoretical and practical considerations for HIV-1." *Curr Mol Med* **3**, 243-63.
- Clark, K. A., A. S. McElhinny, et al. (2002). "Striated muscle cytoarchitecture: an intricate web of form and function." *Annu Rev Cell Dev Biol* **18**: 637-706.

- Coluccio, L.M. and L.G. Tilney (1984). "Phalloidin enhances actin assembly by preventing monomer dissociation." J Cell Biol **99**(2): 529-35.
- Crick, F.H. and J.D. Watson (1956). "Structure of small viruses." Nature **177**(4506): 473-75.
- Disanza, A., A. Steffen, M. Hertzog, E. Frittoli, K. Rottner and G. Scita (2005). "Actin polymerization machinery: the finish line of signaling networks, the starting point of cellular movement." Cell Mol Life Sci **62**(9): 955-70.
- Domingo, G.J., S. Orru and R.N. Perham (2001). "Multiple display of peptides and proteins on a macromolecular scaffold derived from a multienzyme complex." J Mol Biol **305**, 259-67.
- Dormann, D. and C.J. Weijer (2006). "Chemotactic cell movement during Dictyostelium development and gastrulation." Curr Opin Genet Dev **16**(4): 367-73.
- Dos Remedios, C.G. and M.J. Dickens (1978). "Actin microcrystals and tubes formed in the presence of gadolinium ions." Nature **276**: 731-33.
- Drubin, D.G., H.D. Jones and K.F. Wertman (1993). "Actin structure and function: roles in mitochondrial organization and morphogenesis in budding yeast and identification of the phalloidin-binding site." Mol Biol Cell **4**(12): 1277-94.
- Egelman, E.H., N. Francis and D.J. Derosier (1982). "F-actin is a helix with a random variable twist." Nature **298**(5870): 131-35.
- Elzinga, M. and J.J. Phelan (1984). "F-actin is intermolecularly crosslinked by N,N'-p-phenylenedimaleimide through lysine-191 and cysteine-374." Proc Natl Acad Sci U S A **81**(21): 6599-602.
- Engel, A. (1978). "Molecular weight determination by scanning transmission electron microscopy." Ultramicroscopy **3**(3): 273-81.
- Engel, A., and C. Colliex (1993). "Application of scanning transmission electron microscopy to the study of biological structure." Curr Opin Biotechnol **4**(4): 403-11.
- Engel, A. and R. Reichelt (1988). "Processing of quantitative scanning transmission electron micrographs." Scanning Microsc Suppl **2**: 285-93.
- Ensign, D., M. Young and T. Douglas (2004). "Photocatalytic synthesis of copper colloids from CuII by the ferrihydrite core of ferritin." Inorg Chem **43**(11): 3441-46.
- Estes, J.E., L.A. Selden and L.C. Gershman (1981). "Mechanism of action of phalloidin on the polymerization of muscle actin." Biochemistry **20**(4): 708-12.

- Fahrenkrog, B., B. Maco, A.M. Fager, J. Köser, U. Sauder, K.S. Ullman and U. Aebi (2002). "Domain-specific antibodies reveal multiple-site topology of Nup153 within the nuclear pore complex." *J Struct Biol* **140**(1-3): 254-67.
- Faulstich, H., S. Zobeley, D. Heintz and G. Drewes (1993). "Probing the phalloidin binding site of actin". *FEBS Lett* **318**(3): 218-22.
- Flenniken, M.L., L.O. Liepold, B.E. Crowley, D.A. Willits, M.J. Young and T. Douglas (2005). "Selective attachment and release of a chemotherapeutic agent from the interior of a protein cage architecture." *Chem Commun (Camb)*(4): 447-49.
- Flenniken, M. L., D. A. Willits, A.L. Harmsen, L.O. Liepold, A.G. Harmsen, M.J. Young and T. Douglas (2006). "Melanoma and lymphocyte cell-specific targeting incorporated into a heat shock protein cage architecture." *Chem Biol* **13**(2): 161-70.
- Fowler, W.E. and U. Aebi (1982). "Polymorphism of actin paracrystals induced by polylysine." *J Cell Biol* **93**(2): 452-58.
- Fowler, W.E. and U. Aebi (1983). "A consistent picture of the actin filament related to the orientation of the actin molecule." *J Cell Biol* **97**(1): 264-69.
- Frank, R. and H. Overwin (1996). "SPOT synthesis. Epitope analysis with arrays of synthetic peptides prepared on cellulose membranes." *Methods Mol Biol* **66**: 149-69.
- Frosst, P., T. Guan, C. Subauste, K. Hahn and L. Gerace (2002). "Tpr is localized within the nuclear basket of the pore complex and has a role in nuclear protein export." *J Cell Biol* **156**(4): 617-30.
- Galkin, V.E., M.S. VanLoock, A. Orlova and E.H. Egelman (2002). "A new internal mode in F-actin helps explain the remarkable evolutionary conservation of actin's sequence and structure." *Curr Biol* **12**(7): 570-75.
- Gallwitz, D. and I. Sures (1980). "Structure of a split yeast gene: complete nucleotide sequence of the actin gene in *Saccharomyces cerevisiae*." *Proc Natl Acad Sci U S A* **77**(5): 2546-50.
- Gard, D.L. (1999). "Confocal microscopy and 3-D reconstruction of the cytoskeleton of *Xenopus* oocytes." *Microsc Res Tech* **44**(6): 388-414.
- Georgens, C., J. Weyermann and A. Zimmer (2005). "Recombinant virus like particles as drug delivery system." *Curr Pharm Biotechnol* **6**(1): 49-55.
- Ghetti, A., S. Pinol-Roma, M. Michael, C. Morandi and G. Dreyfuss (1992). "hnRNP I, the polypyrimidine tract-binding protein: distinct nuclear localization and association with hnRNAs." *Nucleic Acids Res* **20**(14): 3671-78.

- Gimona, M., J. Vandekerckhove, M. Goethals, M. Herzog, Z. Lando and J.V. Small (1994). "Beta-actin specific monoclonal antibody." Cell Motil Cytoskeleton **27**, 108-16.
- Gonsior, S. M., S. Platz, S. Buchmeier, U. Scheer, B.M. Jockusch and H. Hinssen (1999). "Conformational difference between nuclear and cytoplasmic actin as detected by a monoclonal antibody." J Cell Sci **112** (Pt 6): 797-809.
- Graceffa, P. and R. Dominguez (2003). "Crystal structure of monomeric actin in the ATP state. Structural basis of nucleotide-dependent actin dynamics." J Biol Chem **278**(36): 34172-80.
- Granito, A., L. Muratori, P. Muratori, G. Pappas, M. Guidi, F. Cassani, U. Volta, A. Ferri, M. Lenzi and F.B. Bianchi (2006). "Antibodies to filamentous actin (F-actin) in type 1 autoimmune hepatitis." J Clin Pathol **59**, 280-84.
- Green, N.S., E. Reisler and K.N. Houk (2001). "Quantitative evaluation of the lengths of homobifunctional protein cross-linking reagents used as molecular rulers." Protein Sci **10**(7): 1293-304.
- Greenwood, J., A.E. Willis and R.N. Perham (1991). "Multiple display of foreign peptides on a filamentous bacteriophage. Peptides from Plasmodium falciparum circumsporozoite protein as antigens." J Mol Biol **220**, 821-27.
- Gromak, N., A. Rideau, J. Southby, A.D.J. Scadden, C. Gooding, S. Hüttelmaier, R.H. Singer and C.W.J. Smith et al. (2003). "The PTB interacting protein raver1 regulates alpha-tropomyosin alternative splicing." Embo J **22**(23): 6356-64.
- Grummt, I. (2006). "Actin and myosin as transcription factors." Curr Opin Genet Dev **16**(2): 191-6.
- Grunwald, D., M.C. Cardoso, H. Leonhardt and V. Buschmann (2005). "Diffusion and binding properties investigated by Fluorescence Correlation Spectroscopy (FCS)." Curr Pharm Biotechnol **6**, 381-86.
- Guo, Y., R.A. Kammerer and J. Engel (2000). "The unusually stable coiled-coil domain of COMP exhibits cold and heat denaturation in 4-6 M guanidinium chloride." Biophys Chem **85**(2-3): 179-86.
- Harris, J.R. and P. Agutter (1970). "A negative staining study of human erythrocyte ghosts and rat liver nuclear membranes." J Ultrastruct Res **33**(3): 219-32.
- Heidecker, M., Y. Yan-Marriott and G. Marriott (1995). "Proximity relationships and structural dynamics of the phalloidin binding site of actin filaments in solution and on single filaments on heavy meromyosin". Biochemistry **34**(35): 11017-25.

- Hesterkamp, T., A.G. Weeds and H.G. Mannherz (1993). "The actin monomers in the ternary gelsolin: 2 actin complex are in an antiparallel orientation." Eur J Biochem **218**(2): 507-13.
- Hoenger, A. and U. Aebi (1996). "3-D reconstruction from ice-embedded and negatively stained biomacromolecular assemblies: A critical comparison." J. Struct. Biol. **117**: 99-116.
- Hofmann, W., B. Reichart, A. Ewald, E. Müller, I. Schmitt, R.H. Stauber, F. Lottspeich, B.M. Jockusch, U. Scheer, J. Hauber and M.-C. Dabauvalle (2001). "Cofactor requirements for nuclear export of Rev response element (RRE)- and constitutive transport element (CTE)-containing retroviral RNAs. An unexpected role for actin." J Cell Biol **152**(5): 895-910.
- Hofmann, W.A., T. Johnson, M. Klapczynski, J.L. Fan, P. de Lanerolle (2006). "From transcription to transport: emerging roles for nuclear myosin I." Biochem Cell Biol **84**(4): 418-26.
- Holaska, J.M., A.K. Kowalski and K.L. Wilson (2004). "Emerin caps the pointed end of actin filaments: evidence for an actin cortical network at the nuclear inner membrane." PLoS Biol **2**(9): E231.
- Holmes, K.C., I. Angert, F.J. Kull, W. Jahn and R.R. Schröder (2003). "Electron cryo-microscopy shows how strong binding of myosin to actin releases nucleotide." Nature **425**(6956): 423-27.
- Holmes, K.C., D. Popp, W. Gebhard and W. Kabsch (1990). "Atomic model of the actin filament." Nature **347**(6288): 44-49.
- Holmes, K.C. and W. Kabsch (1991). "Muscle proteins: Actin." Curr. Opin. Struct. Biol. **1**: 270-280.
- Huttelmaier, S., S. Illenberger, I. Grosheva, M. Rüdiger, R.H. Singer and B.M. Jockusch (2001). "Raver1, a dual compartment protein, is a ligand for PTB/hnRNPI and microfilament attachment proteins." J Cell Biol **155**(5): 775-86.
- Irobi, E., L.D. Burtnick, D. Urosev, K. Narayan, R.C. Robinson (2003). "From the first to the second domain of gelsolin: a common path on the surface of actin?" FEBS Lett **552**(2-3): 86-90.
- Janmey, P.A. (1998). "The cytoskeleton and cell signaling: component localization and mechanical coupling." Physiol Rev **78**(3): 763-81.
- Jarnik, M. and U. Aebi (1991). "Toward a more complete 3-D structure of the nuclear pore complex." J Struct Biol **107**(3): 291-308.

- Jennings, G.T. and M.F. Bachmann (2008). "The coming of age of virus-like particle vaccines." Biol Chem **389**(5): 521-36.
- Jeyaseelan, R., C. Poizat, R.K. Baker, S. Abdishoo, L.B. Isterabadi, G.E. Lyons and L. Kedes (1997). "A novel cardiac-restricted target for doxorubicin. CARP, a nuclear modulator of gene expression in cardiac progenitor cells and cardiomyocytes." J Biol Chem **272**(36): 22800-08.
- Jockusch, B.M., S. Huttelmaier and S. Illenberger (2003). "From the nucleus toward the cell periphery: a guided tour for mRNAs." News Physiol Sci **18**: 7-11.
- Jockusch, B.M., K.H. Kelley, R.K. Meyer and M.M. Burger (1978). "An efficient method to produce specific anti-actin." Histochemistry **55**, 177-84.
- Jockusch, B.M., C.A. Schoenenberger, J. Stetfeld and U. Aebi (2006). "Tracking down the different forms of nuclear actin." Trends Cell Biol **16**(8): 391-96.
- Jockusch, H. and S. Voigt (2003). "Migration of adult myogenic precursor cells as revealed by GFP/nLacZ labelling of mouse transplantation chimeras." J Cell Sci **116**(Pt 8): 1611-16.
- Johnson, J.E. and W. Chiu (2000). "Structures of virus and virus-like particles." Curr Opin Struct Biol **10**(2): 229-35.
- Kabsch, W., H.G. Mannherz and D. Suck (1985). "Three-dimensional structure of the complex of actin and DNase I at 4.5 A resolution." Embo J **4**(8): 2113-18.
- Kabsch, W., H.G. Mannherz, D. Suck, E.F. Pai and K.C. Holmes (1990). "Atomic structure of the actin:DNase I complex." Nature **347**(6288): 37-44.
- Kaksonen, M., C.P. Toret and D.G. Drubin (2006). "Harnessing actin dynamics for clathrin-mediated endocytosis." Nat Rev Mol Cell Biol **7**(6): 404-14.
- Kajava, A.V. (1996). "Modeling of a five-stranded coiled coil structure for the assembly domain of the cartilage oligomeric matrix protein." Proteins **24**, 218-26.
- Kim, E., E. Bobkova, G. Hegyi, A. Muhrad and E. Reisler (2002). "Actin cross-linking and inhibition of the actomyosin motor." Biochemistry **41**(1): 86-93.
- Kiseleva, E., S.P. Drummond, M.W. Goldberg, S.A. Rutherford, T.D. Allen and K.L. Wilson (2004). "Actin- and protein-4.1-containing filaments link nuclear pore complexes to subnuclear organelles in *Xenopus* oocyte nuclei." J Cell Sci **117**(Pt 12): 2481-90.
- Kiser, P. F., G. Wilson and D. Needham (1998). "A synthetic mimic of the secretory granule for drug delivery." Nature **394**(6692): 459-62.

- Kistler, J., U. Aebi, L. Onorato, B. ten Heggeler and M.K. Showe (1978). "Structural changes during the transformation of bacteriophage T4 polyheads: characterization of the initial and final states by freeze-drying and shadowing Fab-fragment-labelled preparations." *J Mol Biol* **126**(3): 571-89.
- Kleinhenz, B., M. Fabienke, S. Swiniarski, N. Wittenmayer, J. Kirsch, B.M. Jockusch, H.H. Arnold and S. Illenberger (2005). "Raver2, a new member of the hnRNP family." *FEBS Lett* **579**(20): 4254-58.
- Klenchin, V.A., S.Y. Khaitlina and I. Rayment (2006). "Crystal structure of polymerization-competent actin." *J Mol Biol* **362**(1): 140-50.
- Knight, P. and G. Offer (1978). "p-NN'-phenylenebismaleimide, a specific cross-linking agent for F-actin." *Biochem J* **175**(3): 1023-32.
- Koteliansky, V.E. and G.N. Gneushev (1983). "Vinculin localization in cardiac muscle." *FEBS Lett* **159**(1-2): 158-60.
- Kramer, R.M., C. Li, D.C. Carter, M.O. Stone and R.R. Naik (2004). "Engineered protein cages for nanomaterial synthesis." *J Am Chem Soc* **126**(41): 13282-86.
- Krull, S., J. Thyberg, B. Björkroth, H.R. Rackwitz and V.C. Cordes (2004). "Nucleoporins as components of the nuclear pore complex core structure and Tpr as the architectural element of the nuclear basket." *Mol Biol Cell* **15**(9): 4261-77.
- Kudryashov, D.S., M. Phillips and E. Reisler (2004). "Formation and destabilization of actin filaments with tetramethylrhodamine-modified actin." *Biophys J* **87**(2): 1136-45.
- Kukalev, A., Y. Nord, C. Palmberg, T. Bergman and P. Percipalle (2005). "Actin and hnRNP U cooperate for productive transcription by RNA polymerase II." *Nat Struct Mol Biol* **12**(3): 238-44.
- Lagerkvist, A.C., Z. Foldes-Papp, M.A. Persson and R. Rigler (2001). "Fluorescence correlation spectroscopy as a method for assessment of interactions between phage displaying antibodies and soluble antigen." *Protein Sci* **10**, 1522-28.
- Lange, S., D. Auerbach, P. McLoughlin, E. Perriard, B.W. Schäfer, J.-C. Perriard and E. Ehler (2002). "Subcellular targeting of metabolic enzymes to titin in heart muscle may be mediated by DRAL/FHL-2." *J Cell Sci* **115**(Pt 24): 4925-36.
- Lange, S., E. Ehler, et al. (2006). "From A to Z and back? Multicompartment proteins in the sarcomere." *Trends Cell Biol* **16**(1): 11-18.

- Lange, S., F. Xiang, A. Yakovenko, A. Vihola, P. Hackman, E. Rostkova, J. Kristensen, B. Brandmeier, G. Franzen, B. Hedberg, L. G. Gunnarsson, S.M. Hughes, S. Marchand, T. Sejersen, I. Richard, L. Edström, E. Ehler, B. Udd and M. Gautel (2005). "The kinase domain of titin controls muscle gene expression and protein turnover." *Science* **308**(5728): 1599-603.
- Langer, R. (1998). "Drug delivery and targeting." *Nature* **392**(6679 Suppl): 5-10.
- Lassing, I., F. Schmitzberger, M. Björnstedt, A. Holmgren, P. Nordlund, C.E. Schutt and U. Lindberg (2007). "Molecular and structural basis for redox regulation of beta-actin." *J Mol Biol* **370**(2): 331-48.
- Lazarides, E. and K. Weber (1974). "Actin antibody: the specific visualization of actin filaments in non-muscle cells." *Proc Natl Acad Sci U S A* **71**, 2268-72.
- Leavitt, J., P. Gunning, L. Kedes and R. Jariwalla (1985). "Smooth muscle alpha-actin is a transformation-sensitive marker for mouse NIH 3T3 and Rat-2 cells." *Nature* **316**, 840-42.
- Leavitt, J. and T. Kakunaga (1980). "Expression of a variant form of actin and additional polypeptide changes following chemical-induced in vitro neoplastic transformation of human fibroblasts." *J Biol Chem* **255**(4): 1650-61.
- Leavitt, J., S.Y. Ng, U. Aebi, M. Varma, G. Latter, S. Burbeck, L. Kedes and P. Gunning (1987). "Expression of transfected mutant beta-actin genes: alterations of cell morphology and evidence for autoregulation in actin pools." *Mol Cell Biol* **7**(7): 2457-66.
- Lee, L. A. and Q. Wang (2006). "Adaptations of nanoscale viruses and other protein cages for medical applications." *Nanomedicine* **2**(3): 137-49.
- Lee, S., J. Choi and Z. Xu (2003). "Microbial cell-surface display." *Trends Biotechnol* **21**, 45-52.
- Lepault, J., B. Dargent, W. Tichelaar, J.P. Rosenbusch, K. Leonard and F. Pattus (1988). "Three-dimensional reconstruction of maltoporin from electron microscopy and image processing." *Embo J* **7**(1): 261-68.
- Liljas, L. (1999). "Virus assembly." *Curr Opin Struct Biol* **9**(1): 129-34.
- Littlefield, R., A. Almenar-Queralt and V.M. Fowler (2001). "Actin dynamics at pointed ends regulates thin filament length in striated muscle." *Nat Cell Biol* **3**(6): 544-51.
- Lomonosoff, G.P and J.E. Johnson (1996). "Use of macromolecular assemblies as expression systems for peptides and synthetic vaccines." *Curr Opin Struct Biol* **6**: 176-82.

- Lorenz, M., K.J. Poole, D. Popp, G. Rosenbaum and K.C. Holmes (1995). "An atomic model of the unregulated thin filament obtained by X-ray fiber diffraction on oriented actin-tropomyosin gels." *J Mol Biol* **246**(1): 108-19.
- Lorenz, M., D. Popp and K.C. Holmes (1993). "Refinement of the F-actin model against X-ray fiber diffraction data by the use of a directed mutation algorithm." *J Mol Biol* **234**(3): 826-36.
- Ludwig, C. and R. Wagner (2007). "Virus-like particles-universal molecular toolboxes." *Curr Opin Biotechnol* **18**, 537-45.
- Malashkevich, V.N., R.A. Kammerer, V.P. Efimov, T. Schulthess and J. Engel (1996). "The crystal structure of a five-stranded coiled coil in COMP: a prototype ion channel?" *Science* **274**(5288): 761-65.
- Mannherz, H.G., J. Gooch, M. Way, A.G. Weeds and P.J. McLaughlin (1992). "Crystallization of the complex of actin with gelsolin segment 1." *J Mol Biol* **226**(3): 899-901.
- Martin, A.F. (1981). "Turnover of cardiac troponin subunits. Kinetic evidence for a precursor pool of troponin-I." *J Biol Chem* **256**(2): 964-8.
- May, T., S. Gleiter and H. Lilie (2002). "Assessment of cell type specific gene transfer of polyoma virus like particles presenting a tumor specific antibody Fv fragment." *J Virol Methods* **105**(1): 147-57.
- Mayboroda, O., K. Schluter and B.M. Jockusch (1997). "Differential colocalization of profilin with microfilaments in PtK2 cells." *Cell Motil Cytoskeleton* **37**(2): 166-77.
- McDonald, D., G. Carrero, C. Andrin, G. de Vries and M.J. Hendzel (2006). "Nucleoplasmic beta-actin exists in a dynamic equilibrium between low-mobility polymeric species and rapidly diffusing populations." *J Cell Biol* **172**(4): 541-52.
- McKenna, N.M., C.S. Johnson and W. Yu-Li (1986). "Formation and alignment of Z lines in living chick myotubes microinjected with rhodamine-labeled alpha-actinin." *J Cell Biol* **103**(6 Pt 1): 2163-71.
- McLaughlin, P.J., J.T. Gooch, H.G. Mannherz and A.G. Weeds (1993). "Structure of gelsolin segment 1-actin complex and the mechanism of filament severing." *Nature* **364**(6439): 685-92.
- Medalia, O., I. weber, A.S. Frangakis, D. Nicastro, G. Gerisch and W. Baumeister (2002). "Macromolecular architecture in eucaryotic cells visualized by cryoelectron microscopy." *Science* **298**(5596): 1209-13.

- Michele, D.E., F.P. Albayya and J.M. Metzger (1999). "Thin filament protein dynamics in fully differentiated adult cardiac myocytes: toward a model of sarcomere maintenance." *J Cell Biol* **145**(7): 1483-95.
- Michelot, A., C. Guérin, S. Huang, M. Ingouff, S. Richard, N. Rodiuc, C.J. Staiger and L. Blanchoin (2005). "The formin homology 1 domain modulates the actin nucleation and bundling activity of Arabidopsis FORMIN1." *The Plant Cell* **17**: 2296-2313.
- Miki, M., J.A. Barden, C.G. dos Remedios, L. Phillips and B.D. Hambly (1987). "Interaction of phalloidin with chemically modified actin". *Eur J Biochem* **165**(1): 125-30.
- Miller, M.K., M.L. Bang, C.C. Witt, D. Labeit, C. Trombitas, K. Watanabe, H. Granzier, A.S. McElhinny, C.C. Gregorio and S. Labeit (2003). "The muscle ankyrin repeat proteins: CARP, ankrd2/Arpp and DARP as a family of titin filament-based stress response molecules." *J Mol Biol* **333**(5): 951-64.
- Milligan, R.A., M. Whittaker and D. Safer (1990). "Molecular structure of F-actin and location of surface binding sites." *Nature* **348**(6298): 217-21.
- Millonig, R., H. Salvo and U. Aebi (1988). "Probing actin polymerization by intermolecular cross-linking." *J Cell Biol* **106**(3): 785-96.
- Morris, E.J. and A.B. Fulton (1994). "Rearrangement of mRNAs for costamere proteins during costamere development in cultured skeletal muscle from chicken." *J Cell Sci* **107 (Pt 3)**: 377-86.
- Mulder, J., M. Poland, M.F.B.G. Gebbink, J. Calafat, W.H. Moolenaar and O. Kranenburg (2003). "p116Rip is a novel filamentous actin-binding protein." *J Biol Chem* **278**(29): 27216-23.
- Muller, S.A. and A. Engel (1998). "Mass Measurement in the Scanning Transmission Electron Microscope: A Powerful Tool for Studying Membrane Proteins." *J Struct Biol* **121**(2): 219-30.
- Muller, S.A. and A. Engel (2001). "Structure and mass analysis by scanning transmission electron microscopy." *Micron* **32**(1): 21-31.
- Muller, S.A., K.N. Goldie, R. Bürki, R. Häring and A. Engel (1992). "Factors influencing the precision of quantitative scanning transmission electron microscopy." *Ultramicroscopy* **46**: 317-34.
- Muller, S.A., M. Haner, I. Ortiz, U. Aebi and H.F. Epstein (2001). "STEM Analysis of Caenorhabditis elegans muscle thick filaments: evidence for microdifferentiated substructures." *J Mol Biol* **305**(5): 1035-44.

- Muller, S.A., M.O. Steinmetz, U. Aebi and A. Engel (1996). "Imaging and measuring biomolecules and their assemblies by scanning transmission electron microscopy." MIH University Basel Booklet: chapter 4.
- Mullins, R.D., J.A. Heuser and T.D. Pollard (1998). "The interaction of Arp2/3 complex with actin: nucleation, high affinity pointed end capping, and formation of branching networks of filaments." Proc Natl Acad Sci U S A **95**(11): 6181-86.
- Oda, T., K. Namba and Y. Maeda (2005). "Position and orientation of phalloidin in F-actin determined by X-ray fiber diffraction analysis." Biophys J **88**(4): 2727-36.
- Olave, I.A., S.L. Reck-Peterson and G.R. Crabtree (2002). "Nuclear actin and actin-related proteins in chromatin remodeling." Annu Rev Biochem **71**: 755-81.
- Ono, S. (2003). "Regulation of actin filament dynamics by actin depolymerizing factor/cofilin and actin-interacting protein 1: new blades for twisted filaments." Biochemistry **42**(46): 13363-70.
- Orlova, A., A. Shvetsov, V.E. Galkin, D.S. Kudryashov, P.A. Rubenstein, E.H. Egelman and E. Reisler (2004). "Actin-destabilizing factors disrupt filaments by means of a time reversal of polymerization." Proc Natl Acad Sci U S A **101**(51): 17664-68.
- Orlova, A. and E.H. Egelman (1995). "Structural dynamics of F-actin: I. Changes in the C-terminus." J Mol Biol **245**(5): 582-97.
- Otterbein, L. R., C. Cosio, et al. (2002). "Crystal structures of the vitamin D-binding protein and its complex with actin: structural basis of the actin-scavenger system." Proc Natl Acad Sci U S A **99**(12): 8003-08.
- Otterbein, L.R., P. Graceffa and R. Dominguez (2001). "The crystal structure of uncomplexed actin in the ADP state." Science **293**(5530): 708-11.
- Palmer, K.E., A. Benko, S.A. Doucette, T.I. Cameron, T. Foster, K. M. Hanley, A.A. McCormick, M. McCulloch, G.P. Pogue, M.L. Smith and N.D. Christensen (2006). "Protection of rabbits against cutaneous papillomavirus infection using recombinant tobacco mosaic virus containing L2 capsid epitopes." Vaccine **24**, 5516-25.
- Pantaloni, D., C. Le Clairche and M.F. Carlier (2001). "Mechanism of actin-based motility." Science **292**(5521): 1502-06.
- Pardo, J.V., J.D. Siliciano and S.W. Craig (1983). "A vinculin-containing cortical lattice in skeletal muscle: transverse lattice elements ("costameres") mark sites of attachment between myofibrils and sarcolemma." Proc Natl Acad Sci U S A **80**(4): 1008-12.
- Paulillo, S.M., E.M. Phillips, J. Köser, U. Sauder, K.S. Ullman, M.A. Powers and B. Fahrenkrog (2005). "Nucleoporin domain topology is linked to the transport status of the nuclear pore complex." J Mol Biol **351**(4): 784-98.

- Pederson, T. and U. Aebi (2002). "Actin in the nucleus: what form and what for?" J Struct Biol **140**(1-3): 3-9.
- Pederson, T. and U. Aebi (2005). "Nuclear actin extends, with no contraction in sight." Mol Biol Cell **16**(11): 5055-60.
- Pelham, R.J. Jr. and F. Chang (2001). "Role of actin polymerization and actin cables in actin-patch movement in *Schizosaccharomyces pombe*." Nat Cell Biol **3**(3): 235-44.
- Percipalle, P. and N. Visa (2006). "Molecular functions of nuclear actin in transcription." J Cell Biol **172**(7): 967-71.
- Pinson, A. (1990). "Cell Culture Techniques in Heart and Vessel." (Piper H. M., ed): 20-35.
- Pollard, T.D. (2003). "The cytoskeleton, cellular motility and the reductionist agenda." Nature **422**(6933): 741-45.
- Pollard, T.D. (2007). "Regulation of actin filament assembly by Arp3/3 complex and formins." Annu Rev Biophys Biomol Struct **36**: 451-77.
- Pollard, T.D., L. Blanchoin and R.D. Mullins (2000). "Molecular mechanisms controlling actin filament dynamics in nonmuscle cells." Annu Rev Biophys Biomol Struct **29**: 545-76.
- Pollard, T.D. and G.G. Borisy (2003). "Cellular motility driven by assembly and disassembly of actin filaments." Cell **112**(4): 453-65.
- Pope, B.J., S.M. Gonsior, S. Yeoh, A. McGough and A.G. Weeds (2000). "Uncoupling actin filament fragmentation by cofilin from increased subunit turnover." J Mol Biol **298**(4): 649-61.
- Porta, C., V.E. Spall, T. Lin, J.E. Johnson and G.P. Lomonosoff (1996). "The development of cowpea mosaic virus as a potential source of novel vaccines." Intervirology **39**: 79-84.
- Rafelski, S.M. and J.A. Theriot (2004). "Crawling toward a unified model of cell mobility: spatial and temporal regulation of actin dynamics." Annu Rev Biochem **73**: 209-39.
- Raman, S. (2007). "Design and analysis of peptide based nanoparticles." Dissertation.
- Raman, S., G. Machaidze, A. Lustig, U. Aebi and P. Burkhard (2006). "Structure-based design of peptides that self-assemble into regular polyhedral nanoparticles." Nanomedicine **2**(2): 95-102.
- Reddy, S.T., A.J. van der Vlies, E. Simeoni, V. Angeli, G.J. Randolph, C.P. O'Neil, L.K. Lee, M.A. Schwartz and J.A. Hubbell (2007). "Exploiting lymphatic transport and complement activation in nanoparticle vaccines." Nat Biotechnol **25**: 1159-64.

- Reichelt, R., A. Holzenburg, E.L. Buhle Jr, M. Jarnik, A. Engel and U. Aebi (1990).
“Correlation between structure and mass distribution of the nuclear pore complex and of distinct pore complex components.” J Cell Biol **110**(4): 883-94.
- Ren, Z.J., G.K. Lewis, P.T. Wingfield, E.G. Locke, A.C. Steven and L.W. Black (1996).
“Phage display of intact domains at high copy number: a system based on SOC, the small outer capsid protein of bacteriophage T4.” Protein Sci **5**, 1833-43.
- Reutzel, R., C. Yoshioka, L. Govindasamy, E.G. Yarmola, M. Agbandje-McKenna, M.R. Bubb and R. McKenna (2004). “Actin crystal dynamics: structural implications for F-actin nucleation, polymerization, and branching mediated by the anti-parallel dimer.” J Struct Biol **146**(3): 291-301.
- Rigler, R., Z. Foldes-Papp, F.J. Meyer-Almes, C. Sammet, M. Volcker and A. Schnez (1998). “Fluorescence cross-correlation: a new concept for polymerase chain reaction.” J Biotechnol **63**, 97-109.
- Rould, M.A., Q. Wan, P.B. Joel, S. Lowey and K.M. Trybus (2006). “Crystal structures of expressed non-polymerizable monomeric actin in the ADP and ATP states.” J Biol Chem **281**(42): 31909-19.
- Roy, P. and R. Noad (2008). “Virus-like particles as a vaccine delivery system: myths and facts.” Hum Vaccin **4**, 5-12.
- Ruan, Q. and S.Y. Tetin (2008). “Applications of dual-color fluorescence cross-correlation spectroscopy in antibody binding studies.” Anal Biochem **374**, 182-95.
- Russell, B., D. Motlagh and W.A. Ashley (2000). “Form follows function: how muscle shape is regulated by work.” J Appl Physiol **88**(3): 1127-32.
- Ruwhof, C. and A. van der Laarse (2000). “Mechanical stress-induced cardiac hypertrophy: mechanisms and signal transduction pathways.” Cardiovasc Res **47**(1): 23-37.
- Ruzanov, P.V., V.M. Evdokimova, N.L. Korneeva, J.W. Hershey and L.P. Ovchinnikov (1999). “Interaction of the universal mRNA-binding protein, p50, with actin: a possible link between mRNA and microfilaments.” J Cell Sci **112** (Pt 20): 3487-96.
- Sablin, E.P., J.F. Dawson, S.M.S. VanLoock, J.A. Spudich, E.H. Egelman and R.J. Fletterick (2002). “How does ATP hydrolysis control actin’s associations?” Proc Natl Acad Sci U S A **99**(17): 10945-47.
- Sanchez, J. and J. Holmgren (1989). “Recombinant system for overexpression of cholera toxin B subunit in *Vibrio cholerae* as a basis for vaccine development.” Proc Natl Acad Sci U S A **86**, 481-85.

- Sanchez-Carbayo, M., K. Schwarz, E. Charytonowicz, C. Cordon-Cardo and P. Mundel (2003). "Tumor suppressor role for myopodin in bladder cancer: loss of nuclear expression of myopodin is cell-cycle dependent and predicts clinical outcome." *Oncogene* **22**(34): 5298-305.
- Savic, R., L. Luo, A. Eisenberg and D. Maysinger (2003). "Micellar nanocontainers distribute to defined cytoplasmic organelles." *Science* **300**(5619): 615-18.
- Small, J.V. and J.E. Celis (1978). "Direct visualization of the 10-nm (100-A)-filament network in whole and enucleated cultured cells." *J Cell Sci* **31**, 393-409.
- Schmid, M.F., M.B. Sherman, P. Matsudaira and M. Chiu (2004). "Structure of the acrosomal bundle." *Nature* **431**(7004): 104-07.
- Schoenenberger, C.A., N. Bischler, B. Fahrenkrog and U. Aebi (2002). "Actin's propensity for dynamic filament patterning." *FEBS Lett* **529**(1): 27-33.
- Schoenenberger, C.A., S. Buchmeier, M. Boerries, R. Sütterlin, U. Aebi and B.M. Jockusch (2005). "Conformation-specific antibodies reveal distinct actin structures in the nucleus and the cytoplasm." *J Struct Biol* **152**(3): 157-68.
- Schoenenberger, C.A., M.O. Steinmetz, D. Stoffler, A. Mandinova and U. Aebi (1999). "Structure, assembly, and dynamics of actin filaments in situ and in vitro." *Microsc Res Tech* **47**(1): 38-50.
- Schutt, C.E., J.C. Myslik, M.D. Rozycki, N.C. Goonesekere and U. Lindberg (1993). "The structure of crystalline profilin-beta-actin." *Nature* **365**(6449): 810-16.
- Schwille, P., F.J. Meyer-Almes and R. Rigler (1997). "Dual-color fluorescence cross-correlation spectroscopy for multicomponent diffusional analysis in solution." *Biophys J* **72**, 1878-86.
- Shvetsov, A., R. Musib, M. Phillips, P.A. Rubenstein and E. Reisler (2002). "Locking the hydrophobic loop 262-274 to G-actin surface by a disulphide bridge prevents filament formation." *Biochemistry* **41**(35): 10787-93.
- Silvestrini, R.A. and E.M. Benson (2001). "Whither smooth muscle antibodies in the third millennium?" *J Clin Pathol* **54**, 677-78.
- Skalli, O., P. Ropraz, A. Trzeciak, G. Benzonana, D. Gillessen and G. Gabbiani (1986). "A monoclonal antibody against alpha-smooth muscle actin: a new probe for smooth muscle differentiation." *J Cell Biol* **103**, 2787-96.
- Slot, J.W. and H.J. Geuze (1985). "A new method of preparing gold probes for multiple-labeling cytochemistry." *Eur J Cell Biol* **38**(1): 87-93.

- Small, J.V. and J.E. Celis (1978). "Direct visualization of the 10-nm (100-A)-filament network in whole and enucleated cultured cells." *J Cell Sci* **31**, 393-409.
- Smith, P.R., W.E. Fowler, T.D. Pollard and U. Aebi (1983). "Structure of the actin molecule determined from electron micrographs of crystalline actin sheets with a tentative alignment of the molecule in the actin filament." *J Mol Biol* **167**(3): 641-60.
- Smith, M.L., J.A. Lindbo, S. Dillard-Telm, P.M. Brosio, A.B. Lasnik, A.A. McCormick, L.V. Nguyen and K.E. Palmer (2006). "Modified tobacco mosaic virus particles as scaffolds for display of protein antigens for vaccine applications." *Virology* **348**, 475-88.
- Spellman, R., A. Rideau, A. Matlin, C. Gooding, F. Robinson, N. McGlincy, S.N. Grellscheid, J. Southby, M. Wollerton and C.W. Smith (2005). "Regulation of alternative splicing by PTB and associated factors." *Biochem Soc Trans* **33**(Pt 3): 457-60.
- Spudich, J.A. and S. Watt (1971). "The regulation of rabbit skeletal muscle contraction. I. Biochemical studies of the interaction of the tropomyosin-troponin complex with actin and the proteolytic fragments of myosin." *J Biol Chem* **246**(15): 4866-71.
- Steinmetz, M.O., K.N. Goldie and U. Aebi (1997). "A correlative analysis of actin filament assembly, structure, and dynamics." *J Cell Biol* **138**(3): 559-74.
- Steinmetz, M.O., A. Hoenger, P. Tittmann, K.H. Fuchs, H. Gross and Aebi (1998). "An atomic model of crystalline actin tubes: combining electron microscopy with X-ray crystallography." *J Mol Biol* **278**(4): 703-11.
- Steinmetz, M.O., D. Stoffler, A. Hoenger, A. Bremer and U. Aebi (1997). "Actin: from cell biology to atomic detail." *J Struct Biol* **119**(3): 295-320.
- Stuven, T., E. Hartmann and D. Göhrlich (2003). "Exportin 6: a novel nuclear export receptor that is specific for profilin.actin complexes." *Embo J* **22**(21): 5928-40.
- Taschner, N., S.A. Muller, V.R. Alumella, K.N. Goldie, A.F. drake, U. Aebi and T. Arvinte (2001). "Modulation of antigenicity related to changes in antibody flexibility upon lyophilization". *J Mol Biol* **310**(1): 169-79.
- Taylor, K.A. and D.W. Taylor (1992). "Formation of 2-D paracrystals of F-actin on phospholipid layers mixed with quaternary ammonium surfactants." *J Struct Biol* **108**(2): 140-47.
- Tokuyasu, K.T., A.H. Dutton, B. Geiger and S.J. Singer (1981). "Ultrastructure of chicken cardiac muscle as studied by double immunolabeling in electron microscopy." *Proc Natl Acad Sci U S A* **78**(12): 7619-23.

- Valcarcel, J. and F. Gebauer (1997). "Post-transcriptional regulation: the dawn of PTB." Curr Biol **7**(11): R705-08.
- Vandekerckhove, J., A. Deboen, M. Nassal and T. Wieland (1985). "The phalloidin binding site of actin." Embo J **4**(11): 2815-18.
- Vandekerckhove, J., J. Leavitt, T. Kakunaga and K. Weber (1980). "Coexpression of a mutant beta-actin and the two normal beta- and gamma-cytoplasmic actins in a stably transformed human cell line." Cell **22**(3): 893-99.
- Vandekerckhove, J. and K. Weber (1979). "Amino-acid sequence analysis of the amino-terminal tryptic peptides of different actins from the same mammal [proceedings]". Arch Int Physiol Biochim **87**, 210-12.
- Vorobiev, S., B. Strokopytov, D.G. Drublin, C. Frieden, S. Ono, J. Condeelis, P.A. Rubenstein and S.C. Almo (2003). "The structure of nonvertebrate actin: implications for the ATP hydrolytic mechanism." Proc Natl Acad Sci U S A **100**(10): 5760-65.
- Wagner, E.J. and M.A. Garcia-Blanco (2001). "Polypyrimidine tract binding protein antagonizes exon definition." Mol Cell Biol **21**(10): 3281-88.
- Wang, J., N. Shaner, B. Mittal, Q. Zhou, J. Chen, J.M. Sanger and J.W. Sanger (2005). "Dynamics of Z-band based proteins in developing skeletal muscle cells." Cell Motil Cytoskeleton **61**(1): 34-48.
- Weins, A., K. Schwarz, C. Faul, L. Barisoni, W.A. Linke and P. Mundel (2001). "Differentiation- and stress-dependent nuclear cytoplasmic redistribution of myopodin, a novel actin-bundling protein." J Cell Biol **155**(3): 393-404.
- Wieland, T. and H. Faulstich (1977). "The action of phalloidin." Curr Probl Clin Biochem **7**: 11-4.
- Wieland, T. and H. Faulstich (1978). "Amatoxins, phallotoxins, phallolysin, and antamanide: the biologically active components of poisonous Amanita mushrooms." CRC Crit Rev Biochem **5**(3): 185-260.
- Wilmsen, H.U., K.R. Leonard, W. Tichelaar, J.T. Buckley and F. Pattus (1992). "The aerolysin membrane channel is formed by heptamerization of the monomer." Embo J **11**(7): 2457-63.
- Witt, S., A. Zieseniss, U. Fock, B.M. Jockusch and S. Illenberger (2004). "Comparative biochemical analysis suggests that vinculin and metavinculin cooperate in muscular adhesion sites." J Biol Chem **279**(30): 31533-43.

- Young, P., E. Ehler and M. Gautel (2001). "Obscurin, a giant sarcomeric Rho guanine nucleotide exchange factor protein involved in sarcomere assembly." J Cell Biol **154**(1): 123-36.
- Zak, R., A.F. Martin, G. Prior and m. Rabinowitz (1977). "Comparison of turnover of several myofibrillar proteins and critical evaluation of double isotope method." J Biol Chem **252**(10): 3430-35.
- Zieseniss (2005). "Biochemische Charakterisierung des „dual compartment“- Proteins Raver1: Neue Aspekte der Ligandenbindung und Regulation." Dissertation.
- Zieseniss, A., U. Schroeder, S. Buchmeier, C.-A. Schoenenberger, J. Heuvel, B.M. Jockusch and S. Illenberger (2007). "Raver1 is an integral component of muscle contractile elements." Cell Tissue Res **327**(3): 583-94.
- Zinkernagel, R.M. (1996). "Immunology taught by viruses." Science **271**(5246): 173-78.
- Zinkernagel, R.M. (2003). "On natural and artificial vaccinations." Annu Rev Immunol **21**, 515-46.

Acknowledgments

First of all, I would like to thank Prof. Ueli Aebi for giving me the opportunity to do my PhD in his laboratory.

Next, I am very grateful to PD Dr. Cora-Ann Schoenenberger for her continuous support, guidance and patience during the last years. Dear Cora, without your knowledge and assistance this study would not have been successful. Thank you so much!

I would also like to thank the other members of my thesis committee, Prof. Hans-Georg Mannherz and Prof. Tilmann Schirmer.

My special thanks go to the nice (former) colleagues of MIH for their scientific and private support. In particular, thanks to Alexandra, Yvonne, Marija, Esther, Birthe, Sara, Larissa, Sofia, Prof. Peter Burkhard, Gia, David T., David W., Rod, Bohus, Senthil, Kyrill, Laurent, Christian, Jochen, Unai and Marko. Many thanks to Vesna and Ursula, who helped in CTEM preparation and preparing the student courses. I will keep all of you in mind as very helpful and understanding friends.

Many thanks also to the ‘STEM team’, Dr. Shirley Müller, Françoise, and Phillippe, to Per from biophysics and to the ‘Braunschweig group’, Prof. Brigitte Jockusch, Sabine Buchmeier, Susanne Illenberger and Anke Zieseniss.

Thanks to Urs Berglas (animal facility), Margit Jenny and Roland Buerki (computer administrators), Röbi Wyss (maintenance of machinery), Liselotte Walti (secretary) and to Barbara Merz for cleaning our equipment, amusing conversation and for numerous cakes.

I want to express my gratitude to my nice office- and labmate Teba, who has a great sense of humor and managed to make me laugh even during hard times. Dear Teba, I will never forget our funny time as lab rat siblings. You do not know, how much you helped me to get things done.

Huge thanks to my longtime friends Uwe and Michi for cheering me up, being patient and understanding.

Many thanks also to my beloved family, my mother and father as well as my sister Katrin with Olaf and lovely Magdalena and Johannes for your understanding and unconditional support and encouragement. I could always rely on you in good and bad times.

Dear Heike, I sincerely thank you so much for being the very best mother of our kids. Probably you did the greatest job of all.

Last but not least, thanks to our beloved sons Julian and Jacob. Your catching zest for life makes me forgetting all the daily trouble. I love you with all my heart!

Curriculum vitae



Name: Ulrich Johannes Hubertus Schroeder
Date of birth: 27. December 1969
Place of birth: Würzbburg
Nationality: German
Family status: single

Address (institute)

M.E. Müller Institute for Structural Biology, Biozentrum, University of Basel
Klingelbergstrasse 70, CH-4056 Basel, Switzerland
Telephon: +41 61 267 2095; Fax: +41 61 267 2109
Email: ulrich.schroeder@unibas.ch

Address (private)

Zeppelinstrasse 29, D-79540 Lörrach, Germany
Telephon: +49 7621 169716

Education

2003 - 2008 PhD student in cell biology
with Prof. U. Aebi and PD Dr. C-A. Schoenenberger; M.E. Müller Institute
for Structural Biology, Biozentrum, University of Basel, Switzerland

PhD thesis

„The ‘lower dimer’ and its role in actin patterning: Studying different forms
of actin by electron microscopy, biochemistry and tailor-made antibodies“
with Prof. Dr. Ueli Aebi, PD Dr. Cora-Ann Schoenenberger and
Prof. Dr. Hans Georg Mannherz

- 2002 Diploma in biology
„Biomass-spectra of litoral sediments of two lakes in particular consideration of unicellular organism“
with Prof. K. Hausmann and Dr. D. Dietrich; Institute for Zoology, Freie Universität Berlin, Germany
- 1996 - 2002 Studies in biology; Freie Universität Berlin, Germany
- 1995 Diploma in carpentering; Kernholz GmbH, Berlin, Germany
- 1992 - 1995 Vocational education in carpentering; Kernholz GmbH, Berlin, Germany
- 1990 - 1991 Civilian service; mobile social emergency service; Arbeiterwohlfahrt Karlsruhe, Germany
- 1988 - 1992 General qualification for university entrance; Gewerbliche Schulen Lörrach, Germany

Working experience

- 2008 Planing and design of laboratories and institutes; dr. heinekamp Labor- und Institutsplanung GmbH in Karlsfeld, Germany and Basel, Switzerland

Research experience

- 2004 EMBO practical course on cryo-electron microscopy and 3-D image analysis; The European Molecular Biology Laboratory (EMBL), Heidelberg, Germany
- 2003 - 2004 Five-month doctoral research training with Dr. A. Hoenger; The European Molecular Biology Laboratory (EMBL), Heidelberg, Germany

Teaching experience

- 2003 - 2007 Tutor in bloc courses for „biophysics and structural biology (incl. microscopy)“ for biology students; Biozentrum, University of Basel, Switzerland
- 1999 - 2002 Tutor in basic courses for zoology, evolution and systematic of animals and ecology for biology students; Freie Universität Berlin, Germany

Publications

Schroeder U., A. Graff, S. Buchmeier, P. Rigler, U. Silvan, D. Tropel, B.M. Jockusch, U. Aebi, P. Burkhard and C.-A. Schoenenberger (2008). „Peptide nanoparticles serve as a powerful platform for the immunogenic display of poorly antigenic actin determinants“. Manuscript accepted, J Mol Biol.

Zieseniss, A., U. Schroeder, A. Zieseniss, S. Buchmeier, C.-A. Schoenenberger, J. van den Heuvel, B.M. Jockusch, S. Illenberger (2007). „Raver1 is an integral component of muscle contractile elements.“ Cell Tissue Res 327(3): 583-94.

Poster

2006 „Peptide nanoparticle as a novel repetitive antigen display platform for antibody production.“ Schroeder U., A. Graff, S. Buchmeier, P. Rigler, D. Tropel, B.M. Jockusch, U. Aebi, P. Burkhard and C.-A. Schoenenberger; 9th Carl Zeiss sponsored workshop on FCS and related methods, Stockholm, Sweden

„Tailoring monoclonal antibodies to different forms of actin.“ Schroeder U., S. Buchmeier, D. Tropel, A. Graff, P. Burkhard, U. Aebi, B.M. Jockusch and C.-A. Schoenenberger; 29th annual conference of the Deutsche Gesellschaft für Zellbiologie (DGZ), Braunschweig, Germany

2005 „Potential binding partners for actin in the nucleus.“ Al-Haboubi T., U. Schroeder, V. Cordes, B.M. Jockusch, U. Aebi, B. Fahrenkrog and C.-A. Schoenenberger; Biozentrum symposium 2005, Basel, Switzerland

„The distribution of the hnRNP protein raver1 in different cells and tissues.“
Schroeder U., A. Zieseniss, S. Illenberger, B.M. Jockusch, V. Olivieri, U. Sauder, U. Aebi, B. Fahrenkrog and C.-A. Schoenenberger; Biozentrum symposium 2005, Basel, Switzerland

2004 „The actin ‚lower dimer‘ - an unconventional actin conformation.“ Schroeder U., U. Aebi and C.-A. Schoenenberger; EMBO Practical Course on Cryo-Electron Microscopy and 3-D Image Analysis; The European Molecular Biology Laboratory (EMBL), Heidelberg, Germany

Talk

2004 „Structural aspects of the actin ‚lower dimer‘ - a specific actin conformation.“
EMBO Practical Course on Cryo-Electron Microscopy and 3-D Image Analysis;
The European Molecular Biology Laboratory (EMBL), Heidelberg, Germany